NASA Contractor Report 189671

P-87

CONTINUATION OF TAILORED COMPOSITE STRUCTURES OF ORDERED STAPLE THERMOPLASTIC MATERIAL

MICHAEL H. SANTARE and R. BYRON PIPES

Department of Mechanical Engineering and the Center for Composite Materials at the University of Delaware, Newark, Delaware

Contract NAS1-18758
September 1992

National Aeronautics and Space Administration

Langley Research Center
Hampton, Virginia 23665-5225

Table of Contents

Abstract

The search for cost effective composite structure has motivated the investigation of several new approaches to develop composite structure from innovative material forms. Among the promising new approaches is the conversion of planar sheet to components of complex curvature through sheet forming or stretch forming. In both cases the potential for material stretch in the fiber direction appears to offer a clear advantage in formability over continuous fiber systems. In the present study the investigators have established a framework which allows the simulation of the anisotropic mechanisms of deformation of long discontinuous fiber laminates wherein the matrix phase is a viscous fluid.

Predictions for the effective viscosities of a hyper-anisotropic medium consisting of collimated, discontinuous fibers suspended in a viscous matrix developed earlier by the authors have been extended to capture the characteristics of typical polymers including non-Newtonian behavior and temperature dependence. In addition, the influence of fiber misorientation has also been modeled by compliance averaging to determine ensemble properties for a given orientation distribution.

A design tool is presented for predicting the effect of material heterogeneity on the performance of curved composite beams such as those used in aircraft fuselage structures. Material heterogeneity can be induced during manufacturing processes such as sheet forming and stretch forming of thermoplastic composites. This heterogeneity can be introduced in the form of fiber realignment and spreading during the manufacturing process causing radial and tangential gradients in material properties. Two analysis procedures are used to solve the beam problems. The first method uses separate two-dimensional elasticity solutions for the stresses in the flange and web sections of the beam. The separate solutions are coupled by requiring that forces and displacements match at section boundaries. The second method uses an approximate Rayleigh-Ritz technique to find the solutions for more complex beams. Analyses are performed for curved beams of various cross-sections loaded in pure bending and with a uniform distributed load. Preliminary results show that the geometry of the beam dictates the effect of heterogeneity on performance. The role of heterogeneity is larger in beams with a small average radius-to-depth ratio, R/t, where R is the average radius of the beam and t is the difference between the inside and outside radii. Results of the analysis are in the form of stresses and displacements and are compared to both mechanics of materials and numerical solutions obtained using finite element analysis.

List of Symbols (roman letters)

a	inside radius
A	area region
A_T	temperature shift factor
[A]	material stiffness matrix
b	outside radius
c	ratio of a to b
D	fiber diameter
E_{ij}	elastic stiffness moduli
f	fiber volume fraction
f_i	assumed displacement function
F	maximum packing volume fraction
g	geometric term
g_i	assumed displacement function
h	beam thickness
[H]	coefficient matrix
[K]	global stiffness matrix
L	fiber length, applied end load
M	applied moment
m	cos θ
n	radial heterogeneity coefficient, Carreau parameter
n	sin θ
{N}	stress resultant vector
P	internal pressure
q_i	undetermined displacement parameter
Q_i	undetermined displacement parameter
Q	external pressure
r	radial coordinate
R	average radius (of curved beam)
s	modified heterogeneity exponent
S	surface region
t	modified heterogeneity exponent, beam depth
T	temperature
T_o	baseline temperature
[T]	load vector
{t}	applied surface traction vector
u_i	displacement components
U	elastic strian energy
$[U_i]$	coefficient matrix
{u}	displacement vector
V	potential energy of external forces
v_i	undetermined displacement parameter
Z	assumed displacement function

List of Symbols (greek letters)

α_{ij}	elastic complience components
β_{ij}	viscous complience components
γ_n	material constant ratio
$\dot{\gamma}$	shear strain rate
ε	strain component
$\{\varepsilon\}$	strain vector
$\dot{\varepsilon}_N$	Newtonian strain rate
η	matrix fliud viscosity
η_{ij}	effective viscosity components
η_o	Carreau parameter
$\overline{\eta}_0$	modified Carreau parameter
θ	angle of misalignment
λ	Carreau parameter
$\overline{\lambda}$	modified Carreau parameter
μ	volume fraction factor
ν_{ij}	elastic constant
ξ	Carreau parameter
Π	potential energy
ρ	normalized radial coordinate
σ	stress component
ϕ	distribution function, stress potntial

Introduction

The extraordinary properties of collimated fiber composites consisting of continuous fibers suspended in a polymeric matrix have been well known for the past twenty plus years. These materials were made possible by the invention of synthetic fibers which possess specific strengths significantly greater than conventional monolithic materials. The high cost of advanced materials and manufacturing processes has limited much of their use to military applications where the demand for increased performance outweighs the increased cost. Breakthroughs in manufacturing techniques, materials and structural concepts are needed if advanced composites are to be used for primary structure in commercial aircraft.

The recent introduction of thermoplastic polymer matrices now offers the potential to develop manufacturing methods for these new composite materials that can take advantage of lower cost conventional manufacturing methods. Sheet forming of metallic materials is one of the most pervasive manufacturing methods in the contemporary technology. However, unlike monolithic metallic sheet, continuous fiber composites possess direction of inextensibility in the fiber direction. For these material systems the dominant modes of deformation during sheet forming are shearing. Extensibility in the fiber direction can, however be provided by introducing breaks along the fiber length so that the individual fibers are made discontinuous. The development of extensibility in the fiber direction for the collimated fiber composite results in enhanced formability of multiaxial sheet products.

The objective of the present work is to develop the science base for a series of models that can be used to link manufacturing with structural performance. Specific goals of the project are: 1) create models to predict the deformation mechanics and formability of long discontinuous fiber thermoplastic composites, 2) investigate several forming methods and produce prototype curved beam structures, 3) investigate analysis methods to predict the effects of process induced heterogeneity on structural performance.

Chapter one describes the recent work toward the development of models for predicting formability of discontinuous fiber thermoplastic composites. This represents the continuation of the micromechanics models presented in the previous report dated 12/90. The recent work includes a more general non-Newtonian matrix fluid behavior at the melt and allows for the inclusion of temperature dependence. Additionally, the influence of fiber misorientation is modeled to predict the effective viscosities for an ensemble for a given fiber orientation distribution.

Chapter two presents the analyses used to predict the effects of process induced heterogeneity on the performance of structural components. Two different approaches are used to predict stresses and deformations in heterogeneous curved beams. One uses closed form elasticity solutions and couples them for different regions in the structure. This procedure gives approximate solutions for beams of various cross sections with radially heterogeneous material properties. The second method is a Rayleigh-Ritz approach which allows for a more general description of material heterogeneity. Chapter three describes structural testing performed on prototype beams manufactured through a sub-contract with the Du Pont company.

The second objective listed above was the investigation of several forming methods for curved beams made from discontinuous fiber thermoplastic composite. In the previous report, the diaphragm forming process used at the University of Delaware was discussed. More recently, Du Pont was sub-contracted to produce prototype parts using their patented stretch-forming process. The final report for that sub-contract is included, unedited, in the appendix.

1.0 Constitutive Relations for Aligned Discontinuous Fiber Composites

1.1 Introduction

In several earlier papers [1-3] the authors developed models which predict the primary viscosities of an anisotropic incompressible material consisting of collimated, long discontinuous fibers suspended in a fluid matrix. A state of transverse isotropic symmetry was assumed for the medium. These models were developed by assuming the kinematics of adjacent rigid fibers and determining the resulting behavior of the matrix fluid. This procedure allows for the prediction of the effective properties of the medium including longitudinal elongational, in-plane shearing, transverse elongational and transverse shearing viscosities. Explicit expressions have been developed for each of the effective viscosities for a Newtonian matrix fluid. Table 1.1 shows a summary of these results in terms of fiber volume fraction, f, fiber aspect ratio, L/D (length/diameter), and matrix viscosity, η.

A deficiency of the simple power-law constitutive relation for a shear thinning fluid is its lack of a finite zero-shear viscosity. Most polymers exhibit a finite zero-shear viscosity. In a recent paper [4], the author's introduced a constitutive relation which exhibits a finite zero-shear rate viscosity and includes a temperature dependence into the relations for the effective material properties. This development will be summarized in the following.

1.2 Development

The effective viscosities shown in Table 1.1 fail to capture all the characteristics exhibited by polymer melts such as dependence on shear rate and temperature. Carreau [5,6] has introduced the following empirical rheological model to describe the non-Newtonian behavior of such a fluid.

$$\eta = \bar{\eta}_0 \left[1 + (\bar{\lambda}\dot{\gamma})^2\right]^{(n-1)/2} \tag{1.1}$$

Where $\dot{\gamma}$ is the rate of shear strain and the other terms are defined in the following. The onset of the nonlinearity is determined by the time constant, $\bar{\lambda}$. It is clear from equation (1.1) that for $(\bar{\lambda}\dot{\gamma})<<1$ the viscosity becomes Newtonian. The power law exponent, n, determines the degree of nonlinearity. The value of n=1 corresponds to a Newtonian fluid, and as the exponent decreases the fluid exhibits increased shear thinning.

It has been stated [7], that the influence of temperature on viscosity can be represented as follows:

$$\bar{\eta}_0 = \eta_0 A_T \; ; \; \bar{\lambda} = \lambda A_T \tag{1.2}$$

where the temperature shift factor, A_T, is defined as:

$$A_T = e^{-\xi(T/T_0-1)} \tag{1.2a}$$

Note, the temperature shift factor as defined above is normalized so that at a given reference temperature, T_0, the shift factor equals unity.

Viscosity versus shear rate data for typical high performance polymer PEEK at 399°C is shown in Figure 1.1. Figure 1.2 shows the temperature shift factor versus temperature for PEEK. Equation (1.1) and equation (1.2a) were fit to the PEEK data thus determining the parameters as follows:

$$\eta_0 = 280 \text{ Pa-S}, \lambda = 0.038 \text{ S}, n = 0.787, \xi = 6.56$$

Equations (1.1) and (1.2a) are compared with the experimental data in Figures 1.1 and 1.2.

Employing this matrix constitutive relation and the development presented in reference [3] it is possible to derive new expressions for effective viscosities of the medium as follows:

$$\eta_{11} = \frac{\eta_0 A_T (1-\mu) f}{2\mu} (L/D)^2 \left[1 + \frac{A_T^2 (1-\mu)^2 (L/D)^2}{4\mu^2} (\lambda \dot{\varepsilon}_{11})^2 \right]^{(n-1)/2} \tag{1.3a}$$

$$\eta_{22} = \frac{4\eta_0 A_T}{\mu} \left[1 + \frac{4A_T^2}{\mu^2} (\lambda \dot{\varepsilon}_{22})^2 \right]^{(n-1)/2} \tag{1.3b}$$

$$\eta_{12} = \frac{\eta_0 A_T (1+\mu)}{2\mu} \left[1 + \frac{A_T^2 (1+\mu)^2}{4\mu^2} (\lambda \dot{\gamma}_{12})^2 \right]^{(n-1)/2} \tag{1.3c}$$

$$\eta_{23} = \frac{\eta_0 A_T}{\mu} \left[1 + \frac{A_T^2}{\mu^2} (\lambda \dot{\gamma}_{23})^2 \right]^{(n-1)/2} \tag{1.3d}$$

where

$$\mu = 1 - \sqrt{f/F} \; ; \; F = \begin{cases} \frac{\pi}{4} & \text{square array} \\ \frac{\pi}{2\sqrt{3}} & \text{hexagonal array} \end{cases}$$

1.3 Results

Given the material descriptors and matrix properties as a function of temperature and strain rate, equations (1.3a-d) can be utilized to predict the unique properties of the material. Figure 1.3 shows these predictions for the PEEK data discussed in the next section in conjunction with a square array of 60 percent fiber volume content and a fiber aspect ratio of 10^4. The figure illustrates the relative difference in the various effective viscosities. It is especially interesting that the maximum Newtonian strain rate is lower for the fiber filled polymer than for the neat polymer.

This is especially evident in the longitudinal elongational viscosity which begins to exhibit the shear thinning phenomenon at an elongational strain rate approximately three orders of magnitudes less than the fluid's maximum Newtonian strain rate.

Figure 1.4 shows the effect of temperature on the in-plane viscosity versus strain rate. Notice that an increase in temperature decreases the viscosity but increases the maximum range in rate over which Newtonian behavior is observed.

Since the Carreau parameters are determined empirically, it is instructive to study the effects of varying the various parameters on the effective viscosity of the composite system. Therefore,to gain a better understanding of the strain rate and temperature dependence, a parametric study of the Carreau model parameters will be presented. Only the longitudinal elongational viscosity will be illustrated since the same general tendencies will hold for all the viscosities in equation (1.3). For large strain rate, it is clear that the quantity (n-1) defines the slope of the viscosity versus strain rate curve on a log-log scale. This is illustrated in Figure 1.5 for values of the power law term in the range 0-1. Note that n=1 corresponds to the Newtonian case. Using a log-log bi-linear approximation for the viscosity strain rate relation, an upper bound for the maximum Newtonian strain rate is

$$\dot{\varepsilon}_N = \frac{2\mu}{A_T(1-\mu)(L/D)\lambda} \tag{1.4}$$

Equation (1.4) shows that as the time constant increases, $\dot{\varepsilon}_N$ decreases. This effect of the time constant on $\dot{\varepsilon}_N$ is illustrated in Figure 1.6. The influence of the fiber geometry on viscosity can also be observed by studying equation (1.4). Increases in L/D will result in a decrease in the maximum Newtonian strain rate for the fiber assembly. The temperature dependency on the viscosity appears in the zero-shear rate viscosity and the time constant. As the temperature shift factor increases, the zero-shear rate viscosity and the time constant decrease. This is illustrated in Figure 1.7 for various values of the temperature shift factor.

1.3.1 Influence of Fiber Orientation on The Viscoities of Anisotropic Materials

The relationships for the material properties as presented above are valid for a system of perfectly aligned fibers which coincides with the reference axes. Many times the fibers are off axis to the loads and hence the reference axis. In this case the effective properties are of interest. Also due to manufacturing and processing, the fibers are not perfectly aligned. The effective viscosities for these two conditions will be studied in the following.

The effective viscosities for a medium consisting of collimated, long discontinuous fibers suspended in a viscous matrix were examined in the last section. These results have shown that the effective viscosities for such a system are highly anisotropic with anisotropy ratios which often exceed 10^6 for fiber aspect ratios of 10^3 - 10^4. Given the extreme sensitivity to material anisotropy of material properties transformed outside the principal material coordinate system, it is clear that fiber orientation will have a great influence upon effective material properties. Two conditions of fiber orientation must be considered. First, the condition where fibers are perfectly collimated but do not coincide with the load direction and second, the condition where individual fibers are misoriented with respect to the principal material direction. In the latter case, misorientation of individual fibers might have occurred during the manufacturing step, while in the former case the inability to insure that the test directions and material principal directions coincide could lead to measurement of properties which could differ greatly from actual values.

1.3.2 Transformed Properties

For orthotropic viscous materials in plane stress with the principal material designated "1", the principal viscosities are:

η_{11} : longitudinal elongational viscosity
η_{22} : transverse elongational viscosity
η_{12} : inplane shearing viscosity

The apparent or transformed properties at any angle, θ may be expressed in terms of the principal viscosities and the angle, θ through the standard transformation.

$$\eta_{11}'(\theta)/\eta_{11} = \left[m^4 + (\eta_{11}/\eta_{12}-1)m^2n^2 + (\eta_{11}/\eta_{22})n^4\right]^{-1} \tag{1.5}$$

$$\eta_{22}'(\theta)/\eta_{22} = \left[m^4 + (\eta_{22}/\eta_{12}-\eta_{22}/\eta_{11})m^2n^2 + (\eta_{22}/\eta_{11})n^4\right]^{-1} \tag{1.6}$$

$$\eta_{12}'(\theta)/\eta_{12} = \left[(m^2-n^2)^2 + 4(2\eta_{12}/\eta_{11}+\eta_{12}/\eta_{22})m^2n^2\right]^{-1} \tag{1.7}$$

where $m = \cos\theta$ and $n = \sin\theta$.

Results for η_{11}', η_{22}', and η_{12}' are shown in Figures 1.8-10 where estimates for η_{11}, η_{22}, and η_{12} are taken from reference [1] as shown in Table 1.2. Estimates for the viscosities could also be obtained from the relations given in equations (3a-3c). The dependence of the principal elongational viscosity upon fiber aspect ratio (L/D) is apparent in Figure 1.8. For systems with L/D=10^4 the ratio of transformed elongational viscosity to principal elongational viscosity, η_{11}'/η_{11} is 10^{-2} at θ=1°. Hence, fiber aspect ratios which correspond to actual material systems such as that discussed in reference [8] yield highly anisotropic materials systems whose properties exhibit extreme sensitivity to fiber orientation. A similar result for η_{22}'/η_{22} is shown in Figure 1.9 for L/D=10^4. For the apparent inplane shearing viscosity η_{12}'/η_{12}, the maximum occurs at $\theta = \pi/4$ with a value of approximately 10^1 as shown in Figure 1.10. It is interesting to note that while both the elongational viscosities varied over 10^0 to 10^{-6} for the range in orientation angle of 0 to $\pi/2$, the inplane shearing viscosity ratio only varied over 10^0 to 10^1 for L/D=10^4.

1.3.3 Ensemble Properties

Should the material system consist of an ensemble of elements (fibers) with varying orientation, the expected value of the viscosities for the ensemble will be different from the values obtained from equations 1.5-1.7. In fact, even with small misalignments the effective viscosities may be drastically different. The effective viscosities will be bounded by average values as determined by assuming constant stress or constant strain. In the following, only the expected values based on constant stress will be presented. This will illustrate the large changes in effective viscosity due to small misorientations.

To determine the expected values of the viscosities, a distribution function, $\phi(\theta)$, representing the fiber orientation is determined and a weighted average of the compliance matrix is calculated as shown below.

$$\langle \eta_{ij} \rangle_\beta = \left[\int_{-\pi/2}^{\pi/2} \beta'_{ij}(\theta)\phi(\theta)d\theta \right]^{-1} \tag{1.8}$$

where the compliance terms, $\beta'_{ij}(\theta)$, are defined as follows:

$$\beta'_{11} = m^4/\eta_{11} + (-1/\eta_{11}+1/\eta_{12})\, m^2n^2 + n^4/\eta_{22} \tag{1.9}$$

$$\beta'_{22} = n^4/\eta_{11} + (-1/\eta_{11}+1/\eta_{12})\, m^2n^2 + m^4/\eta_{22} \tag{1.10}$$

$$\beta'_{66} = m^4/\eta_{12} + (8/\eta_{11}+4/\eta_{22}-2/\eta_{12})\, m^2n^2 + n^4/\eta_{12} \tag{1.11}$$

If the fibers are assumed to be uniformly distributed between $\pm\theta_1$, the normalized probability density function is

$$\begin{aligned} &\phi = 0,\ \theta > \theta_1 \text{ and } \theta < -\theta_1 \\ &\phi = 1/2\theta_1\ ,\ -\theta_1 \le \theta \le \theta_1 \end{aligned} \tag{1.12}$$

Combining equations (1.8) through (1.12) yields the expected value of the viscosities based on the compliance matrix:

$$\begin{aligned} \langle \eta_{11} \rangle/\eta_{11} = {} & 32\theta_1\eta_{22}\eta_{12}/\big[(2\eta_{22}\eta_{12}+3\eta_{11}\eta_{12}+\eta_{11}\eta_{22})\ 4\theta_1 \\ & + (\eta_{12}\eta_{22}-\eta_{11}\eta_{12})\ 8\sin2\theta_1 + (2\eta_{22}\eta_{12}+\eta_{11}\eta_{12}-\eta_{11}\eta_{22})\ \sin4\theta_1\big] \end{aligned} \tag{1.13}$$

$$\begin{aligned} \langle \eta_{22} \rangle/\eta_{22} = {} & 32\theta_1\eta_{11}\eta_{12}/\big[(2\eta_{22}\eta_{12}+3\eta_{11}\eta_{12}+\eta_{11}\eta_{22})\ 4\theta_1 \\ & + (\eta_{11}\eta_{12}-\eta_{22}\eta_{12})\ 8\sin2\theta_1 + (2\eta_{22}\eta_{12}+\eta_{11}\eta_{12}-\eta_{11}\eta_{22})\ \sin4\theta_1\big] \end{aligned} \tag{1.14}$$

$$\begin{aligned} \langle \eta_{12} \rangle/\eta_{12} = {} & 8\theta_1\eta_{11}\eta_{22}/\big[(\eta_{11}\eta_{22}+2\eta_{12}\eta_{22}+\eta_{11}\eta_{12})\ 4\theta_1 \\ & + (\eta_{11}\eta_{22}-2\eta_{12}\eta_{22}-\eta_{11}\eta_{12})\ \sin4\theta_1\big] \end{aligned} \tag{1.15}$$

Consider the expected value of the principal elongational viscosity $\langle \eta_{11} \rangle$ for a fiber ensemble with equal probability of fiber orientation between $\pm\theta_1$. The expected viscosity for a range of values of θ_1 are shown in Figure 1.11. These results indicate that the compliance method mirrors the significant sensitivity to orientation shown for η'_{11} in Figure 1.8. Therefore for small misalignment of the fibers the apparent viscosity is greatly reduced.

For the expected value of the transverse elongational viscosity $\langle \eta_{22} \rangle$ of the ensemble, there is little dependence on the misorientation as shown in Figure 1.12. Similar results for the expected value of the shearing viscosity $\langle \eta_{12} \rangle$ are shown in Figure 1.13.

1.4 Conclusions

Relations for predicting the effective viscosities of an aligned discontinuous fiber filled fluid developed in [1-3] for Newtonian and power law fluids have been extended to include zero-shear viscosity and temperature dependence. This was accomplished by describing the matrix fluid viscosity with a Carreau model. Using experimentally determined viscosity data for PEEK, effective properties of a fiber assembly were predicted. It was shown that the introduction of fibers into the fluid can dramatically decrease the maximum Newtonian strain rate. This is critical when determining a maximum strain rate for which Newtonian behavior is expected. The effect of the Carreau model parameters on the elongational viscosity were demonstrated for a wide range of values.

In addition to long discontinuous fiber systems, the relationships presented in this chapter, all but the longitudinal elongational viscosity prediction, are valid for continuous fiber systems. It should be kept in mind that these relations provide insight into the relative magnitudes of the predicted properties, the effect of material descriptors, and the degree of anisotropy of the medium.

The influence of fiber orientation upon the effective viscosities of a medium consisting of discontinuous fibers suspended in a viscous medium have been determined for the conditions of perfect collimation and off-axis orientation, as well as ensemble misorientation. In the former case extreme sensitivity to fiber orientation was exhibited by all the viscosity terms corresponding to materials with aspect ratios of 10^3 - 10^4. Reduction in the ratio of apparent elongational viscosity to principal elongational viscosity of 10^{-2} for an orientation of 1° was observed.

The compliance matrix was utilized to predict the expected values for the anisotropic viscosities of the medium consisting of an ensemble of misoriented fibers in a viscous medium. This averaging approach yielded results for the expected values of viscosities which display the same tendencies as the properties for the off axis perfect collimation results. It was shown that small misalignments in the fibers could greatly decrease the longitudinal elongational viscosities without corresponding effects on the transverse elongational and inplane shearing viscosities.

Table 1.1

Summary of Viscosity Predictions [3]

Term	Newtonian Fluid
η_{11}/η	$\frac{f}{2}\left[\frac{1-\mu}{\mu}\right](L/D)^2$
η_{12}/η	$\frac{1}{2}\left[\frac{1+\mu}{\mu}\right]$
η_{23}/η	$\frac{1}{\mu}$
η_{22}/η	$\frac{4}{\mu}$

Table 1.2

Plane Stress Orthotropic Viscosities

	Micromechanics Predictions (1)
Volume fraction : 0.6	$\eta_{11}/\eta = 2.08\ (L/D)^2$
Packing geometry : square array	$\eta_{12}/\eta = 4.47$
	$\eta_{22}/\eta = 31.8$

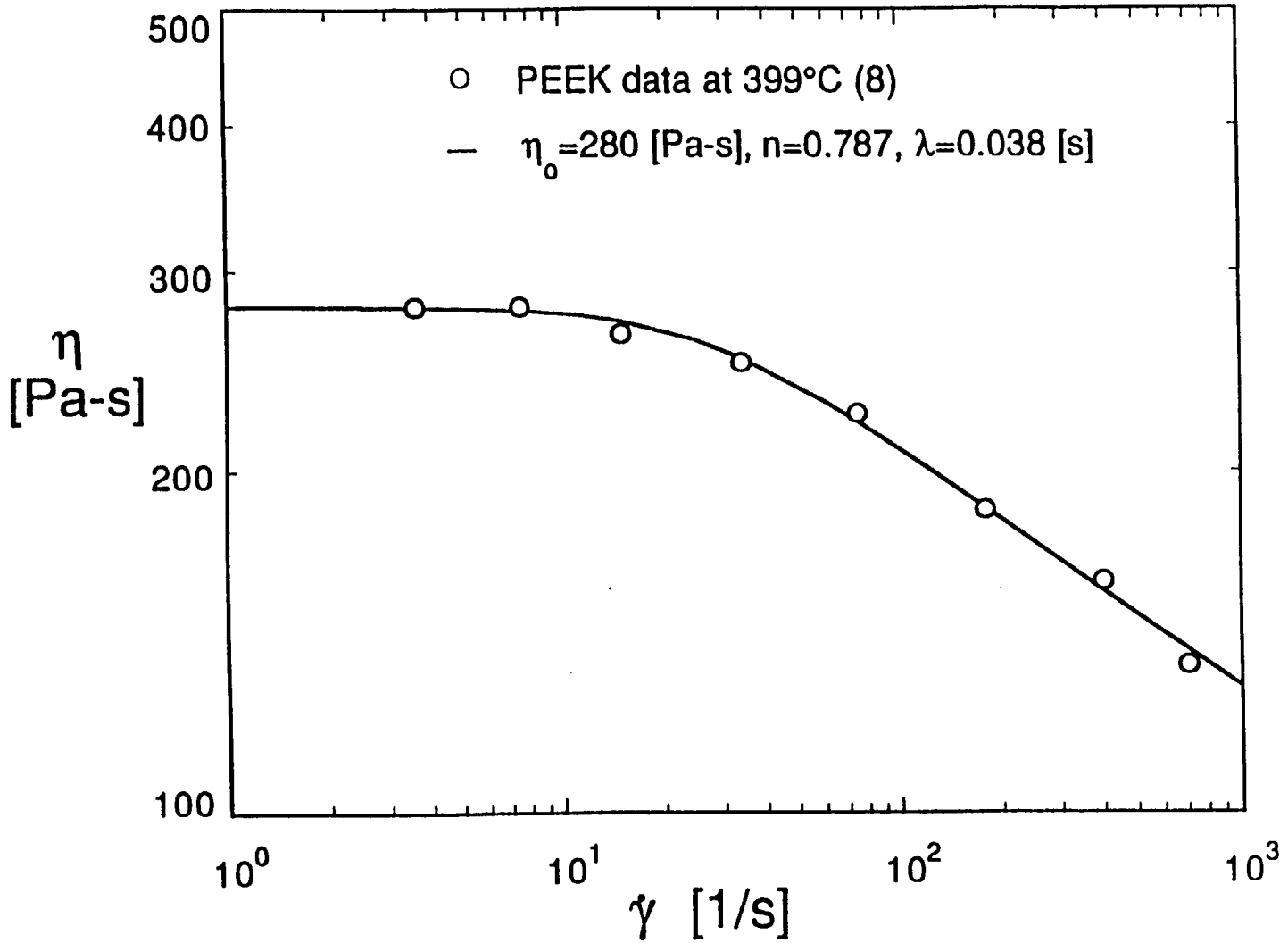

Figure 1.1 Experimental Data for Viscosity vs. Shear Rate for PEEK at 399° C

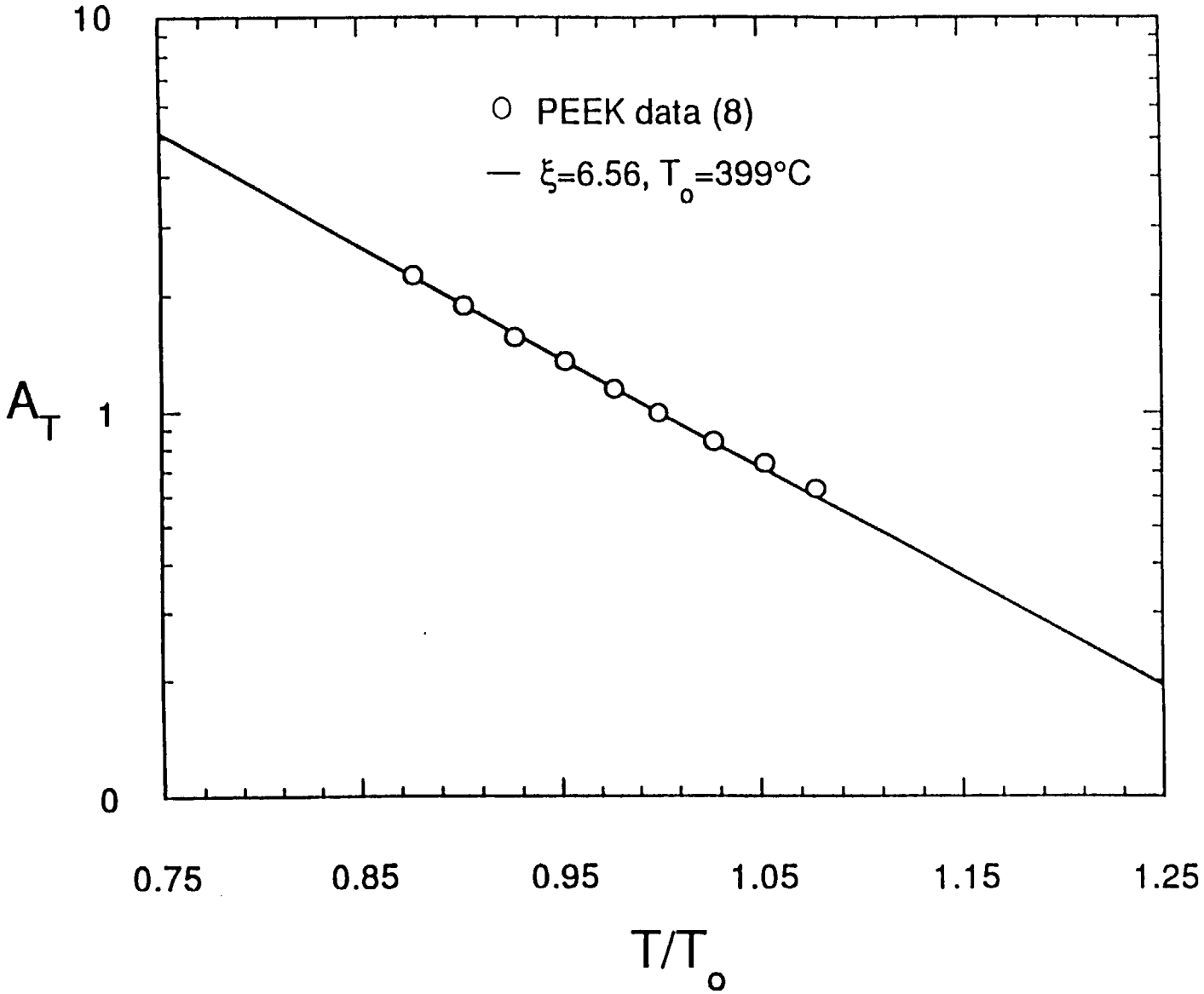

Figure 1.2 Experimental Data for Temperature Shift Factor vs. Temperature for PEEK

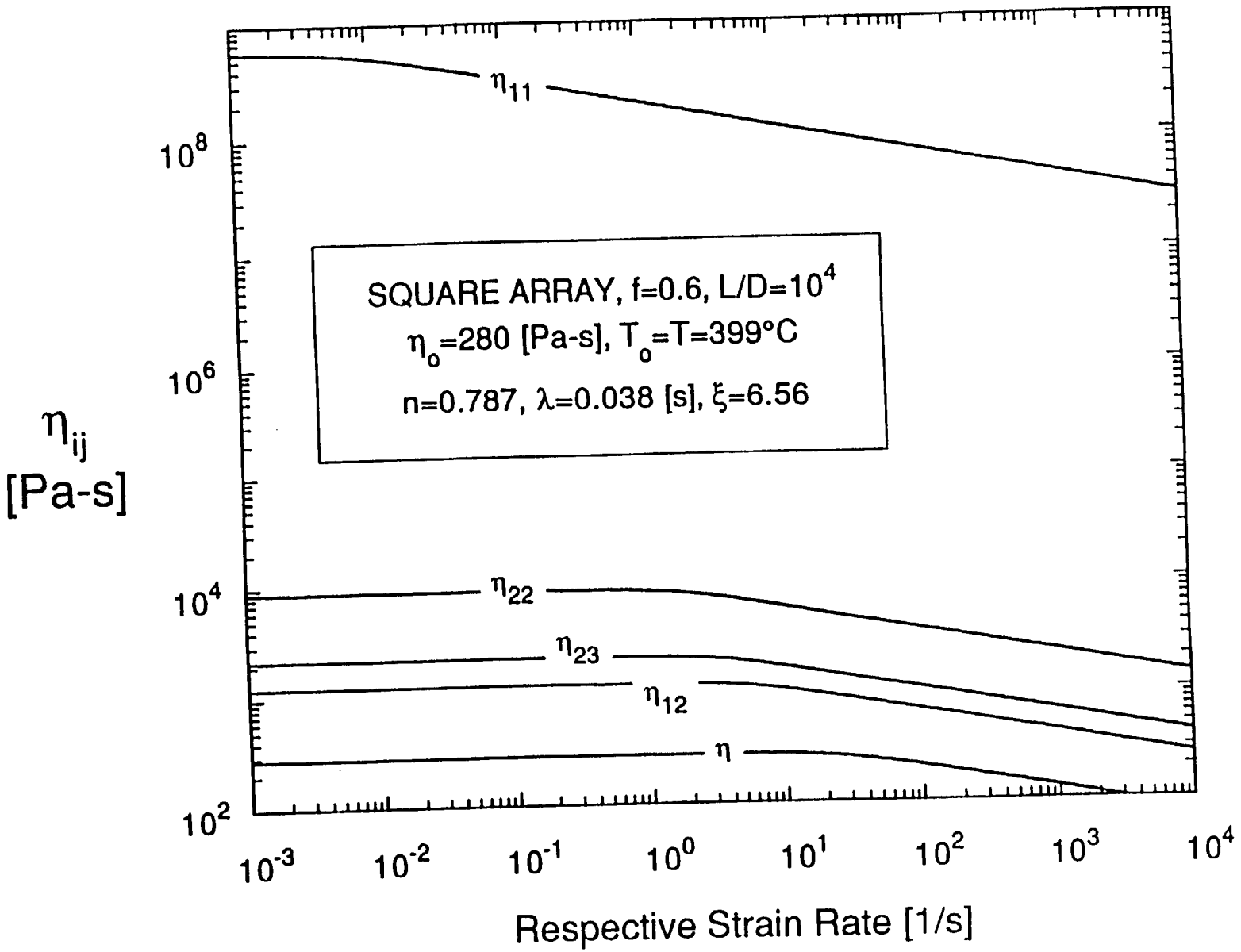

Figure 1.3 Effective Viscosities vs. Strain Rate for Fiber Reinforced PEEK at 399° C

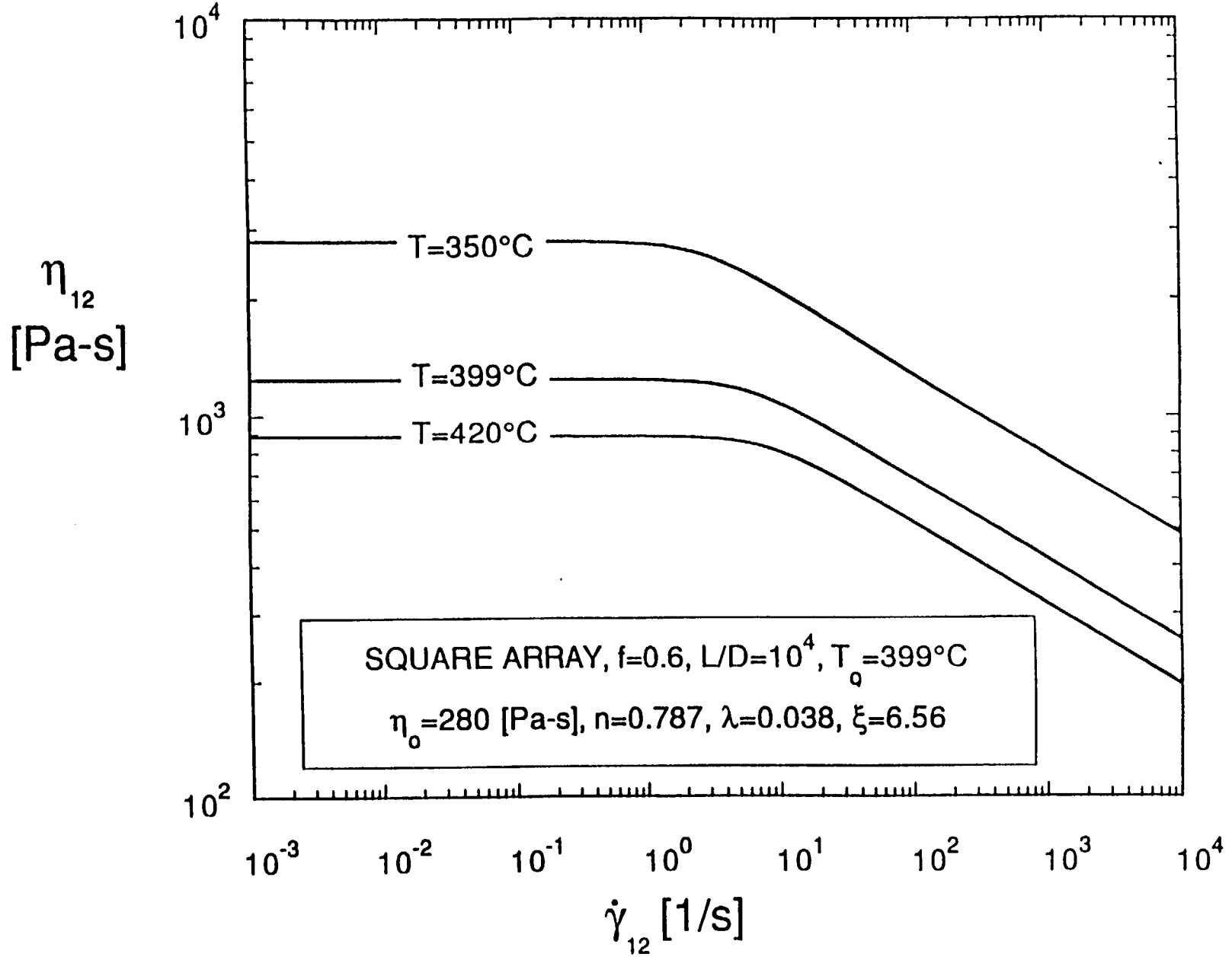

Figure 1.4 Effect of Temperature on Inplane Shearing Viscosity vs. Strain Rate for Fiber Reinforced PEEK

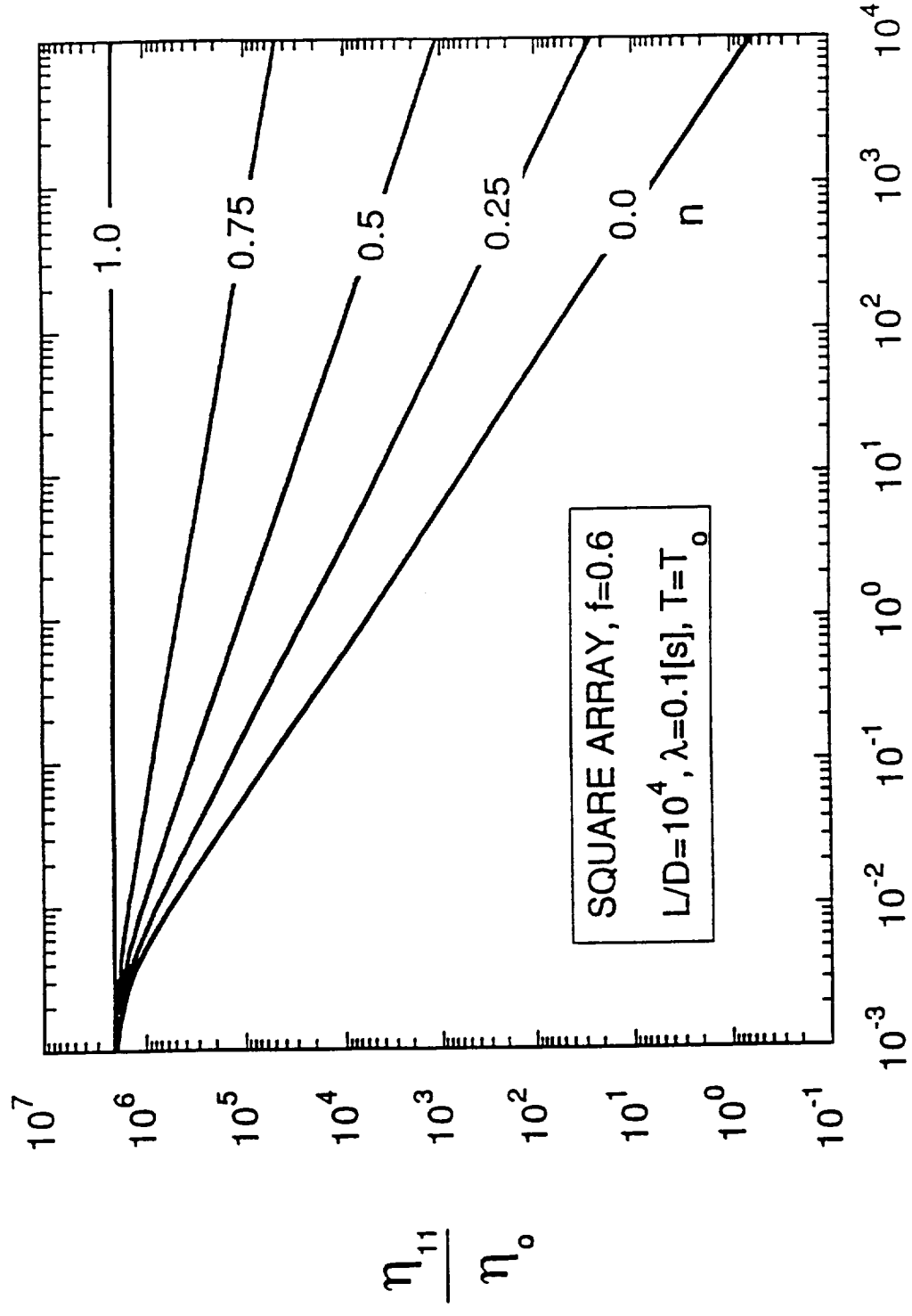

Figure 1.5 Effect of Power Law Exponent on Longitudinal Elongational Viscosity vs. Strain Rate

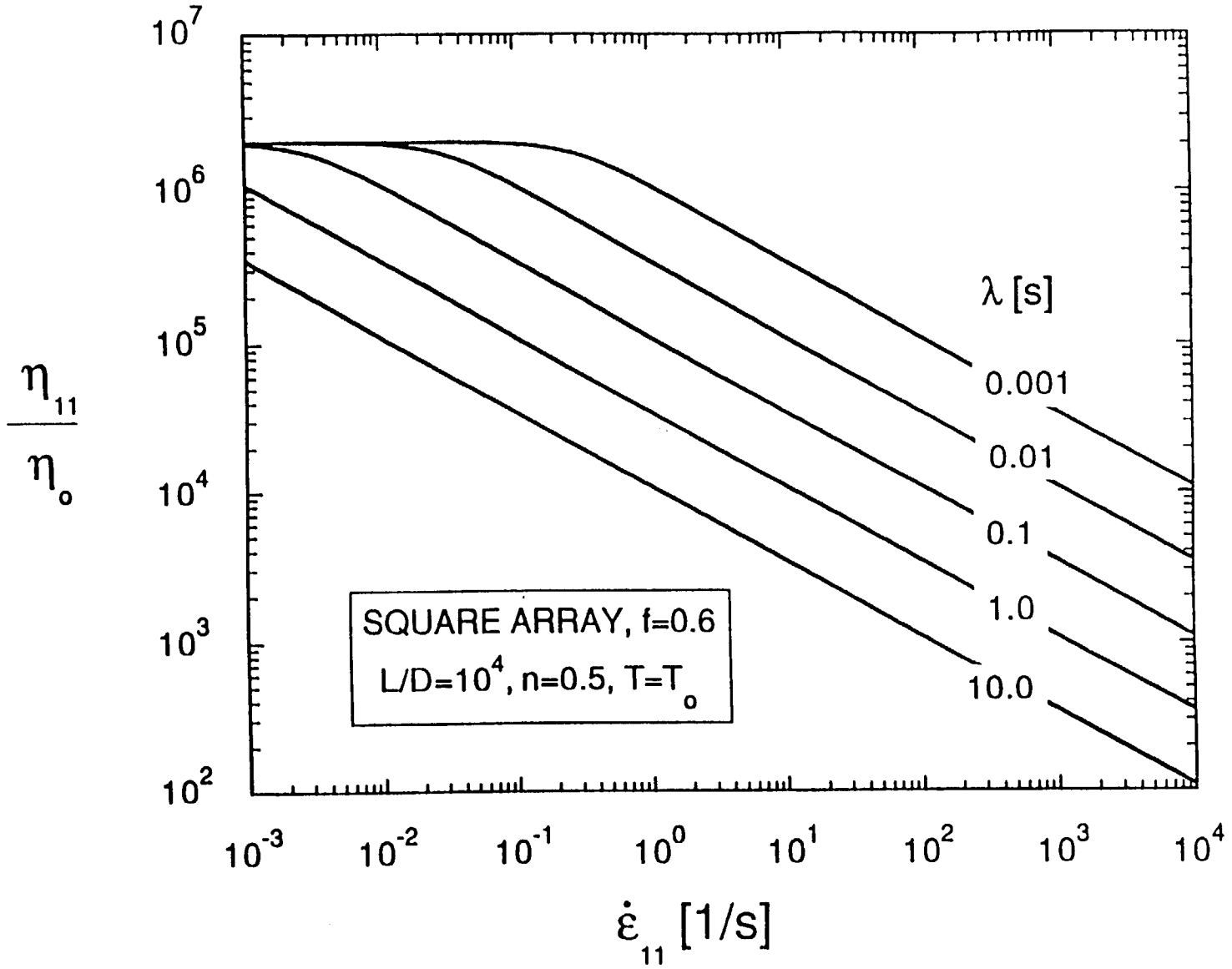

Figure 1.6 Effect of Time Constant on Longitudinal Elongational Viscosity vs. Strain Rate

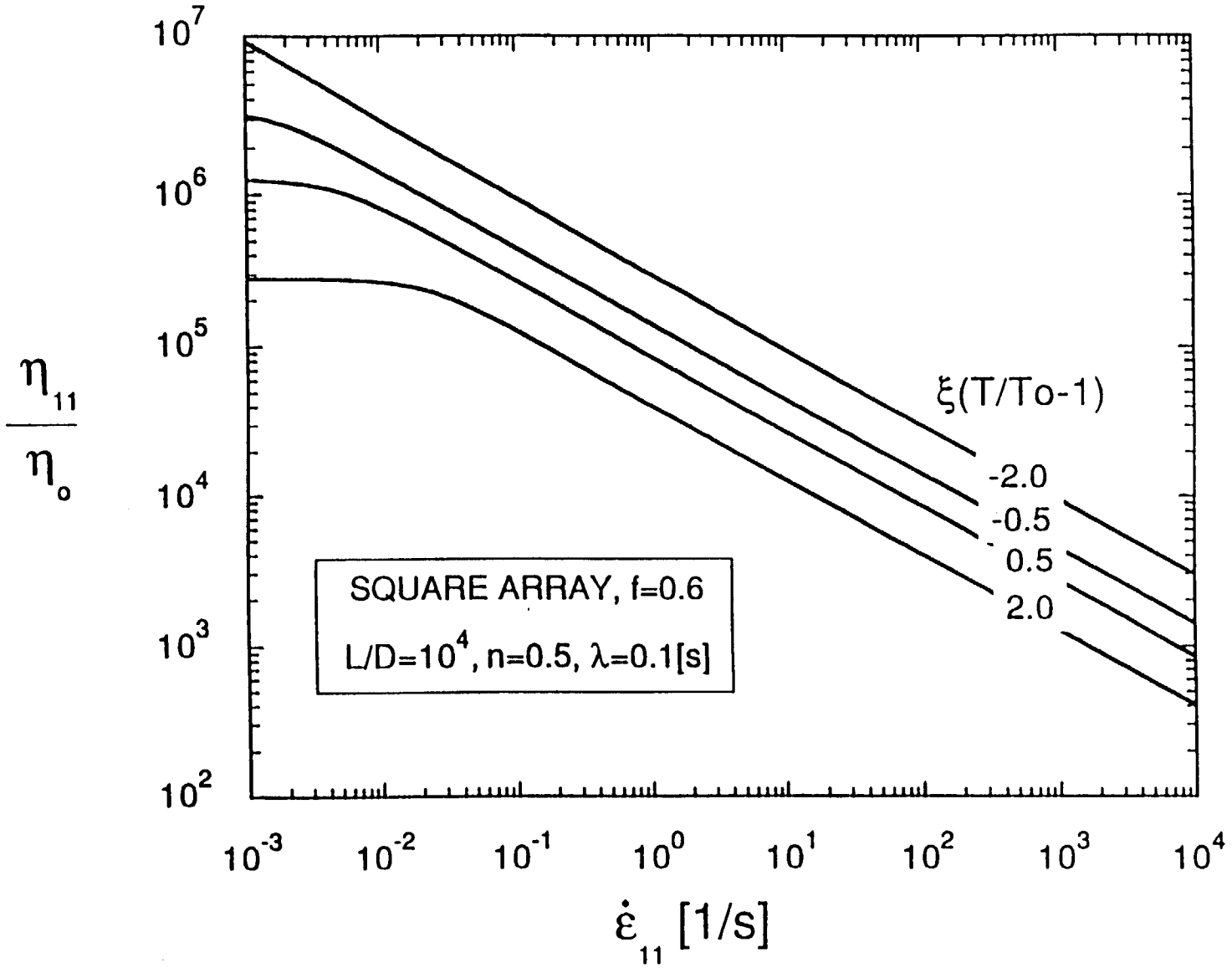

Figure 1.7 Effect of Temperature on Longitudinal Elongational Viscosity vs. Strain Rate

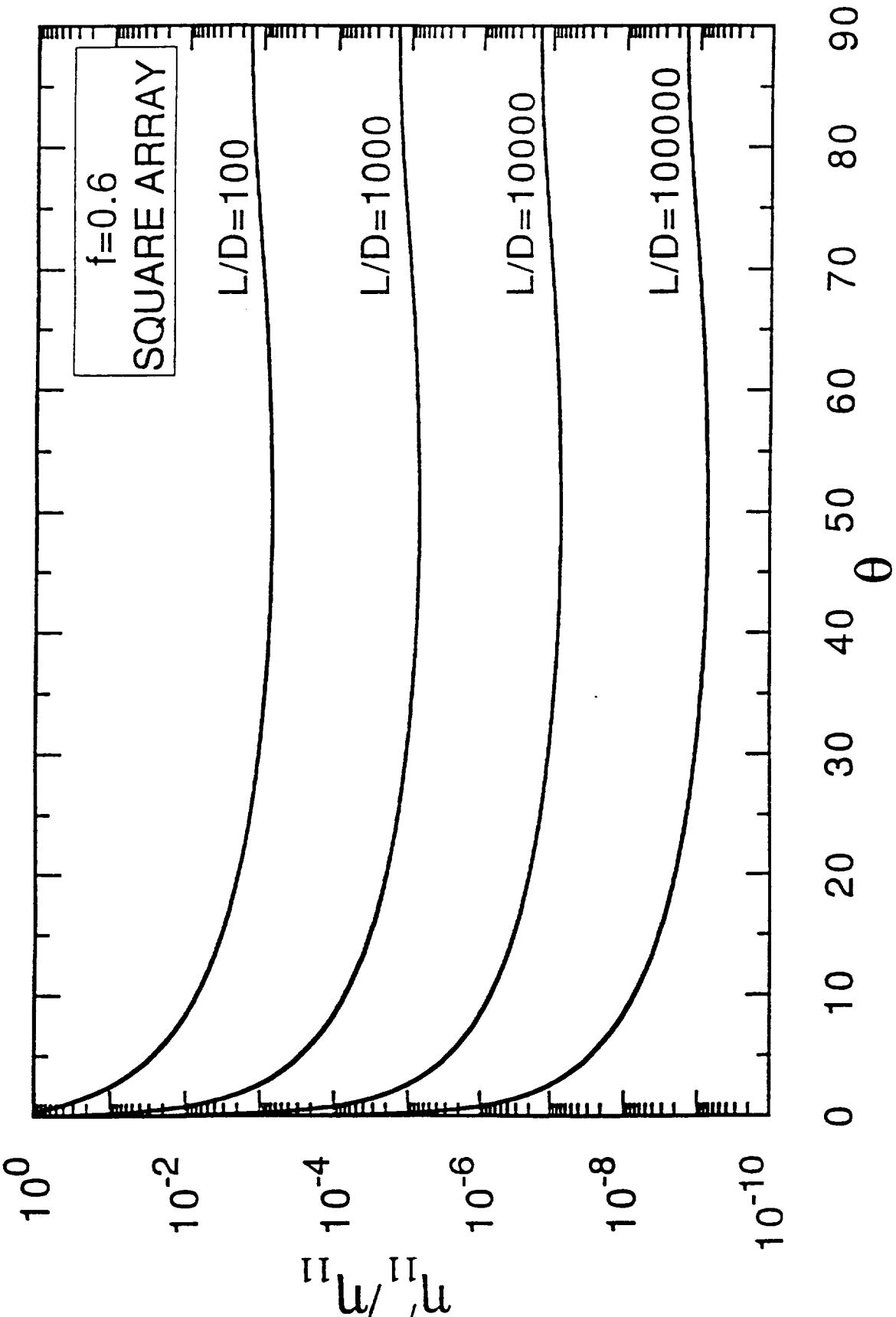

Figure 1.8 Influence of Fiber Orientation on Longitudinal Elongational Viscosity

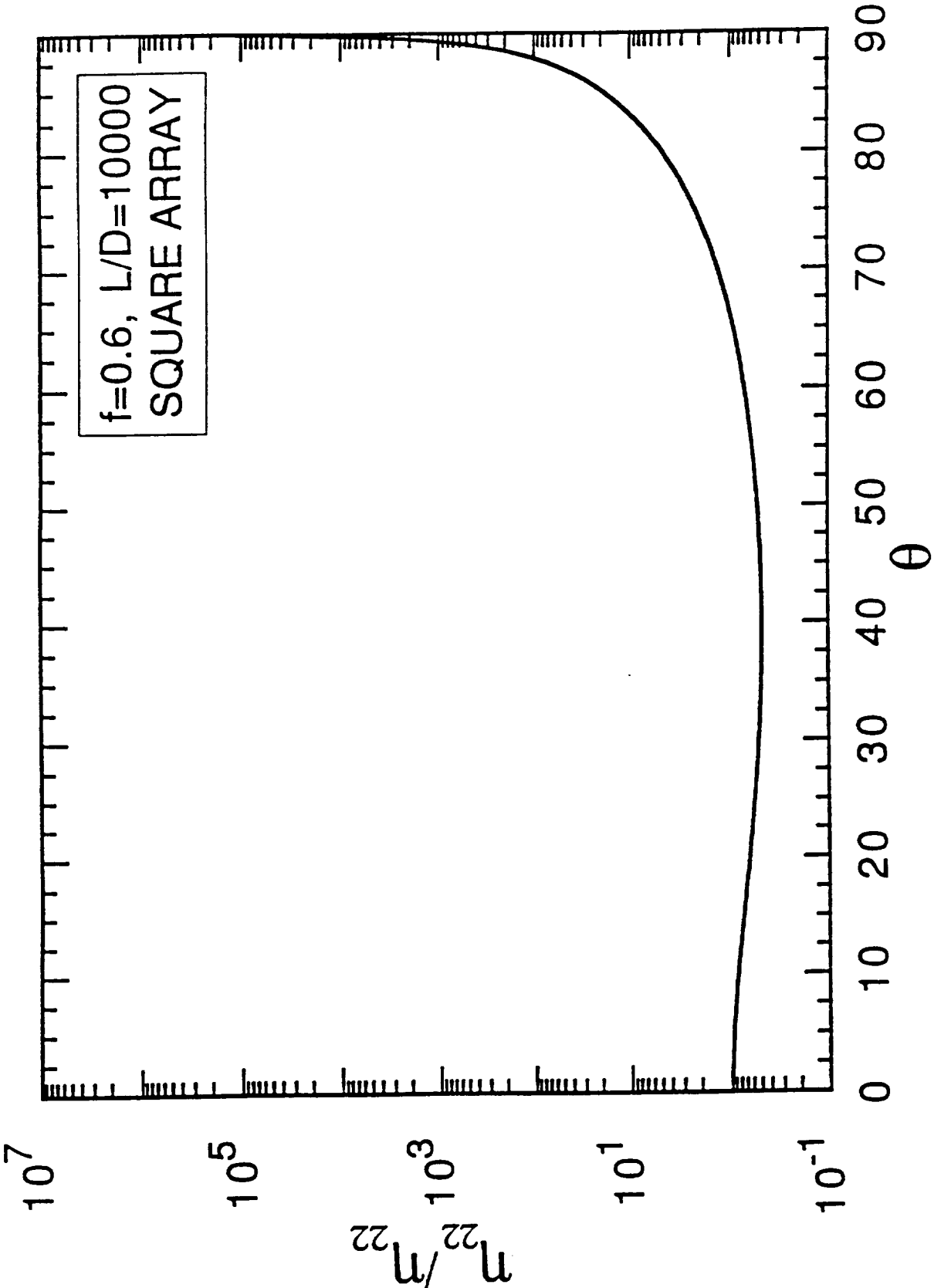

Figure 1.9 Influence of Fiber Orientation on Transverse Elongational Viscosity

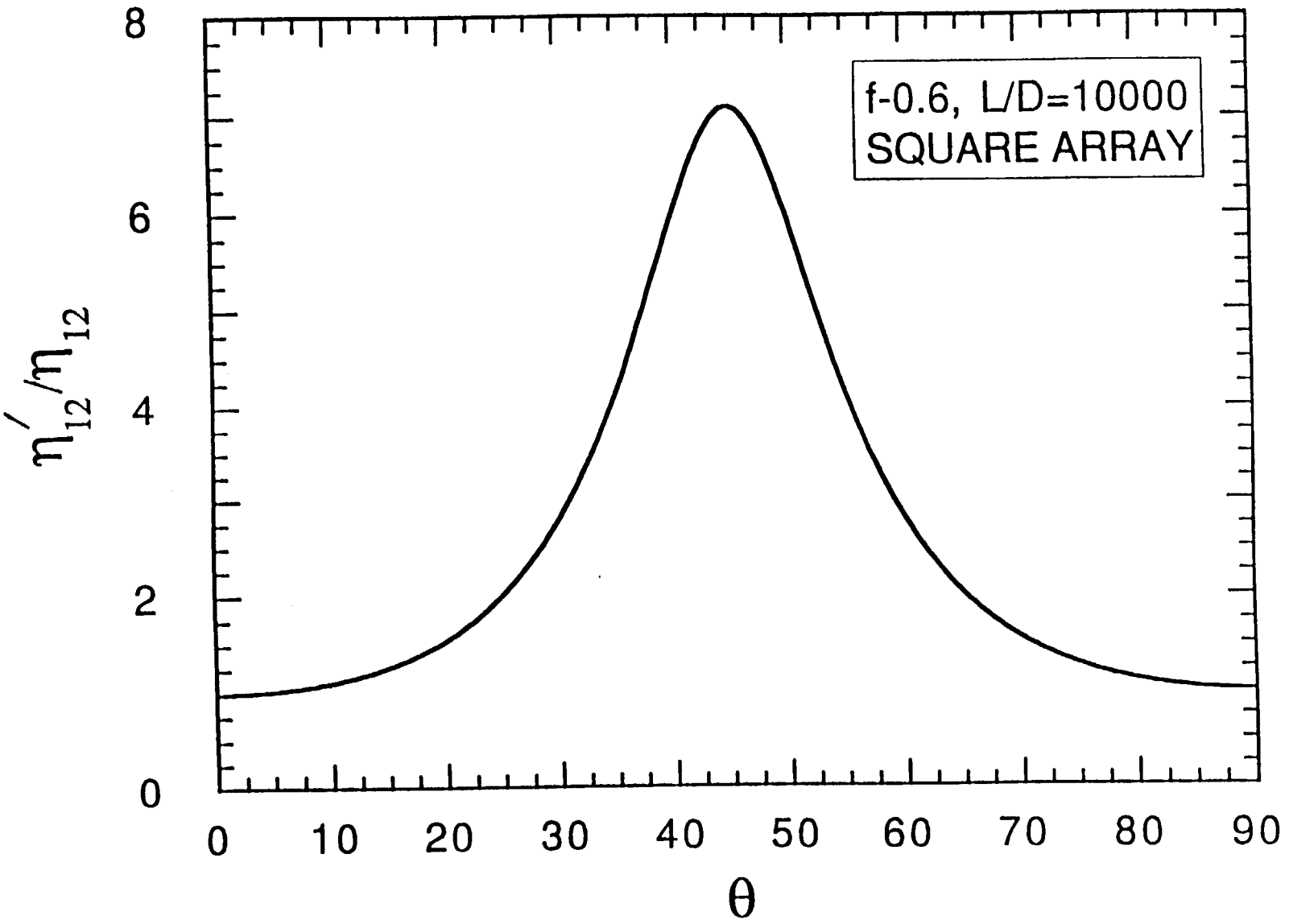

Figure 1.10 Influence of Fiber Orientation on Inplane Shearing Viscosity

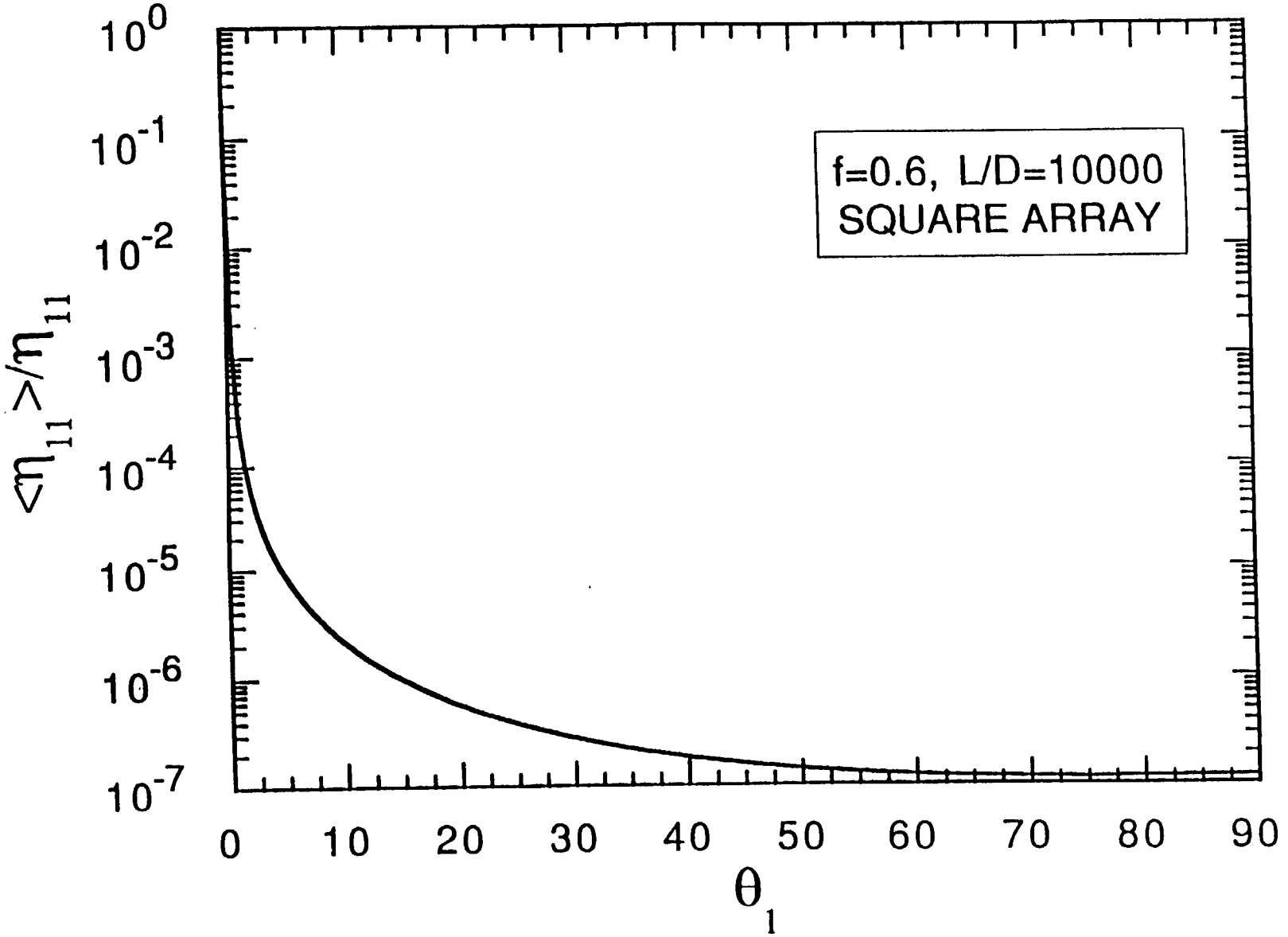

Figure 1.11 Expected Value for Longitudinal Elongational Viscosity

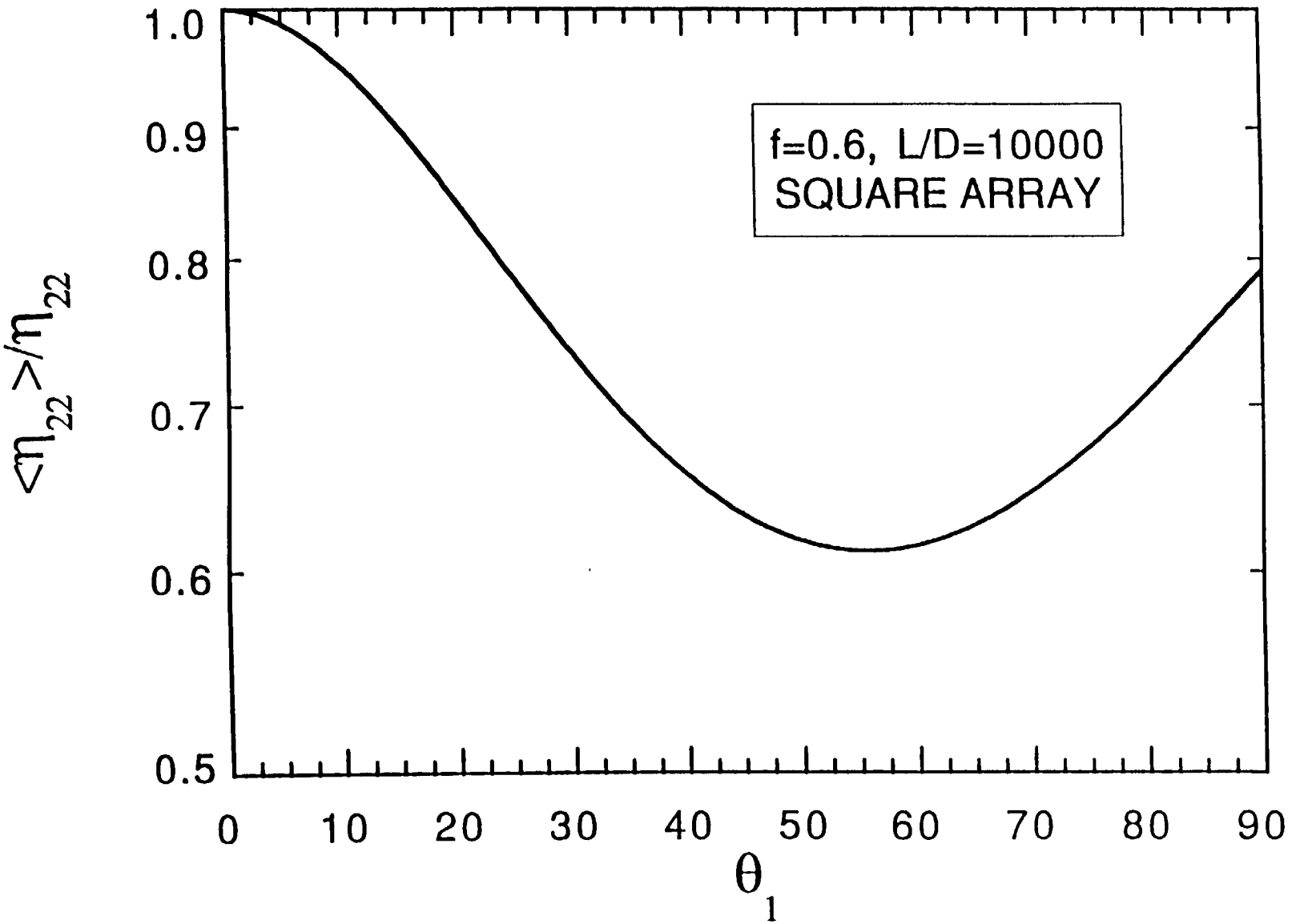

Figure 1.12 Expected Value for Transverse Elongational Viscosity

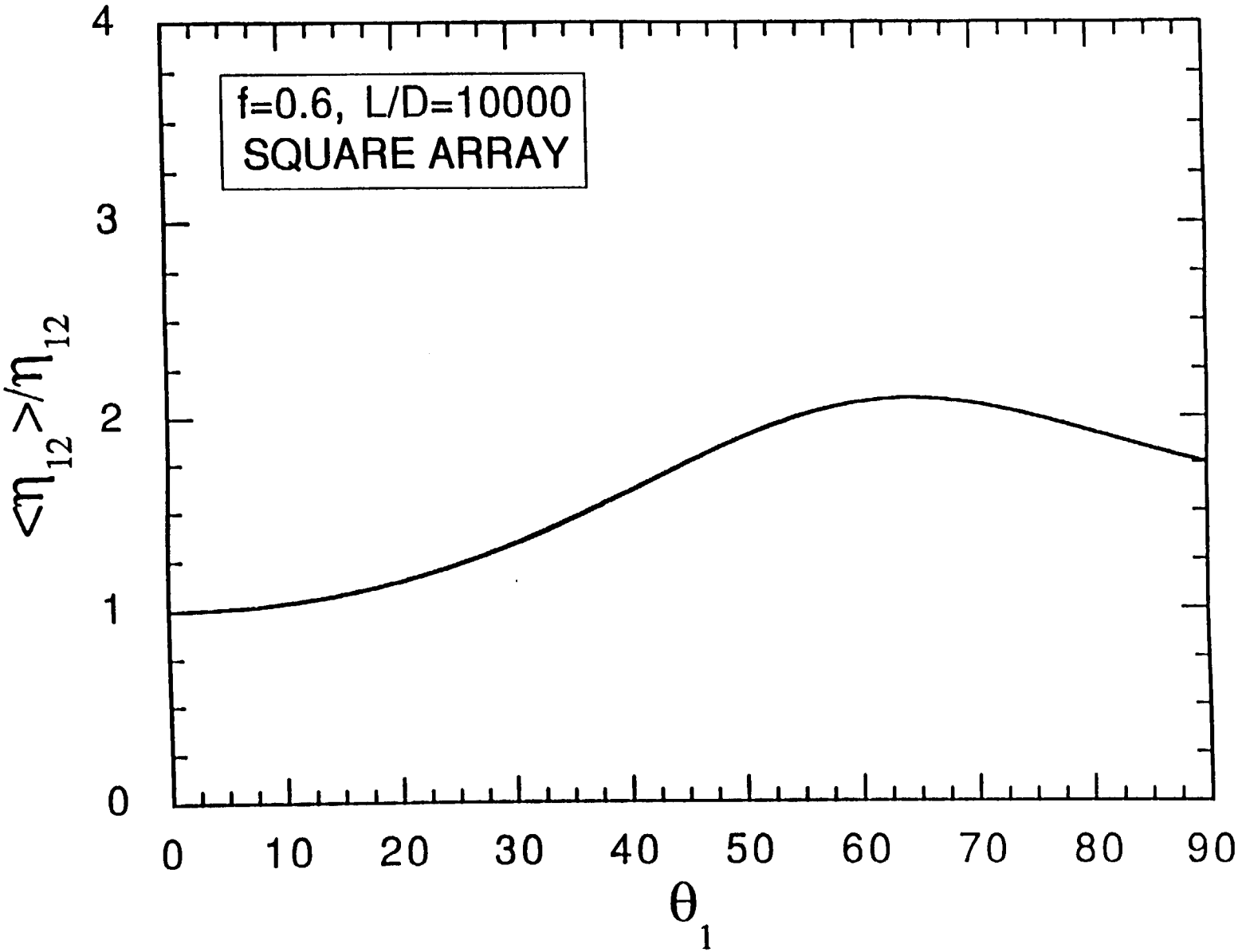

Figure 1.13 Expected Value for Inplane Shearing Viscosity

2.0 The Effect of Material Heterogeneity in Curved Composite Beams

2.1 Introduction

Manufacturing processes such as sheet forming and stretch forming can be used to produce several types of composite parts [9, 10]. The use of a long discontinuous fiber material system allows for material stretching over complex curvature parts while maintaining a high percentage of the continuous fiber material properties [11]. Combination of these forming methods and material system allows the production of complex structures such as curved beams as shown in Figure 2.1. The microstructure of a curved beam is sensitive to the production method and gradients in material properties are expected in both sheet formed [12] and stretch formed [10] beams. Schematic examples of two types of heterogeneity are shown in Figure 2.2; analysis of these types of beams can be useful in determining the effect of such property gradients on the overall performance of a given beam.

Two separate analyses are conducted. The first uses a closed form stress potential approach to investigate the effect of radial heterogeneity on curved beams loaded in pure bending. The stress state is found for beams which can have several different geometries including I, J, T, and rectangular cross-sections. Material properties can be specified independently for each section of the beam, i.e., flange and web can have different properties. Each section of the beam is treated as an individual curved rectangular beam loaded in pure bending and with a constant distributed load on the curved surfaces. Superposition is used to combine the results of the individual sections into the total beam solution. Details of the analysis are provided and results are shown for comparison with known solutions.

The second analysis technique uses a Rayleigh-Ritz approach to solve the minimum potential energy equation for several curved beam problems including pure bending and a beam with a uniform distributed load. This is an approximate solution which uses an assumed series formulation of the displacement field. The advantage of this method is that it allows for any type of material heterogeneity and can be used to solve other relevant problems such as tensile loaded beams or beams with geometric stress concentrations such as cutouts.

Analysis results are compared to solutions found by using mechanics of materials and finite element methods. The mechanics of materials solutions are useful for comparing results for beams with homogeneous material properties and the finite element analysis is necessary to solve the problem when the beam has heterogeneous material properties. The first type of analysis has been incorporated into a design tool for analyzing curved beams loaded in pure bending. A wide range of geometric parameters and material properties can be analyzed with relative ease. The second type of analysis is being developed so that a similar tool can be used to analyze curved beams with different loading conditions or geometric configurations.

2.2 Stress Potential Solution Procedure

The state of stress and strain is determined for a curved beam loaded in pure bending which has any of the following cross-sections; I-beam, T-beam, J-beam, etc. The solution is found by separating the beam into three sections; each with an applied bending moment and distributed load. A stress potential approach is used to solve the two-dimensional problem in each section. The constitutive relations take the form;

$$\varepsilon_i = \alpha_{ij}\, r^{-n}\, \sigma_j \;;\quad i, j = 1, \tag{2.1}$$

where ε is the two-dimensional strain vector in polar coordinates, σ is the corresponding stress vector, r is the radial position, and α_{ij} are the base values of the elements of the compliance matrix;

$$\alpha_{11} = a^n/E_{11} \;,\quad \alpha_{12} = \alpha_{21} = -\nu_{12}\, a^n/E_{12} \;,\quad \alpha_{22} = a^n/E_{22} \;, \tag{2.2}$$

and a is the inside radius of the beam. The degree of radial heterogeneity, n, allows for a property gradient in the radial direction of the beam. A positive 'n' defines a beam which is stiffer with increasing radius, a negative 'n' defines a beam which is more compliant with increasing radius and homogeneous material properties are specified by letting n = 0. Base values for the material properties are defined along the inside radius of the beam. This constitutive relation, together with equilibrium and compatibility can be combined to form the equation;

$$\nabla^4 \phi = 0, \tag{2.3}$$

where ϕ is the stress potential. We can solve for ϕ by applying boundary conditions to the two-dimensional curved beam as shown in Figure 2.3; the tractions along the straight edges are represented by a bending moment, M, and the curved surfaces are traction free. The resulting stresses are [13]:

$$\sigma_r = -\frac{M}{b^2 h g}\left[\frac{c^t - c^{n+1}}{c^s - c^t}\,\rho^{s-1} + \frac{c^{n+1} - c^s}{c^s - c^t}\,\rho^{t-1} + \rho^n\right],$$

$$\sigma_\theta = -\frac{M}{b^2 h g}\left[\frac{c^t - c^{n+1}}{c^s - c^t}\,s\,\rho^{s-1} + \frac{c^{n+1} - c^s}{c^s - c^t}\,t\,\rho^{t-1} + (n+1)\,\rho^n\right], \tag{2.4}$$

where,

$$g = \frac{(c^t - c^{n+1})(1 - c^{s+1})}{c^s - c^t}\,\frac{s}{s+1} + \frac{(c^{n+1} - c^s)(1 - c^{t+1})}{c^s - c^t}\,\frac{t}{t+1} + \frac{(n+1)}{(n+2)}\,(1 - c^{n+2}) \;, \tag{2.5}$$

$$\binom{s}{t} = \frac{1}{2}\left(n \pm \sqrt{n^2 + 4\,\gamma_n}\right) \;,\quad \gamma_n = \frac{(\alpha_{11} + n\,\alpha_{12})}{\alpha_{22}} \;, \tag{2.6}$$

and h is the beam thickness, c is the ratio of the inside radius to the outside radius (c = a/b), and ρ is the ratio of radial position to outside radius (ρ = r/b). Notice that the solution is axisymmetric and $\sigma_{r\theta} = 0$ everywhere.

Another loading condition that produces an axisymmetric state of stress in a curved beam is the classic Lame's problem, which is a circular cylinder with an internal and external pressure. The stresses in such a cylinder are [13]:

$$\sigma_r = - P c \frac{\rho^{s-1} - \rho^{t-1}}{c^s - c^t} + Q \frac{c^t \rho^{s-1} - c^s \rho^{t-1}}{c^s - c^t}$$

$$\sigma_\theta = - P c \frac{s \rho^{s-1} - t \rho^{t-1}}{c^s - c^t} + Q \frac{s c^t \rho^{s-1} - t c^s \rho^{t-1}}{c^s - c^t} \tag{2.7}$$

where P is the internal pressure, Q is the external pressure, and all the other variables are the same as in the pure bending case. When looking at a section of the cylinder, as shown in Figure 2.4, the straight edges are not traction free; the tractions can be represented by an end moment and an end load analogous to hoop stress found in a thin walled cylinder. The end load, L, is determined by integrating the tangential stress across the depth of the beam and the end moment, M_L, is found by integrating the tangential stress times the radius across the depth of the beam.

2.2.1 Superposition of Two-Dimensional Solutions

Now that the solution for the stresses has been established in each individual section under the general loading shown in Figure 2.5, superposition is used to find the solution of the entire beam. The curved I-beam, for example, loaded with a bending moment, M, is separated into three sections with the following bending moments and distributed loads: M_1, M_2, M_3, P_2, P_3, Q_1, and Q_2, as shown in Figure 2.5. Applying superposition; the sum of the moments on the section ends must be equal to the applied moment, M:

$$M_1 + M_2 + M_3 + M_{L1} + M_{L2} + M_{L3} = M \tag{2.8}$$

where M_1, M_2, and M_3 are bending moments applied at each section end and M_{L1}, M_{L2}, and M_{L3} are the bending moments due to the applied distributed loads Q_1, P_2 and Q_2, and P_3, respectively.

Six more equations are necessary to solve this problem. The sections must be in equilibrium where they meet, therefore the radial loads must be equal resulting in the following relations:

$$P_2 h_2 = Q_1 h_1 \quad \text{and} \quad P_3 h_3 = Q_2 h_2 \tag{2.9}$$

where h_1, h_2, and h_3 are the thickness of each section and the P's and Q's are the applied pressures. The final equations are found by requiring the continuity of radial and tangential displacements at the section boundaries,

$$u_r^{(1)} = u_r^{(2)}, \text{ at } r = b \qquad u_r^{(2)} = u_r^{(3)}, \text{ at } r = c$$

$$u_\theta^{(1)} = u_\theta^{(2)}, \text{ at } r = b \qquad u_\theta^{(2)} = u_\theta^{(3)}, \text{ at } r = c. \tag{2.10}$$

These seven equations (2.8) - (2.10) are solved simultaneously for the seven unknowns; M_1, M_2, M_3, P_2, P_3, Q_1, and Q_2. The stresses, strains and displacements can be found in each section based on these loading conditions.

2.3 General Heterogeneity Stress Analysis

A Rayleigh-Ritz stress analysis method is used to solve several problems including pure bending of a curved beam and a uniform distributed load on beams and rings with various cross-sections. This method uses an assumed displacement field which contains unknown parameters and satisfies the boundary conditions of the specific problem of interest. The displacement field is substituted into the principal of virtual work, resulting in a system of linear equations which is then solved for the unknown parameters. Displacements, strains, and stresses can be determined when these parameters are substituted into the assumed displacement field. This method allows for the calculation of stresses in components without the need for elaborate pre- and post-processing; which is especially convenient for parts with complex heterogeneous material properties and geometry. The solution procedure is outlined below and then two types of problems are solved using different assumed displacement fields.

2.3.1 Rayleigh-Ritz Method

The principle of minimum potential energy states that of all displacement fields which satisfy the prescribed constraint conditions, the correct state is that which makes the total potential energy, Π, of the structure a minimum [14]. The potential energy of the structure is the sum of the elastic strain energy, U, and the potential of the external forces, V. The minimum potential energy is found by setting its first variation equal to zero, $\delta \Pi = \delta U + \delta V = 0$; which can be expanded to the following expression for a two-dimensional body:

$$\int_A \delta\{\varepsilon\}^T\{N\}\, dA - \int_S \delta\{u\}^T\{t\}\, dS = 0. \qquad (2.11)$$

where,

$\{\varepsilon\}$ = strain vector
$\{N\}$ = stress resultant vector
$\{u\}$ = displacement vector
$\{t\}$ = applied surface traction vector

and A is the in-plane area of the two-dimensional structure and S is the curve which defines its boundary. We assume the following form of the displacement field;

$$u_r = \sum_{j=0}^{N} \sum_{k=1}^{M} q_j^k f_1(r,k)\, g_1(j,\theta) \quad , \quad u_\theta = \sum_{j=0}^{N} \sum_{k=1}^{M} q_j^{M+k} f_2(r,k)\, g_2(j,\theta)\,, \qquad (2.12)$$

where u_r and u_θ are the displacement components and q_j^k are unknown parameters. The functions f_1, f_2, g_1, and g_2 are chosen so that the displacements match symmetry and boundary conditions of the problem. The length of the two series are determined by the input variables N and M. The displacements can be written in matrix form;

$$\{u\} = \begin{Bmatrix} u_r \\ u_\theta \end{Bmatrix} = \sum_{j=0}^{N} [U_j] \{q_j\} , \tag{2.13}$$

where $\{q_j\}$ is a vector containing 2M unknown parameters and $[U_j]$ is a 2 x 2M matrix of the form:

$$[U_j] = \begin{bmatrix} f_1(r,1)\, g_1(j,\theta) & \dots & f_1(r,M)\, g_1(j,\theta) & 0 & \dots & 0 \\ 0 & \dots & 0 & f_2(r,1)\, g_2(j,\theta) & \dots & f_2(r,M)\, g_2(j,\theta) \end{bmatrix} \tag{2.14}$$

.

The strain vector is obtained by substituting equations (2.13) and (2.14) into the strain-displacement relations for polar coordinates:

$$\{\varepsilon\} = \begin{Bmatrix} \varepsilon_r \\ \varepsilon_\theta \\ \gamma_{r\theta} \end{Bmatrix} = \begin{bmatrix} \frac{\partial}{\partial r} & 0 \\ \frac{1}{r} & \frac{1}{r}\frac{\partial}{\partial \theta} \\ \frac{1}{r}\frac{\partial}{\partial \theta} & \frac{\partial}{\partial r} - \frac{1}{r} \end{bmatrix} \{u\} = \sum_{j=0}^{N} [H_j] \{q_j\} , \tag{2.15}$$

where $[H_j]$ is a 3 x 2M matrix which has the following form;

$$\begin{bmatrix} [f'_1(r,1) \dots f'_1(r,M)]\, g_1(j,\theta) & 0 \dots 0 \\ [\frac{1}{r} f_1(r,1) \dots \frac{1}{r} f_1(r,M)]\, g_1(j,\theta) & [\frac{1}{r} f_2(r,1) \dots \frac{1}{r} f_2(r,M)]\, \dot{g}_2(j,\theta) \\ [\frac{1}{r} f_1(r,1) \dots \frac{1}{r} f_1(r,M)]\, \dot{g}_1(j,\theta) & \left\{ [f'_2(r,1) - \frac{f_2(r,1)}{r}] \dots [f'_2(r,M) - \frac{f_2(r,M)}{r}] \right\} g_2(j,\theta) \end{bmatrix} \tag{2.16}$$

Differentiation with respect to r is denoted by $( )'$ and differentiation with respect to θ is denoted by $\dot{( )}$. The stress resultant vector is determined by applying the stress-strain relations;

$$\{N\} = \begin{Bmatrix} N_r \\ N_\theta \\ N_{r\theta} \end{Bmatrix} = \begin{bmatrix} A_{11} & A_{12} & A_{16} \\ A_{12} & A_{22} & A_{26} \\ A_{16} & A_{26} & A_{66} \end{bmatrix} \begin{Bmatrix} \varepsilon_r \\ \varepsilon_\theta \\ \gamma_{r\theta} \end{Bmatrix}, \tag{2.17}$$

where A_{11}, A_{12}, etc., are the elements of the material stiffness matrix and can be defined as constants or as functions of position. The stress resultant vector can also be written as;

$$\{N\} = [A]\{\varepsilon\} = \sum_{j=0}^{N} [A][H_j]\{q_j\}. \tag{2.18}$$

The principal of minimum potential energy is rewritten by substituting equations (2.13) - (2.18) into equation (2.11) which yields the following:

$$\int_A \sum_{j=0}^{N} \sum_{l=0}^{N} [H_j]^T [A][H_l]\{q_l\}\, dA - \int_S \sum_{j=0}^{N} [U_j]^T \{t\}\, dS = 0, \tag{2.19}$$

which can be written more compactly as:

$$[K]\{q\} = [T], \tag{2.20}$$

where $\{q\}$ is the vector of unknown parameters.The global stiffness matrix and the load vector, [K] and [T] respectively, are defined below:

$$[K] = \int_A \sum_{j=0}^{N} \sum_{l=0}^{N} [H_j]^T [A][H_l]\, dA \quad \text{and} \quad [T] = \int_S \sum_{j=0}^{N} [U_j]^T \{t\}\, dS. \tag{2.21}$$

The limits on the area and surface integrals are defined by the geometry of each problem to be solved. The applied surface traction vector $\{t\}$ is defined by the applied loading conditions, and all the other matrices are defined by the assumed displacement field and the material properties. Solutions are found for two problems requiring different assumed displacement fields.

2.3.2 Solution Procedure for Problems With Two Planes of Symmetry

Two different problems involving two-dimensional plates with two planes of symmetry are solved using the same assumed displacement. The first problem solved is a circular ring loaded by uniform distributed loads on the inner and outer radii as shown in Figure 2.4; Highlights of this analysis are shown below. The second solution is for a biaxially loaded notched plate; the details of this analysis are presented by Russell, [15]. The following form of the displacement field is assumed,

$$u_r = \sum_{j=0}^{N} \sum_{k=1}^{M} q_j^k \, r^{2(k-M)+1} \cos(2j\theta), \quad u_\theta = \sum_{j=0}^{N} \sum_{k=1}^{M} q_j^{M+k} \, r^{2(k-M)+1} \sin(2j\theta), \qquad (2.22)$$

where u_r and u_θ are the displacement components and q_j^k are unknown parameters. This displacement field satisfies symmetry conditions and, for the case of an isotropic circular ring loaded by internal and external pressure, it converges to the exact solution with very few terms of the series; j=0 and k=2. Substituting this equation into the principle of minimum potential energy, equation (11), leads to a system of M(2N+1) linear equations which are solved simultaneously for the unknown parameters, q_j^k.

2.3.3 Solution Procedure for Problems With One Plane of Symmetry

Problems with one plane of symmetry such as a curved beam loaded in pure bending are represented by Figure 2.3. The solution procedure starts with the assumed form of the displacement field;

$$u_r = \sum_{l=0}^{L} \sum_{n=1}^{N} \left[q_l^n \, f_n(r) + Q_l^1 \, r \ln r \right] \cos\left(\frac{\pi}{\phi} l\theta\right), \quad u_\theta = \sum_{l=0}^{L} \sum_{m=1}^{M} v_l^m \, g_m(r) \, Z(\theta), \qquad (2.23)$$

where u_r and u_θ are the displacement components and q_l^n, v_l^m, and Q_l^1 are the unknown parameters. The functions $f_n(r)$, $g_m(r)$ and $Z(\theta)$ are defined as

$$f_n(r) = r^{2(n-N)+1}, \; g_m(r) = r^{2(m-M)+1}, \text{ and } Z(\theta) = \begin{cases} \theta & \text{if } l = 0 \\ \sin\left(\frac{\pi}{\phi} l\theta\right) & \text{if } l > 0 \end{cases}. \qquad (2.24)$$

These functions were chosen so that when L=0, N=2, and M=1, and the beam has isotropic material properties, the displacements take the correct form as shown below which is found from the closed form elasticity analysis described in the previous section;

$$u_r = q_1 \frac{1}{r} + q_2 r + q_3 r \ln r \quad , \quad u_\theta = q_4 r \theta \, . \tag{2.25}$$

The beam theory assumption that plane sections remain plane can always be maintained if the input variables are set so that M = 1 and L = 0. Adding more terms allows the evaluation of beams which might not follow the beam theory assumption such as in the case of beams with heterogeneous material properties. The displacements can be written in matrix form;

$$\{u\} = \begin{Bmatrix} u_r \\ u_\theta \end{Bmatrix} = \sum_{l=0}^{L} [U_l] \{q_l\} \, , \tag{2.26}$$

where $\{q_l\}$ is a vector containing N+M+1 unknown parameters and $[U_l]$ is a 2 x (N+M+1) matrix of the form;

$$[U_j] = \begin{bmatrix} f_1 \, C \, \ldots \, f_n \, C & r \ln r \, C & 0 \quad \ldots \quad 0 \\ 0 \quad \ldots \quad 0 & 0 & g_1 \, Z \, \ldots \, g_m \, Z \end{bmatrix} , \tag{2.27}$$

$$\{q_l\} = \begin{bmatrix} q_1^1 \, \ldots \, q^N & Q_1^1 & v_1^1 \, \ldots \, v_1^M \end{bmatrix}^T \, , \tag{2.28}$$

and $C = \cos\left(\frac{\pi}{\phi} 1\theta\right)$. Applying the strain-displacement relations, equation (2.15), we find;

$$\{\varepsilon\} = \begin{Bmatrix} \varepsilon_r \\ \varepsilon_\theta \\ \gamma_{r\theta} \end{Bmatrix} = \sum_{l=0}^{L} [H_l] \{q_l\} \, , \tag{2.29}$$

where

$$[H_l] = \begin{bmatrix} \left(f'_1 \ldots f'_N\right) C & (1+\ln r) \, C & (0 \ldots 0) \\ \left(f_1 \ldots f_N\right) C/r & \ln r \; C & \left(g_1 \ldots g_M\right) \dot{Z}/r \\ \left(f_1 \ldots f_N\right) \dot{C}/r & \ln r \; \dot{C} & \left[\left(rg'_1 - g_1\right) \ldots \left(rg'_M - g_M\right)\right] Z/r \end{bmatrix} . \tag{2.30}$$

The stress resultant vector is found by applying the stress-strain relations as given in equation (2.18);

$$\{N\} = [A]\{\varepsilon\} = \sum_{l=0}^{L} [A][H_l]\{q_l\} \ . \tag{2.31}$$

The global stiffness matrix is found by substituting equations (2.26), (2.29), and (2.31) into the expression derived from the principle of Minimum Potential Energy, equation (2.11);

$$[K_{jl}] = \sum_{j=0}^{L}\sum_{l=0}^{L} \int_{0}^{\Phi} \int_{ri}^{ro} [H_j]^T [A] [H_l] \, r \, dr \, d\theta. \tag{2.32}$$

For all values of j and l, each $[K_{jl}]$ is an (N+M+1) by (N+M+1) matrix since $[H_j]^T$ is a (N+M+1) by (3) matrix, [A] is a (3) by (3) matrix and $[H_l]$ is a (3) by (N+M+1) matrix. $[K_{jl}]$ is partitioned in to nine sections which have the dimensions as shown below.

$$[K_{jl}] = \begin{bmatrix} [\,N \times N\,] & [\,N \times 1\,] & [\,N \times M\,] \\ [\,1 \times N\,] & [\,1 \times 1\,] & [\,1 \times M\,] \\ [\,M \times N\,] & [\,M \times 1\,] & [\,M \times M\,] \end{bmatrix}_{jl} \tag{2.33}$$

Each of the nine sections are defined by a single expression. The radial integrals found in equation (2.32) are simple functions and exact solutions are found. The tangential integrations can be quite complex and are solved numerically using Simpson's Rule.

2.4 Results

The superposition model, which is used to find stresses and displacements in a curved beam loaded in pure bending, has been verified by comparing results with mechanics of materials and finite element analysis solutions. Several example problems of isotropic beams having I-, T-, or rectangular cross-sections have been examined and the difference between the superposition and mechanics of materials solutions is less than 1% for all cases. Two-dimensional finite element analysis is used to compare results for a curved heterogeneous anisotropic J-beam. The heterogeneity is introduced into the finite element analysis by varying the material properties in each element of the model. Table 2.1 compares the superposition results with those found using finite element analysis for a beam with the following dimensions: inside radius is 95.0 cm, the outside radius is 101.3 cm, the lower flange is 1.24 cm wide, the upper flange is 2.26 cm wide and the web and flanges are 0.15 cm thick. The flanges are incorporated into the finite element model by setting the thickness of the inside and outside row of elements accordingly. Three different constitutive relations are examined; the degree of radial heterogeneity, n, is set equal to -2, 0, and +2, where an 'n' value of -2 corresponds to a beam which is approximately 20% stiffer on the inside radius, an 'n' value of +2 is roughly equivalent to a beam which is 20% stiffer on the outside radius, and an 'n' value of zero means the beam is homogeneous. The finite element analysis results are within 3.4% of the superposition results as shown in Table 2.1.

Table 2.1

Comparison of Superposition and Finite Element Analysis Results
for a Heterogeneous, Anisotropic J-Beam Loaded in Pure Bending

Solution Procedure	Degree of Heterogeneity (n)	Maximum Displacement. (cm)	Maximum Stress (kPa)	Minimum Stress (kPa)
FEA	-2	1.798 E-4	35.44	-24.13
Superposition	-2	1.831 E-4	35.65	-24.41
% Difference	---	1.8 %	0.6 %	1.1 %
FEA	0	1.659 E-4	34.54	-24.61
Superposition	0	1.717 E-4	34.75	-25.03
% Difference	---	3.4 %	0.6 %	1.7 %
FEA	2	1.582 E-4	33.72	-25.30
Superposition	2	1.610 E-4	33.85	-25.58
% Difference	---	1.7 %	0.4 %	1.1 %

The validity of the model has been demonstrated and the effect of radial heterogeneity on beam performance can now be determined. The maximum tangential stress and maximum displacement versus heterogeneity are found for a curved J-beam loaded in pure bending. These maximum values are plotted for several different beam geometries in Figure 2.6. The degree of heterogeneity is varied from -2 to +2 corresponding to approximately a 20% decrease or 20% increase in stiffness, respectively. The effect of material heterogeneity is highly dependent on the beam geometry which is characterized by the average radius to depth ratio, R/t; where $R = (r_i + r_o)/2$ and $t = r_o - r_i$. Heterogeneity has a considerable effect on the maximum tangential stress in beams with a small curvature, R/t = 1, while it has virtually no effect on the stresses in beams with a large curvature. The maximum displacement is affected by heterogeneity for all beam geometries considered, but, the effect is again seen more drastically in beams with small curvature.

This analysis procedure can be used as a simple tool for preliminary design of curved beams. Given the basic beam dimensions, i.e., inner and outer radii, a range of values for all other dimensions can be selected. Flange widths and thicknesses can be varied independently as well as the material properties and degree of heterogeneity in each section. The results of a sample preliminary design are presented in Table 2.2. Two types of beams are analyzed; a J-beam with an R/t ratio of 14.5 and a channel beam with an R/t ratio of 6.7. The table shows the change in maximum and minimum tangential stress as well as the maximum deflection for a range of several variables. These variables are the degree of radial heterogeneity which is varied from -2 to +2 for isotropic and unidirectional beams, the inner flange thickness, h_1, which is varied from 0.23 to 2.26 cm, and the web thickness, h_2, which is varied from 0.10 to 0.25 cm.

Table 2.2

Design Study Results

Beam Type	Material	Variable Parameter	% Change in Max. Stress	% Change in Min. Stress	% Change in Max. Deflection
J-Beam	Uni-Directional	n = -2 to +2	6.7	6.1	12.8
J-Beam	Isotropic	n = -2 to +2	6.7	6.1	12.8
J-Beam	Uni-Directional	h1 =.23 to 2.26	49.7	20.1	37.4
J-Beam	Uni-Directional	h2 = .10 to .25	33.9	26.7	31.1
C-Beam	Uni-Directional	n = -2 to +2	16.5	14.3	28.4
C-Beam	Isotropic	n = -2 to +2	16.3	14.0	28.2
C-Beam	Uni-Directional	h1 =.38 to 1.14	26.2	10.1	18.7
C-Beam	Isotropic	h1 =.38 to 1.14	26.1	10.2	19.6

The Rayleigh-Ritz technique is used to solve the problem of a curved beam loaded by internal and external pressure. Solutions are compared with exact results for isotropic and axisymmetric anisotropic beams [13], and the difference is within 0.1%. This solution technique is also verified by solving the problem of an infinite plate with a centrally located hole loaded only by an internal pressure where the principle material directions are along the Cartesian axes. This problem is modeled by letting r_i = 2.54 cm, r_o = 76.2 cm, P_i = 1 Pa, and P_o = 0 Pa The stress concentrations found at $\theta = 0°$ and 90° are within 1% of those found by Lekhnitskii, [13]. A carbon reinforced thermoplastic composite ring with an inner radius of 15.24 cm and an outer radius of 20.3 cm is analyzed for two different fiber arrangements; one with tangentially oriented fibers and the second with fibers aligned in the x-direction. The stress distribution is axisymmetric in the ring with tangentially oriented fibers as shown in Figure 2.7a while the ring with straight fibers in the x-direction has a slight stress concentration at approximately $\theta = 45°$ as shown in Figure 2.7b. These results are evidence that the tangential heterogeneity due to non-axisymmetric fiber distribution can effect the stresses in a curved beam loaded by internal and external pressure.

The Rayleigh-Ritz technique is also used to solve the problem of a curved beam loaded in pure bending. Results for isotropic beams compare to within 1% of the elasticity solutions. Results for anisotropic beams with the principle fiber directions along the polar axes also compare to within 1%. The results for beams having heterogeneous material properties are currently being compared to finite element analysis solutions.

2.5 Concluding Remarks

A closed form elasticity solution can be used to solve for the stresses and displacements in a heterogeneous anisotropic curved beam loaded in pure bending. The elasticity analysis, based on the superposition of several two-dimensional solutions, provides results which are in very good agreement with those found from mechanics of materials and finite element analysis. The heterogeneity is introduced into the model by defining the material properties as an exponential function of the radius, while the actual heterogeneity due to fiber realignment during forming can be determined using enhanced ultrasonic C-scanning techniques.

The effect of radial heterogeneity on curved beams loaded in pure bending depends on the geometry of the beam. The maximum stress and deflection in beams with a small average radius to depth ratio is significantly effected by heterogeneous material properties. A beam whose stiffness

decreases by 20% from the inside to outside radius (i.e., n = -2), shows a 28% increase in the maximum tangential stress and a 75% increase in the maximum deflection when compared to a homogeneous beam if R/t = 2, but only a 1% and 4% increase, respectively, if R/t = 10. It is unlikely that radial heterogeneity effects the performance of most beams used in transport aircraft fuselage applications since they have an R/t > 10; but this heterogeneity could play a part in the performance of beams used in other applications.

The superposition elasticity analysis has been incorporated into a computer program which can be used for design studies of curved beams. Several of the beam parameters can be varied to determine their overall effect on maximum tensile and compressive stresses, as well as maximum deflections. The variable parameters are the thickness and depth of the flange and web along with their material properties and degree of radial heterogeneity. This provides a quick and easy way to perform initial beam sizing calculations.

The Rayleigh-Ritz analysis can be used to solve problems with both radial and tangential heterogeneity. The importance of this ability is demonstrated by the results of the pressurized ring problem. Isotropic and axisymmetric anisotropic rings have an axisymmetric state of stress when pressurized. Rings with tangential heterogeneity however, do not have an axisymmetric state of stress when pressurized. Stress concentrations develop which are a function of both the material properties and the heterogeneity. This type of analysis is currently being used to study the effect of heterogeneity on curved beams subject to several different loading conditions; pure bending, internal and external pressure, and end loading. Geometric heterogeneity, such as a notch or cut-out, is also under investigation. Future work includes applying an appropriate failure criterion to the results of these analyses and comparing with experimental data.

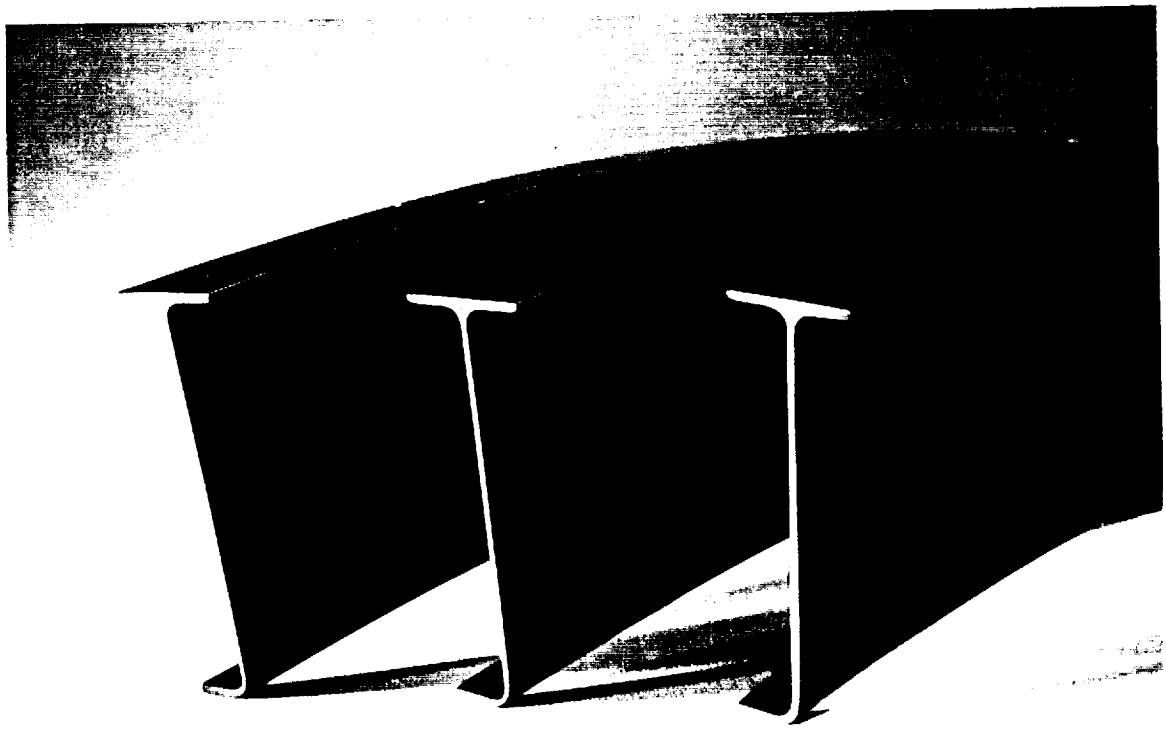

Figure 2.1: Thermoplastic Composite Curved Beam

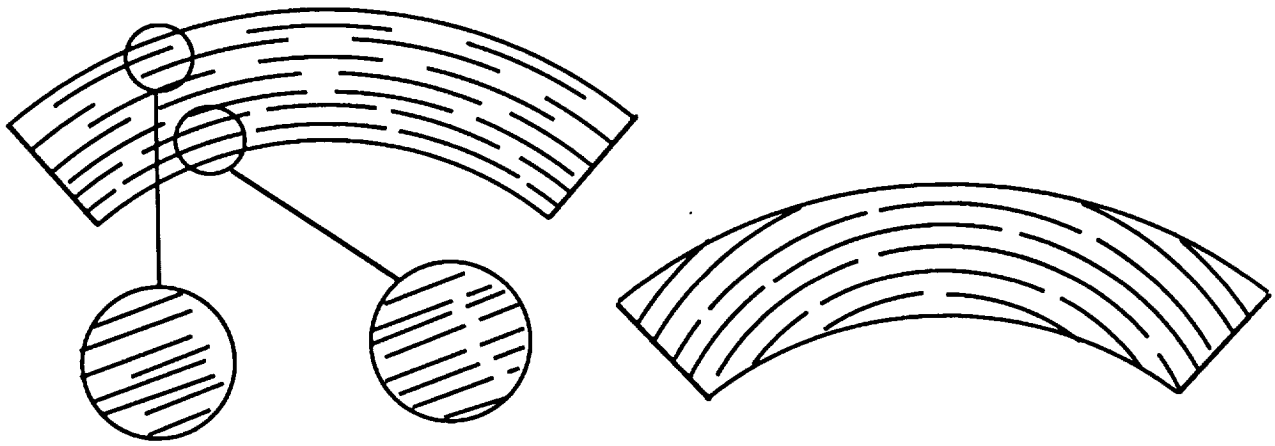

Figure 2.2: Different Types of Material Heterogeneity

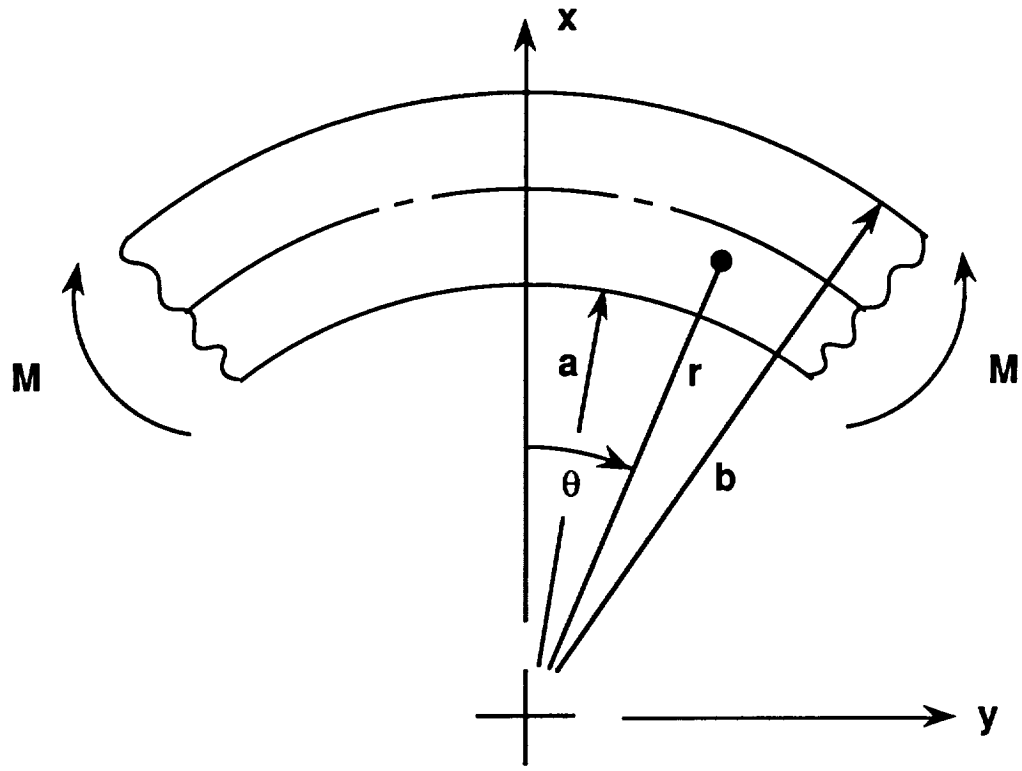

Figure 2.3. Pure Bending Load Case

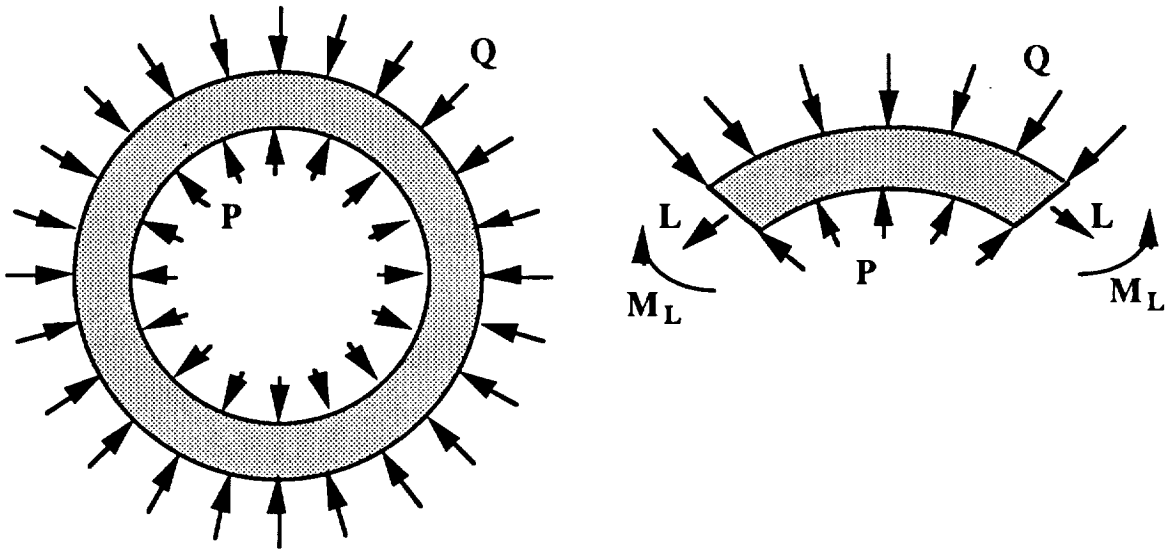

Figure 2.4. Lame's Problem

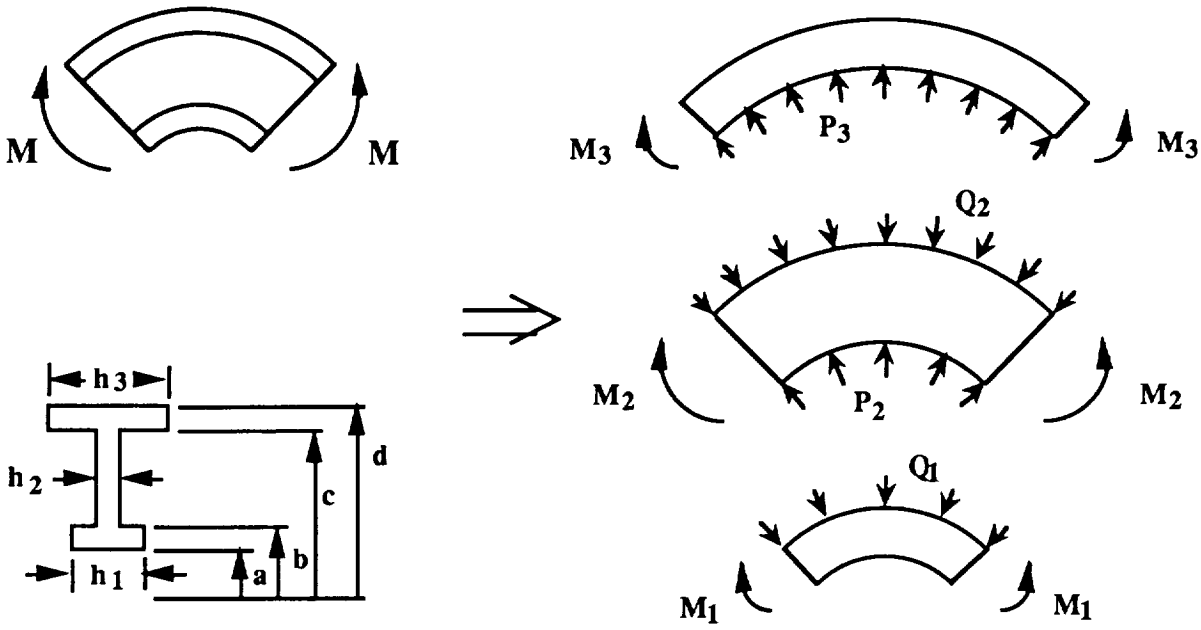

Figure 2.5. Superposition Analysis

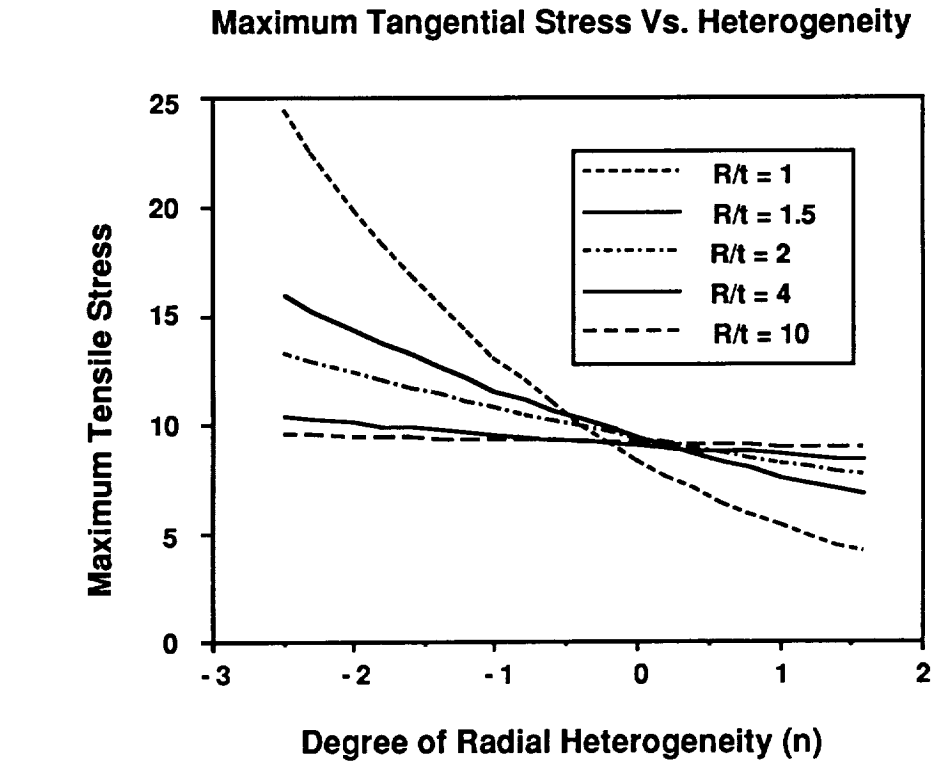

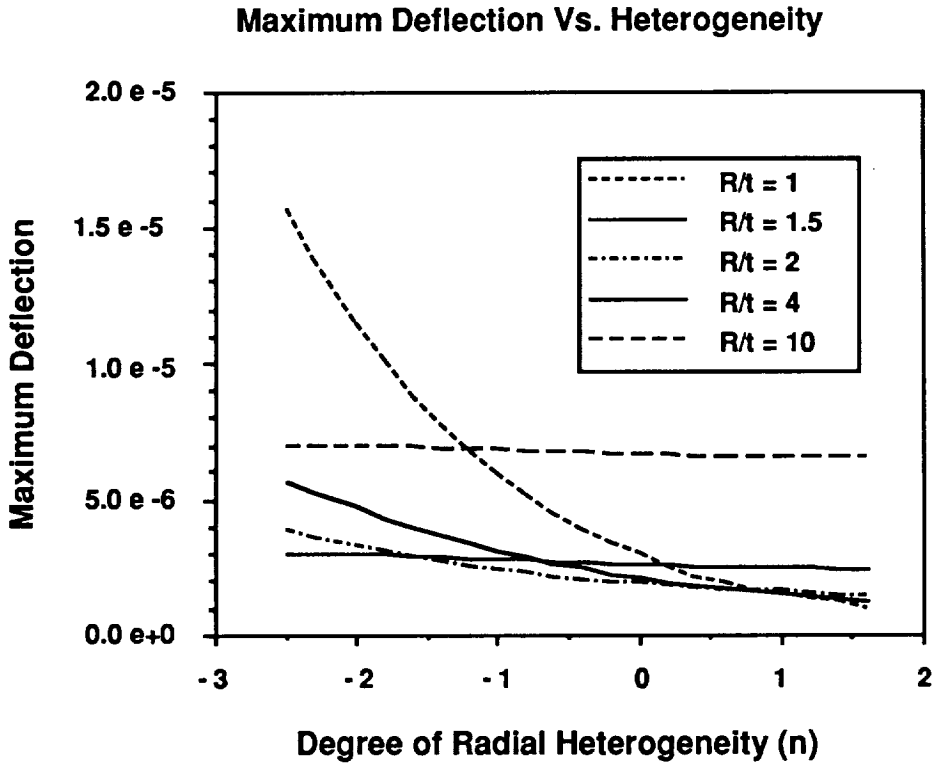

Figure 2.6: Maximum Tangential Stress and Maximum Displacement vs. Heterogeneity

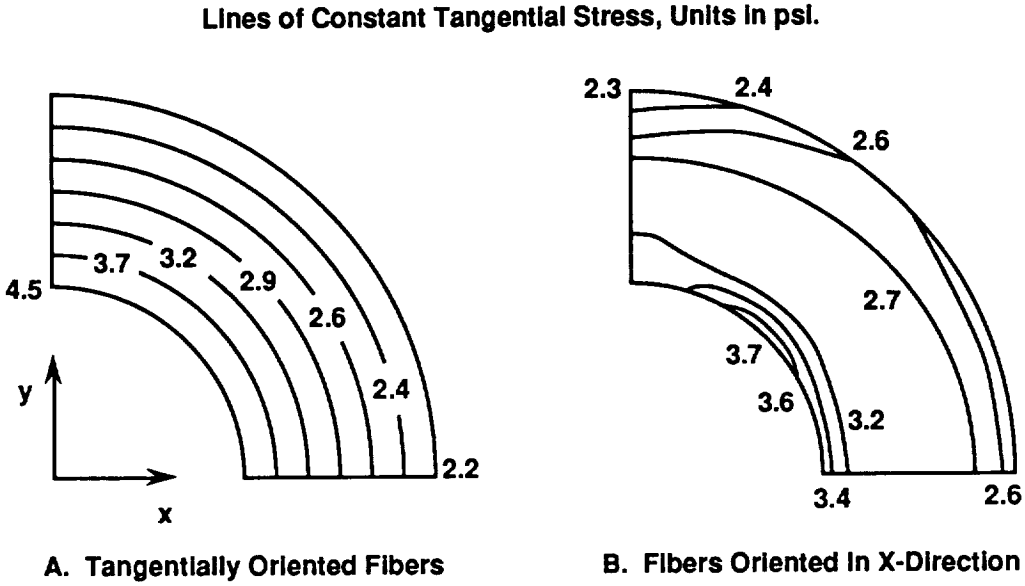

Figure 2.7. Tangential Stress Contours in a Circular Ring Loaded by an Internal Pressure, P_i = 1 Pa.

3.0 Structural Testing of Curved Composite Beams Made of Long Discontinuous Fiber Thermoplastic Composite

3.1 Introduction

An experimental investigation is conducted to determine the failure mechanisms of the curved J-beams described in the appendix. There are no ASTM standard experimental procedures for testing curved beams but some trends are found in the literature review [16-21]. Rich and Lowry [16] test curved I-beams in a fixture which imparts a combined axial load and bending moment. Llorente, et al., use similar loading conditions to test curved channel sections [20]. Typical design loads for an aircraft fuselage structure are presented in Figure 3.1. Loading conditions for three different design constraints are approximated with a combination of an applied axial load, bending moment, and shear load [22].

A fixture was designed and developed for testing the LDF^{TM} J-beams used in this study. Two different gage lengths were tested under loading conditions similar to the '3.75G' design constraint shown in Figure 3.1, where the bending moment is four times the axial load. Failure mechanisms are discussed and load versus strain data is compared to theoretical predictions.

3.2 Experimental Procedure

The outer arc length of each beam is 40.64 cm and the inner arc length is 38.1 cm with a web depth of 6.50 cm. The end of one of the beams was damaged during test preparation and the damaged section was removed. The outer and inner arc lengths of this shortened beam are 30.48 cm and 28.58 cm, respectively. This beam is referred to as the 'short beam' for the remainder of this discussion.

Load is transferred to the beams through a clevis with a 1.27 cm pin. End tabs are attached to both ends of each beam to help distribute the load more evenly. This reduces the chance of beam failure in the highly stressed area near the load pin. Two end tab designs are used for these experiments. The first end tab design uses a 5.1 x 6.4 cm rectangular block of aluminum on each side of the web. The tabs are 0.95 cm thick and bonded to the composite using HYSOL's EA9309NA epoxy. A 1.27 cm bolt hole is drilled and reamed through the end tabs and the composite 2.54 cm from end of the beam. This provides a 25.4 cm distance between loading points in the 'short beam'.

The second set of end tabs is designed to impart a greater bending moment to the beam by using an offset tensile load. These tabs are machined from T6061 aluminum and are also bonded to the composite beam with epoxy. These tabs are also bolted to the beam with four 5 mm bolts positioned as shown in Figure 3.2. The tabs extend radially from the beam and three 1.27 cm holes are drilled and reamed to provide a choice of moment arms. A clevis is used to apply a pin loading at either 7.6, 10.2, or 12.7 cm from the center line of the beam.

Rich and Lowry [16] found that supports were needed to prevent out-of-plane deflections in the curved I-beams which they tested. They reasoned that the fuselage skin provides a similar form of stability to the curved beams used as skin stiffeners in aircraft structures. A restraining frame, was constructed and used to reduce the out-of-plane deformation in the J-beams tested during this investigation. The frame consists of aluminum angle sections with steel cross members. Adjustable aluminum spacers are attached to the steel cross members and tightened until they just made contact with the beam. These spacers are 2.5 x 5.1 x 1.3 cm blocks located at

different positions along the beam length depending on the end tab arrangement. Figure 3.3 shows three different configurations used for the tests.

The parts are loaded in tension using an 1125 Instron with a 88.9 kN load cell. The load is applied at a constant velocity of 1.27 mm/min. The strain is measured with gages at eight locations across the depth of the beam half-way between the end tabs as pictured in Figure 3.4. Two gages are placed in the center of the outer flange on the outside surface. One gage is oriented tangentially and the other gage is oriented in the transverse direction. Two gages are placed on the inner flange and oriented in the same manner as the outside flange. The last two sets of gages are positioned on the web 6.4 mm from the flanges. Each of these sets has one gage oriented radially and the other is oriented tangentially.

3.2.1 Initial Tests

The first test was conducted with the 'short beam' and the smaller end tabs which were loaded through the center of the web. This configuration is shown schematically in Figure 3.3a. This was one of the 'J2' beams and its' mechanical properties are defined in the appendix. The test was started and initially there was no apparent deformation or accoustic emissions. A loud pop was heard when the load reached 9.78 kN and another very loud cracking sound occurred at 12.45 kN. The end tabs popped off at this point, the test was stopped, and the specimen was unloaded.

No damage was visible in the beam and the tabs on the bottom end were still intact. A visual inspection of the top end of the beam showed that none of the epoxy was left on the composite. Suspecting a poor batch of epoxy, the beam surface was resanded and degreased and then the end tabs were rebonded.

The test was repeated and no loud sounds were heard until the load reached 34.8 kN. The top end tabs had failed again and some tear out occurred at the bolt holes. There was no apparent damage to the composite and no epoxy remained on the beam; but, a 22.2 kN increase in load had been obtained.

This procedure was repeated one more time and the epoxy failed before the composite again. Slight clicking noises were hear occasionally until the load reached 30.2 kN at which time a loud bang was heard. Another even louder bang occurred at 32.0 kN which corresponded to the epoxy failure.

3.2.2 Additional Tests

This second set of end tabs were designed to increase the moment in the test section of the composite for a given applied load. These tabs can be attached to the beam two ways; the first imparts a relative compressive load on the inside edge of the beam when loaded in tension as shown in Figure 3.3b and the second imparts a relative compressive load on the outer edge of the beam as shown in Figure 3.3c. The same 'short beam' was next tested in the configuration which applies relative compression to the inside edge. The load was applied with the same Instron and 88.9 kN load cell and at the same rate 1.3 mm/min. The beam tried to deform out-of-plane but the restraining fixture held it in place. The beam failed at an end load of 9.33 kN and an approximate end moment of 949 J. The failure occurred on the inner flange, next to the end tab about 3.8 cm from the end of the beam. Delamination was seen along the inner flange at this point, see Figure 3.5, so the crosshead was stopped and the beam was unloaded. A second failure occurred approximately 5 seconds after the initial failure while the beam was being unloaded. This failure started in the inner flange about 10.8 cm from the end of the beam and propagated halfway through the web. The beam appeared to twist out-of-plane as this failure occurred.

The same test configuration was used next to test one of the long 'J2' beams. Low level popping noises started to occur at about 4.6 kN and continued sporadically until a loud pop was heard at 9.7 kN. The load was still increased until another loud cracking sound was heard and the beam delaminated along the inner flange next to the top end tab. This occurred at an end load of 10.0 kN and an approximate end moment of 1.02 kJ. The delamination did not propagate past the end tab. A second failure occurred 7.6 cm below the first failure while the beam was being unloaded. This failure occurred at an end load 7.3 kN and appeared to be a torsion failure. These failure mechanisms are similar to the short beam failure modes shown in Figure 3.5. The load versus strain curves for the inner flange of both the long and short beams are shown in Figure 3.6. The outer flange load-strain curves are shown in Figure 3.7.

One of the 'J' beams was tested in the configuration which applies a relative compressive load to the outer flange as shown in Figure 3.3. This long beam was tested and slight pops could be heard after the load reached about 1.8 kN. The beam started to straighten at about 4.0 kN, the frequency of the popping noises increased at about 7.6 kN, and it failed at an end load of 10.2 kN. This failure started at one of the 5 mm bolt holes in the upper end tab and propagated across the web at a 45° angle. Another crack propagated out of this same bolt hole into the inner flange as shown in Figure 3.8. The damaged end of this beam was cut off so that the remaining piece had the 'short beam' dimensions. This beam was tested in the same configuration and failed in almost the same manner. Cracking sounds started to occur at 8.1 kN and the beam failed with a loud crack at an end load of 12.2 kN and an end moment of 48.9 kN. The failure mode was identical to that of the long beam. The load-strain curves for these beams are shown in Figure 3.9.

3.3 Theoretical Predictions

The test sections of the beams loaded in configurations 2b and 2c are modeled using finite element analysis. The loading conditions used are a combination of axial tension and pure bending. The end tabs used in the experiments provide a 10.2 cm moment arm; therefore, the boundary conditions applied to the model are a unit end load, P, and an end moment, M = 4P. Configuration 2b is modeled with a negative moment which applied a relative compression on the inner edge and configuration 2c is modeled with a positive end moment. Symmetry conditions at the center line are used in the finite element analysis. The flanges are approximated by assigning the actual beam dimensions to the inner and outer rows of elements. The inner row of elements have a thickness of 1.24 cm, the outer row of elements have a thickness of 2.26 cm, and the web elements have a thickness of 1.52 mm.

The finite element analysis results are obtained for a beam with the elastic moduli of the J2 laminates described in the appendix. The tangential stresses on the inner and outer flanges along the center line of the beam are recorded. This corresponds to the location of the inner and outer sets of strain gages. The tangential stress on the inner flange of the short beam loaded in bending is $(\sigma_\theta)_{IF} = -5.3M$, where M is the magnitude of the applied bending moment. The tangential stress on the outer flange is $(\sigma_\theta)_{0F} = 5.0M$. The corresponding stresses for the same beam under an applied axial load are: $(\sigma_\theta)_{IF} = 6.0P$, where P is the applied axial load and $(\sigma_\theta)_{0F} = 2.1P$. Therefore, the tangential stresses in the short beam under the combined loading case, where M = 4P, are $(\sigma_\theta)_{0F} = 22.1P$ and $(\sigma_\theta)_{IF} = -15.2P$.

The experimental values for the tangential stress in the two flanges are obtained using the constitutive relation.

$$\sigma_{11} = A_{11}\varepsilon_1 + A_{12}\varepsilon_2, \qquad (3.1)$$

where the subscript, 1, corresponds to the tangential direction, the subscript, 2, corresponds to the transverse direction, the strains ε_1 and ε_2 are taken from the gage data and the laminate stiffness properties, A_{11} and A_{12} are calculated from laminate data given in the appendix. The experimental and theoretical stress versus load curves for the J2 short beam are shown in Figure 3.10.

The predicted stress values on the inner flange are very close to the experimentally determined values up until a load of about 4.9 kN. The slope of the experimental curve changes at this point, possibly due to the flange bending out of plane. The predicted stress values in the outer flange are consistently about 22% higher than the experimental values. Both of these curves stay linear throughout the entire test but with different slopes.

3.4 Discussion

The 'J2' beams were tested in configuration 2b, which imparts a relative compression on the inner flange. These beams were identical except for their length and the longer beam failed at a slightly higher load. They both failed in a two-step manner. The inner flange which was loaded in compression started to bend out of plane. This flange opening increased the interlaminar tensile stresses through the thickness of the flange-web bend. The inner flange delaminated at a point adjacent to the end tab in both beams. The second step of the failure process occurred while the beam was being unloaded. Both beams seemed to twist out of plane after the initial failure causing a large crack to propagate suddenly from the inner flange.

It seems that a compressive stress concentration exists on the inner flange near the end tab. This could be due to an uneven transfer of load to the beam through the end tab. Further modification is needed to avoid this type of failure in the future. The tab is only attached to the web of the beam in the present configurations. A new tab which fits the dimensions of the beam more closely and can be bonded to the flanges as well as the web might help to distribute the load more evenly. Another test could be conducted with a set of strain gages at the location of initial failure to determine the extent of the stress concentration. A more detailed finite element analysis of this region could also be used to determine the stress concentration.

The long and short beams tested in configuration 2c which applies a relative compression to the outer flange. These beams have the 'J' laminate mechanical properties and they both failed in the same manner. A tensile failure occurred starting from one of the small bolt holes used to secure the end tabs. Further analysis and design of the load transfer mechanism is needed so that beam failure occurs in the test section.

		Ultimate Pressure	3G Down Gust	3.75 G
M	in-lbs (J)	-20,070 (-2,268)	-5267 (-595.2)	12,000 (1356)
V	lbs (N)	0 0	117 (520.1)	0 0
P	lbs (kN)	48,998 (217.8)	0 0	-3000 (-13.34)

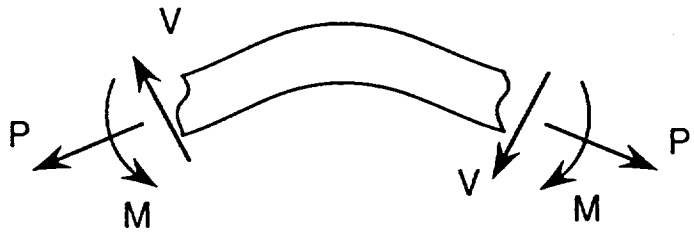

Figure 3.1 Typical Crown Frame Design Loads

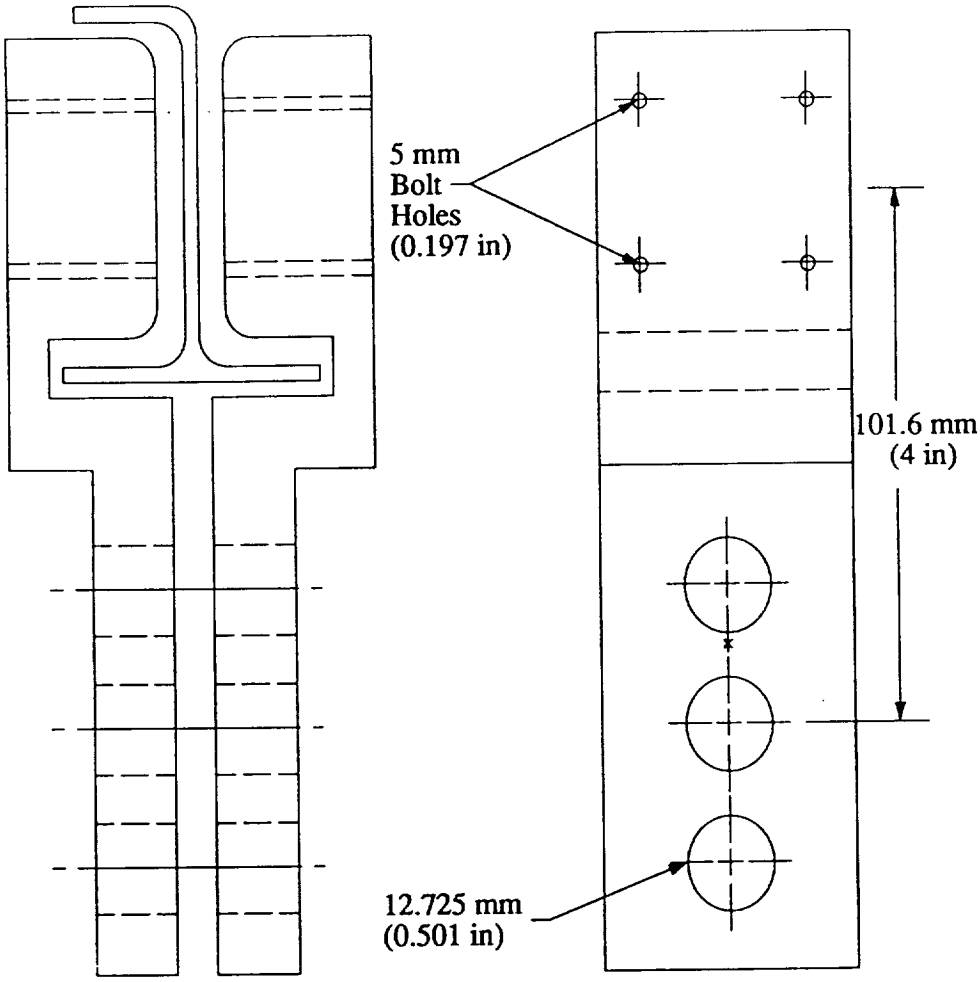

Figure 3.2 End Tab Configuration

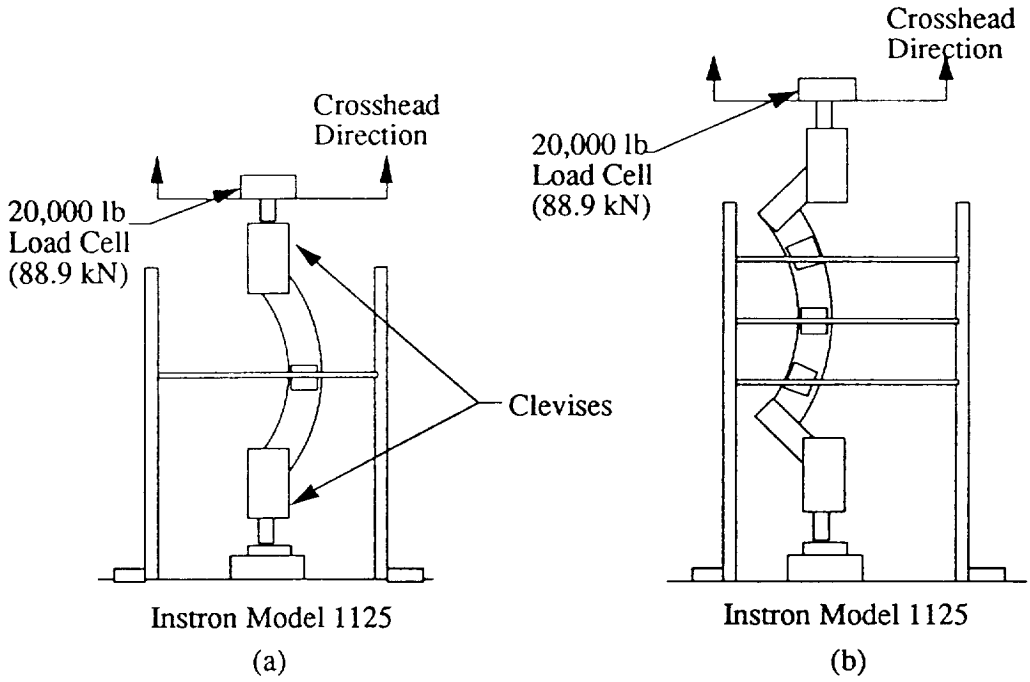

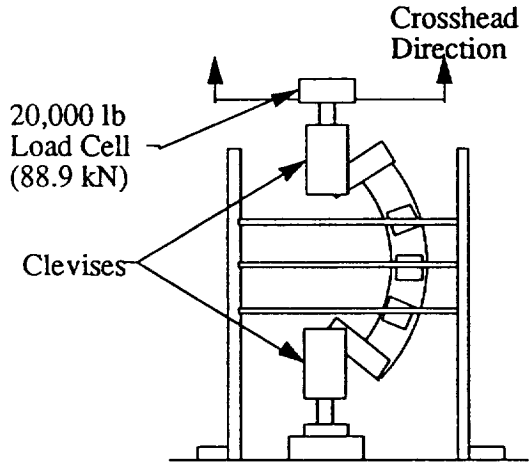

Figure 3.3 Test Configurations

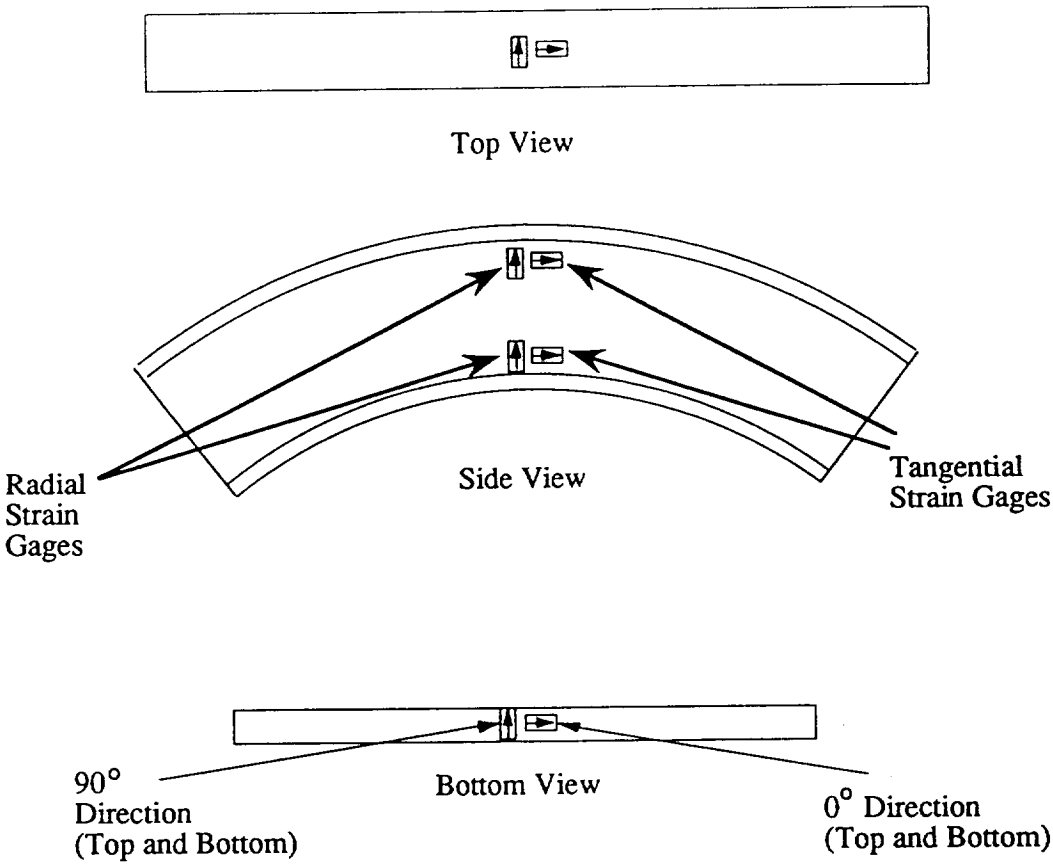

Figure 3.4 Strain Gage Locations

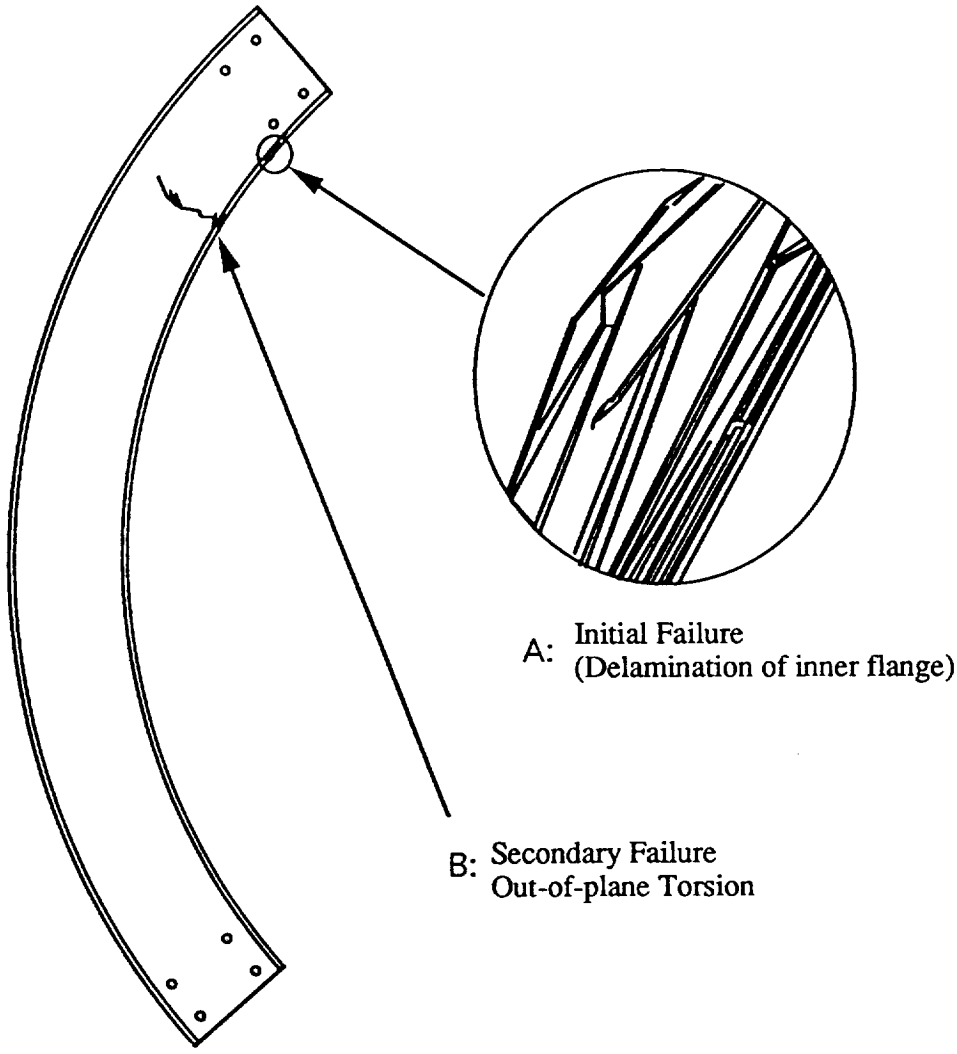

Figure 3.5 Failure Mechanisms of Beams Tested in Configuration 3b

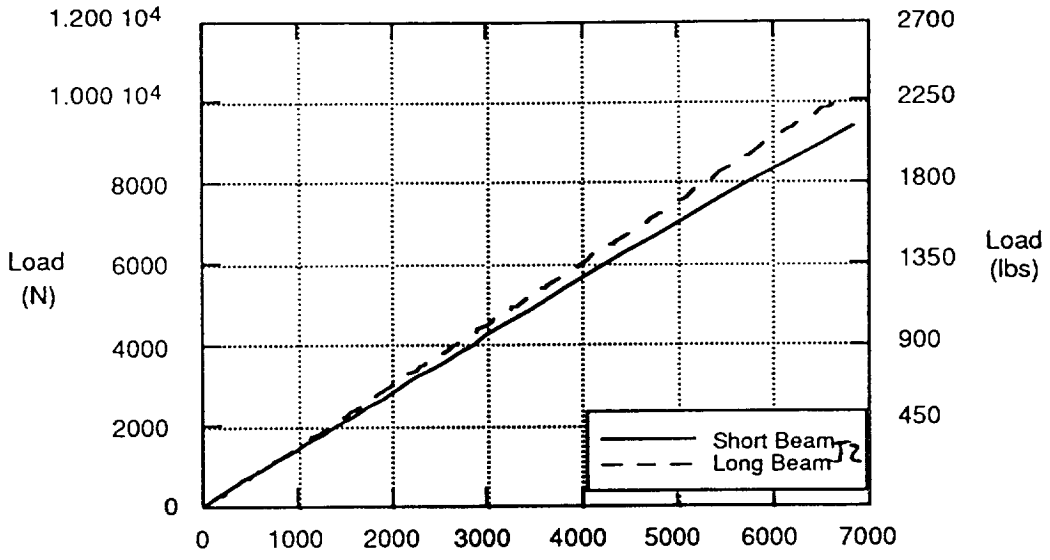

(a) Microstrain in Outer Flange - 0° Direction

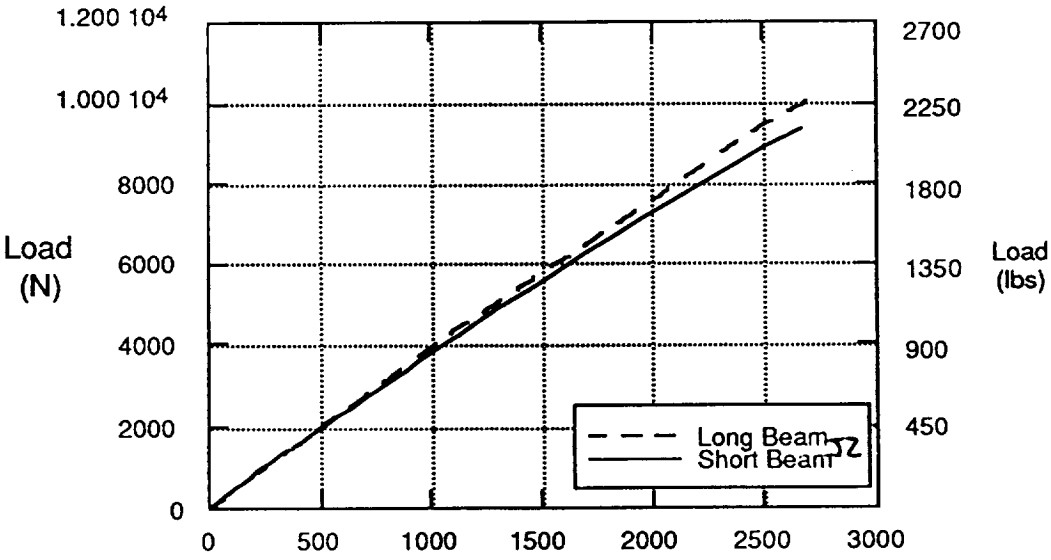

(b) Compressive Microstrain in Outer Flange - 90° Direction

Figure 3.6 Load-Strain Curves for The Outer Flange of The Beams Tested in Configuration 3b

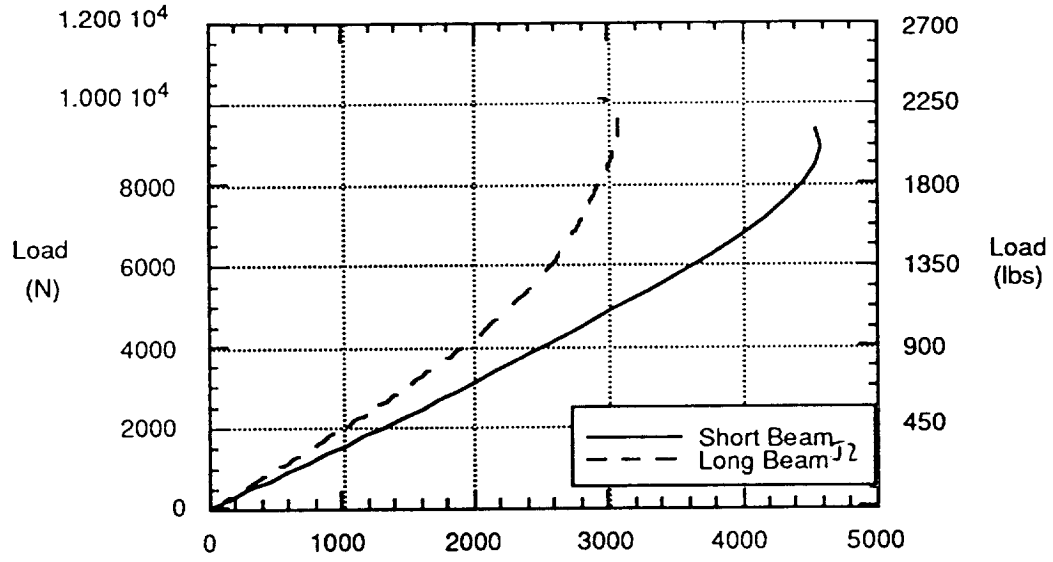

(a) Microstrain in Inner Flange - 0° Direction

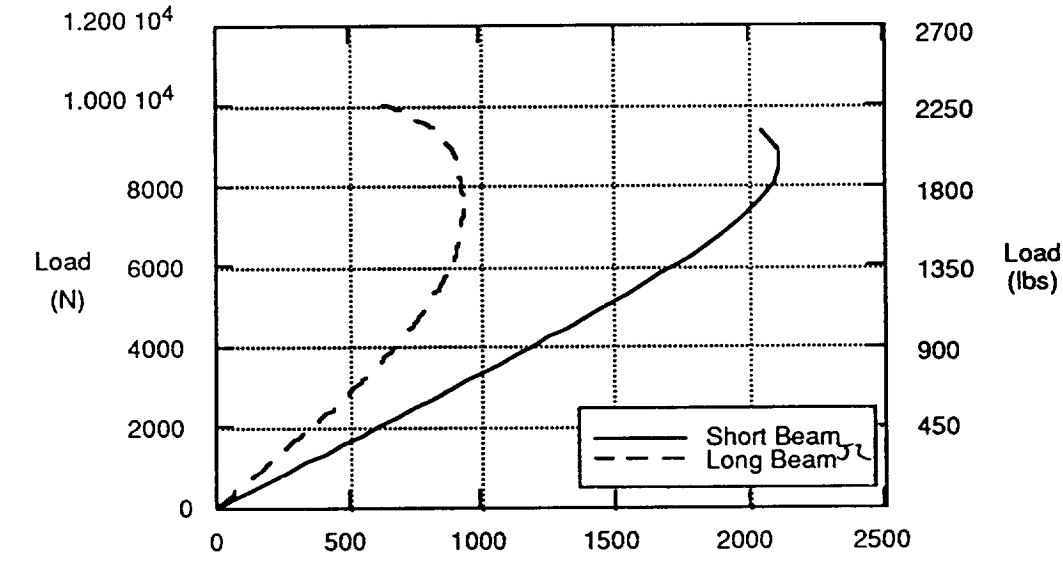

(b) Compressive Microstrain in Inner Flange - 90° Direction

Figure 3.7 Load-Strain Curves for The Inner Flange of The Beams Tested in Configuration 3b

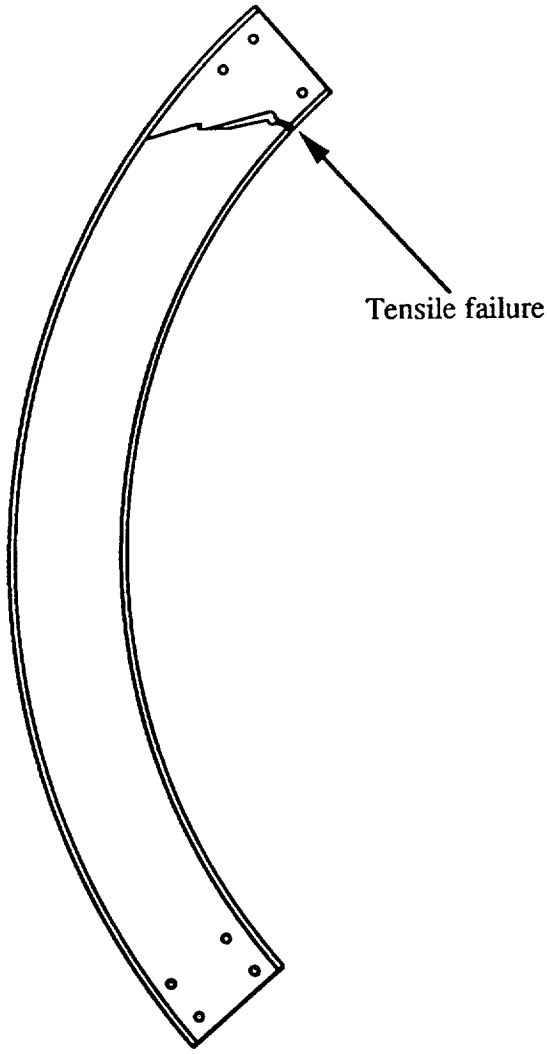

Figure 3.8 Failure Mechanisms of Beams Tested in Configuration 3c

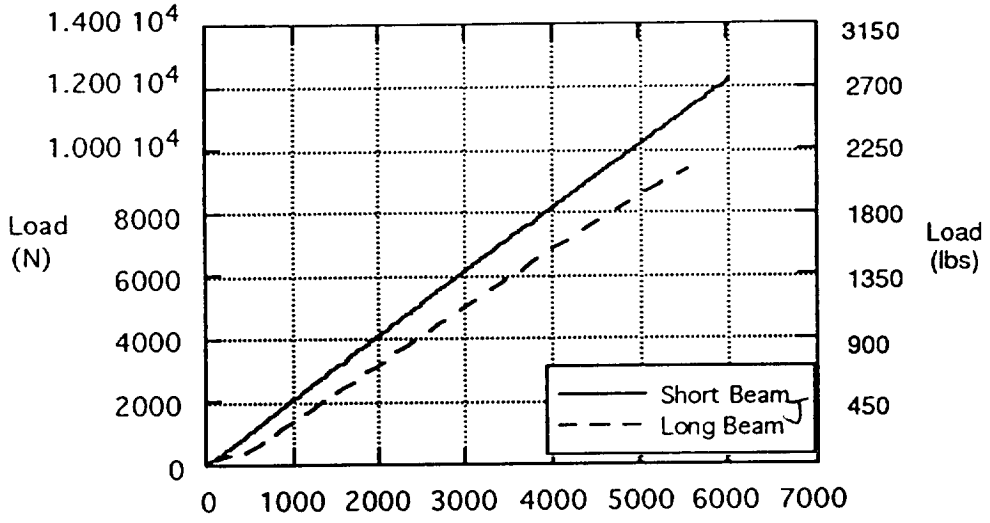

(a) Compressive Microstrain in Outer Flange - 0° Direction

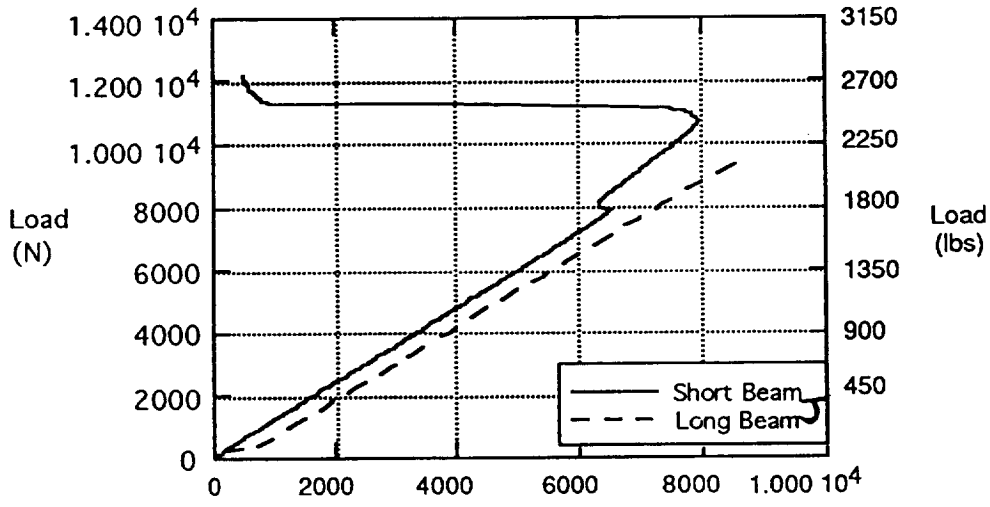

(b) Microstrain in Inner Flange - 0° Direction

Figure 3.9 Load-Strain Curves for Beams Tested in Configuration 3c

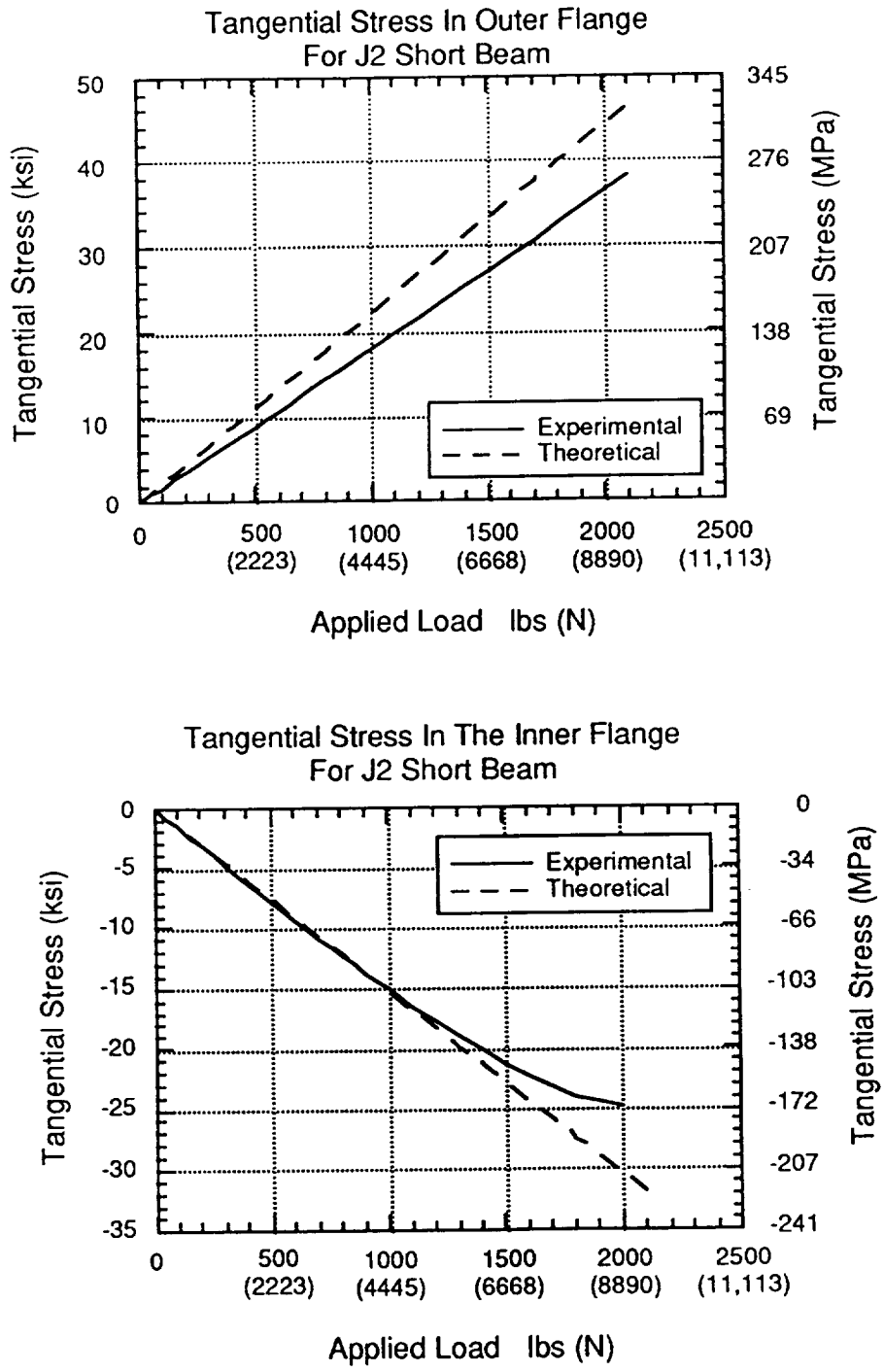

Figure 3.10 Experimental and Theoretical Stresss-Load Graphs for Short Beam With J2 Layup

Concluding Remarks

Flexible manufacturing methods are needed to reduce the cost of using advanced composites in primary commercial aircraft structure. One material system that allows for flexibility is long discontinuous fiber thermoplastic matrix composite. In order to exploit this flexibility in an economical way, a thorough understanding of the relationship between manufacturing and component performance must be developed. This report reviews some of the recent work geared toward establishing this understanding.

A Carreau fluid model is introduced into the previously developed micromechanics formulations. The effects of varying the Carreau parameters are demonstrated using the model. Additionally, the influence of fiber orientation distribution is investigated. Results show that a small misalignment in the fibers can reduce the elongational viscosity by several orders of magnitude without a large effect on the viscosity values.

By superimposing the closed form solutions for different regions of a curved beam structure one can create a useful design tool for studying various degrees of material heterogeneity and beam geometries. The results from these models show that the effects of material heterogeneity depend heavily on the geometry of the structure. A rectangular cross section curved beam whose stiffness decreases by 20% from the inside to outside radius shows a 28% increase in maximum stress over a homogeneous beam with a radius to depth ratio R/t = 2. However the decrease is about 1% for a similar beam whose R/t ratio is 10. Structures with a more general type of heterogeneity can be studied using a Rayleigh-Ritz analysis. This approach can be used to study the effects of material heterogeneity on stress concentrations near holes and notches as well as curved beam and other type structures.

Several tests were conducted on prototype beams to determine load deflection and failure characteristics. The major difficulty was devising a fixture that tests the beams in in-plane bending. The failure observed were believed to be a result of out-of-plane bending and twisting. Further work needs to be done to determine with confidence the probable behavior of these parts in actual aircraft structural configurations.

References

[1] R.B. Pipes, J.W.S. Hearle, R.K. Okine, A.J. Beaussart and A.M. Sastry,"A Constitutive Relation for the Viscous Flow of an Oriented Fiber Assembly," J. Comp. Mat., April 1991.

[2] R. B. Pipes, J. W. S. Hearle, A. J. Beaussart, and R. K. Okine, "Influence of Fiber Length on the Viscous Flow of an Oriented Fiber Assembly," J. Comp. Mat., July 1991.

[3] R. B. Pipes, "Anisotropic Viscosities of an Oriented Fiber Composite with a Power Law Matrix," J. Comp. Mat. (to appear)

[4] D. W. Coffin, R. B. Pipes, "Anisotropic viscosities of an Oriented Fiber Assembly," Proceedings of ICCM/8, Honolulu, Hawaii, July 15-19, 1991.

[5] P. J. Carreau, Trans. Soc. Rheol., 16 (1), 99, 1972.

[6] P. J. Carreau, D. DeKee, and M. Daroux, Can. J. Chem. Eng., 57, 135, 1979.

[7] Z. Kemblowski and M. Michniewicz, Rheol. Acta, 20, 352, 1981.

[8] J. F. Pratte et al., "High Performance Thermoplastic Composites with Poly(ether keytone keytone) Matrix," Proceedings of the 34th International SAMPE Symposium, Reno, 1989.

[9] C.M. O'Bradaigh, R.B. Pipes and P.J. Mallon., "Issues in Diaphragm Forming of Continuous Fiber Reinforced Thermoplastic Composites," Polymer Composites, Vol. 12, no. 4, 1991, pp 246-256.

[10] S. Medwin, "Long Discontinuous Ordered Fiber Structural Parts," 34th International SAMPE Symposium and Exhibition, Reno, NV, May 8-11, 1989.

[11] J.F. Pratte, W.H. Krueger, and I.Y. Chang, "High Performance Thermoplastic Composites With Poly Ether Ketone Ketone Matrix," 34th International SAMPE Symposium and Exhibition, Reno, NV, May 8-11, 1989.

[12] R.B. Pipes, M.H. Santare, B.J. O'Toole, A.J. Beaussart, D.C. DeHeer, and R.K. Okine, "Long Discontinuous Fiber Composite Structure - Forming and Structural Mechanics," Proceedings of the First NASA Advanced Composites Technology Conference, Seattle, Washington, Oct. 29-Nov. 1, 1990, pp 247-270.

[13] S.G. Lekhnitskii, Theory of Elasticity of an Anisotropic Body, Mir Publishers, 1981.

[14] T.R. Tauchert, Energy Methods in Structural Mechanics, McGraw-Hill, 1974, pp 72-76.

[15] S.G. Russell, "A Rayleigh-Ritz Analysis Methodology for Cutouts in Composite Structures," Proceedings of the First NASA Advanced Composites Technology Conference, Seattle, Washington, Oct. 29-Nov. 1, 1990, pp 901-920.

[16] M. J. Rich and D. W. Lowry, "Design, Analysis and Test of Composite Frames for Helicopter Fuselage Structures," AIAA Journal. 1983, pp 83-1005.

[17] K. T. Kedward, R. S. Wilson and S. K. McLean, "Flexure of Simply Curved Composite Shapes," Composites, November 1989, pp 527-536.

[18] G. E. Mabson and E. P. Neall III, "Analysis and Testing of Composite Aircraft Frames for Interlaminar Tension Failure," National Specialists Meeting on RotaryWing Test Technology of the American Helicopter Society, Bridgeport, CT. March 15-16, 1988.

[19] G. E. Mabson, "Effects of Curvature on Composite Material Beams," AIAA Journal, 1989, 89-1362-CP

[20] S. Llorente, P. Minguet, R. Fay and S. Medwin, "Application of Advanced Material Systems to Composite Frame Elements," Proceedings of the Ninth DoD/NASA/FAA Conference on Fibrous Composites in Structural Design, Lake Tahoe, NV, November 4-7, 1991.

[21] F. Chang and G. S. Springer, "The Strengths of Fiber Reinforced Composite Bends," Journal of Composite Materials, January 1986, pp 30-45.

[22] J. F. Pratte, "Curved Composite Beams for University of Delaware NASA-ACT Program," Program Status Report, U/D Sub-Contract, Du Pont Composites, E. I. du Pont de Nemours and Company, Inc., 1991.

APPENDIX

PROGRAM FINAL REPORT

FOR DUPONT SUB-CONTRACT

(report is included in its entirety with editing)

PROGRAM FINAL REPORT
November 1991

(Ref. Du Pont Proposal #06B-C90-050)

Curved Composite Beams for University of Delaware NASA-ACT Program

NASA Contract #NASA1-18758
U/D Sub-Contract #B-110803-6

Submitted by:

Du Pont Composites
E. I. du Pont de Nemours and Company, Inc.

J. F. Pratte (Project Manager)
Phone (302) 999-2033

November 27, 1991

Introduction:

The primary goal of NASA's ACT program is to develop an integrated composites technology base that will keep the U.S. airframe industry competitive through the next several decades. Most of the program effort at the airframers have focussed on structural design concepts that take advantage of potential low cost processing and assembly methods to achieve weight and cost goals. Fuselage of commercial transports represent an area of the airplane that is being redesigned in this manner where curved beam elements comprise a major portion of the substructure.

One of the design concepts being evaluated by Boeing Commercial Airplane Group (BCAG) for its ACT program is a hat stiffened fuselage design where the curved "J" frame (figure 1) bonds directly to the skin. BCAG is considering LDF™ Technology (Long Discontinuous Fiber) for these curved "J" frames using Du Pont's patented stretch forming process. The main concern of this design is where stringers extend through the cutouts in the "J" frame. Structural performance of these frames will be largely determined by how severe the stress concentration is in the region of the cutout. Thus, one of the objectives of the University of Delaware's ACT program is to develop process models, analytical techniques and test data that would aid in the development of weight efficient curved beam designs.

The goals of this firm fixed price sub-contract to Du Pont from the University of Delaware were :

(a) Demonstrate that a curved "J" beam element could be made using a potential low cost fabrication method (i.e. stretch forming)

(b) Produce flat laminates and curved "J" beam elements from the LDF™ AS-4/PEKK material to be used for testing and analysis

Both of the above goals were met for this program. The remainder of this report briefly describes the activities and results of each of the tasks performed for this sub-contract. In conclusion, it is felt that based on the results of this program along with other internal Du Pont efforts (72" radius, 90 degree segment "Z" beam; figure 2) that the concept of fabricating fuselage frames via LDF™ stretch forming is feasible.

Statement of Work:

Task 4.1.1. Component Design/Specification

With the University of Delaware, the part dimension and geometry was defined as given in figure 3. This part design was chosen after discussions with NASA-Langley and Boeing Commercial Airplane Group as to its value to Boeing's fuselage study. Two 12 ply layups giving a nominal thickness of .064 inches were chosen which will allow for testing the beam in the University of Delaware test equipment. Six curved "J" beams were to be fabricated from each of these layups. The layups were chosen to give one longitudinally "stiff" and "soft" beam. The layup orientations, part designation and number of parts are given below:

Part Designation	# parts	Layup Orientation	# plies
J-#	6	[+45/-45/0/90/0/0]s	12
J2-#	6	[+45/-45/90/+45/-45/0]s	12

Figure 4 shows how the plies were oriented in the "J" beams.

Task 4.1.2. Test Laminate Fabrication

Twelve 14" X 14" test laminates were fabricated and delivered to University of Delaware. Laminates were made by laying up a multi-ply stack of LDF™ AS-4/PEKK tape (fiber volume = 58%; ply thickness = 0.0053") on a flat steel tool and consolidating the stack in a high temperature/pressure autoclave using Kapton® as the bagging material. The autoclave cycle consisted of a temperature ramp to 370 C under 300 KPa pressure, followed by an increase to 2.3 MPa pressure with a dwell time of 20 minutes for consolidation, and then cooled at a rate of 3-4 C/min. Vacuum (28-29 mm Hg) was kept on the bag throughout the cycle. Layup orientations for the laminates are given by the following:

# laminates	Layup Orientation	# plies
3	[+45/-45/0/90/0/0]s	12
3	[+45/-45/90/+45/-45/0]s	12
3	$[0]_8$	8
3	[+45/0/-45/90]s	8

Task 4.1.3. "J" Beam Tool Design and Fabrication

Risk reduction experiments were performed to determine stock shape tool dimensions and optimum autoclave fabrication process These experiments led to the current stock shape tools which were fabricated from tooling steel. The tool is composed of three pieces (sheet metal "Z", machined steel bar, machined flat plate). Two autoclaved straight "J" beams (40" long; see figure 5) were made with the measurements of the first beam given in table 1. The angles of the straight "J" beam were within tolerances specified for use as a stock shape. Likewise, the vertical height and thicknesses were within a few percent of what was specified which was adequate for stretch forming. Ultrasonic scans and photomicrographs verified that the tool and autoclave process gave well consolidated "J" stock shapes (see figures 6 and 7). Two more straight stock shape tools for the autoclave were made to ensure an adequate supply of "J" stock shapes were available to meet the delivery date for stretch formed frames.

Curved "J" beam matched metal tool for the research stretch former was fabricated and assembled. Safety checks and temperature profiles were run on the tool to verify that it met design requirements. The tool met the requirements and was cleared for process development.

Task 4.1.4 Process Development

The stretch forming process to make curved "J" beams is schematically shown in figure 8. A straight "J" stock shape was inserted into the Du Pont Research Stretch Former and clamped in place outside the heating zone. Electric heaters heated the part and tooling to the process temperature of 370 C. At this point, the part was stretched and formed to the contour of the tool. After the stretching was completed, pressure was applied normal to the web and flanges to fully reconsolidate the part. The part is then cooled to below the resin glass transition temperature (156 C) while under pressure before removing it from the machine.

Part quality was determined by evaluating photomicrographs of the cross sections, ultrasonic scans of the web region and part thickness along the beam. In determining the initial process conditions, priority

was given to consolidation level due to the results of the Boeing Helicopter C-Channel program. Therefore, ultrasonic scans and visual appearance (no wrinkles or buckles) were initially weighted more than thickness uniformity in determining preliminary process conditions.

Ten trial runs were needed to debug the tooling and obtain curved "J" beams with no visual defects. In addition to debugging the tool during these trial runs, the temperature profile, dwell times and stretch forming rates were also varied. Consolidation pressures were set at a high level to ensure low void parts were obtained. These pressures were used throughout the program. Most of the stretch formed parts showed 90% or greater of the web area having low decibel losses (2-3 db) in their ultrasonic scans using 5 MHz frequency (TTU) (figure 9). This generally indicates a void free area which was verified by photomicrographs of the cross sections (figure 10).

Part thicknesses of the initial stretch formed beams ("J-#" layup) varied widely from the nominal thickness with the ends of the parts showing a visual impression created by the tooling. Modifications to the tooling eliminated these visual defects and lowered the thickness deviation from nominal. "J2-#" curved beams showed thicknesses with less part to part variation (+/-5%) and a smaller deviation from the nominal thickness than the "J-#" curved beams. Due to program cost and timing considerations, it was decided that the process conditions after the tenth run would be used to produce the 12 curved "J" beams even though more process development was needed to improve part to part thickness reproduciblity for the "J-#" layup beams.

Task 4.1.5. Produce 12 Curved "J" Beams

The following are the number of parts delivered of each layup orientation:

# Parts	Layup Orientation
7	[+45/-45/0/90/0/0]s
6	[+45/-45/90/+45/-45/0]s

Figure 11 shows the final trimmed "J" beam element and a section of the stock shape used to stretch form the curved "J" beam element.

An extra "J-#" beam was given to University of Delaware to use in setting up their test equipment. All parts had ultrasonic scans of the web region showing 95% or greater of the area having a decibel loss of 4 or less (figure 12). As stated earlier this corresponds to less than 1% voids in these regions. Photomicrographs of the cap, web and inner flange regions verified the C-scan observations that the curved "J" beams had a low void content (figure 13).

Thickness measurements for these curved "J" beam elements are shown in figures 14, 15 and 16. As stated in the Process Development section, the consolidation pressures for the curved "J" beams were not optimized during this program and were set at a high level to ensure full consolidation. Consolidation pressures for this program were approximately 5 times higher than what is needed to consolidate a flat laminate. This accounts for most of the curved "J" beam thickness variations due to transverse squeeze flow of the 0 degree plies from the web out through the edges of the beam. In addition, figures 15 and 16 showed that there was a layup dependency on the thickness uniformity with the "J2-#" layup being more uniform than the "J-#" layup. This was due to the "J2-#" layup having a smaller percentage of 0 degree plies than the "J-#" layup (17% vs. 50%). These observations are in agreement with the amount of edge flash seen in the formed parts. It is felt that lower pressures can be utilized to achieve better thickness uniformities without any loss in consolidation. This is especially true for the "J-#" layup as was suggested in the Process Development section.

The final measurements made on the curved "J" beams were on the inner and outer radii. A Unigraphics CAD/CAM unit produced a paper template of the inner and outer radii to visually determine whether the beam outer dimensions matched those for the design. All of the curved "J" beams fabricated had inner and outer radius dimensions that matched those of the template along the entire length of the arc (outer radius = 40.5"; inner radius = 37.8"). This result was expected since match metal tooling was used to stretch form the segment thereby giving outer dimensions within tolerance of those specified. This is an important result since the outer radius dimensions are critical for bonding frames into the current Boeing ATCAS fuselage design.

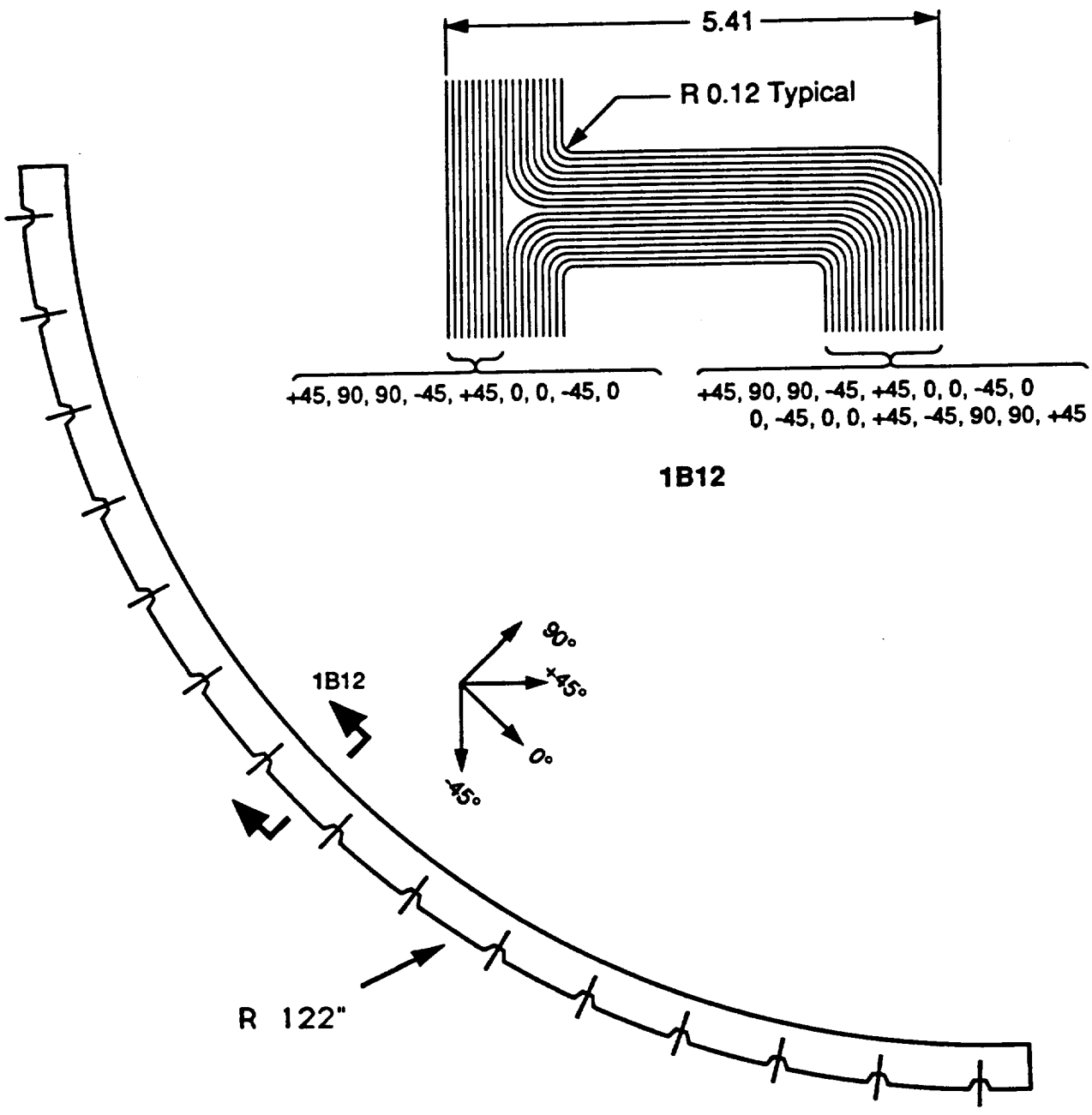

Figure 1

BCAG Curved "J" Frame for NASA ACT Program

ORIGINAL PAGE
BLACK AND WHITE PHOTOGRAPH

Figure 2

72" Radius, 90° Segment "Z" Beam Demonstrator

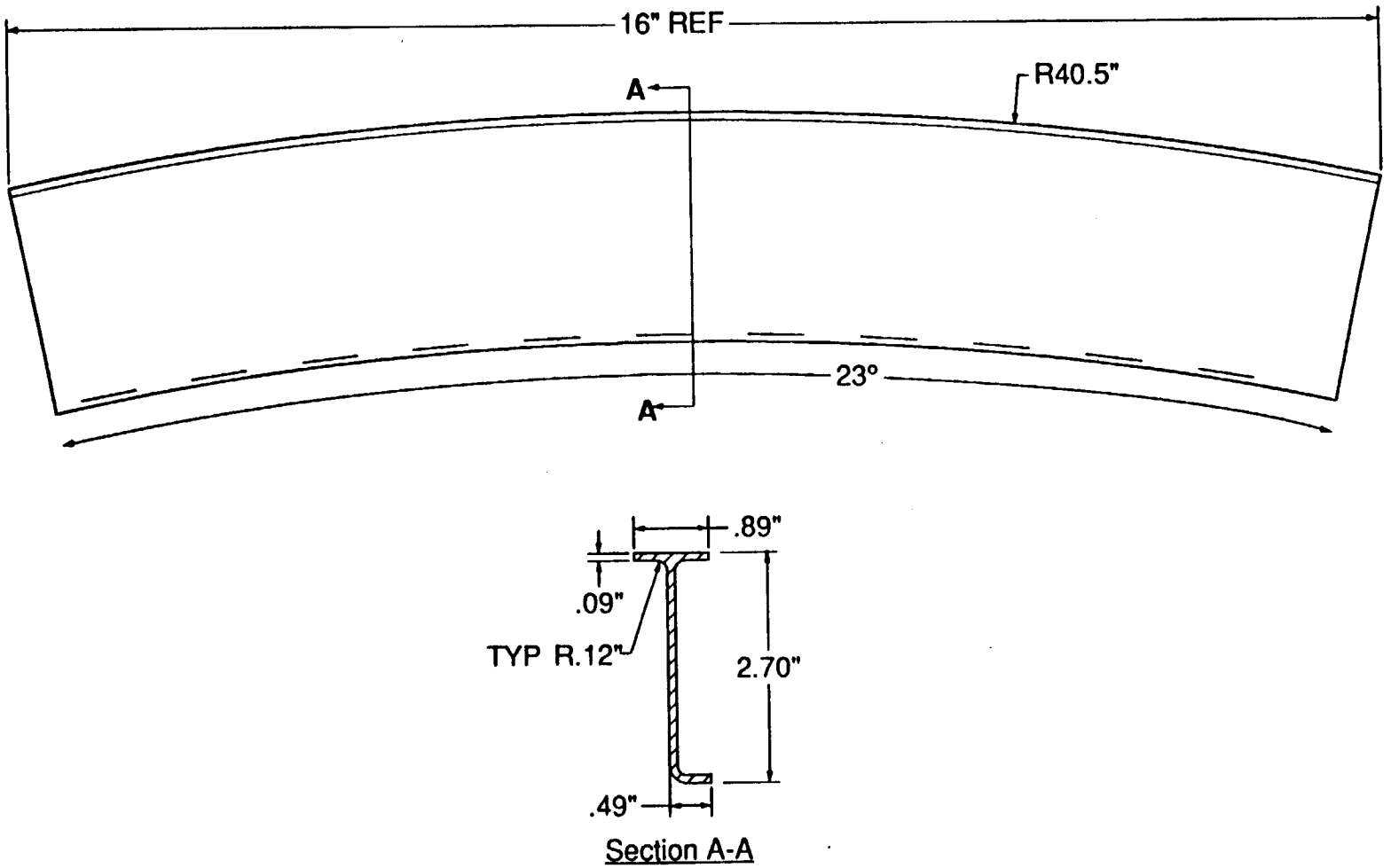

Figure 3

Proposed Scaled, Curved "J" Beam Element

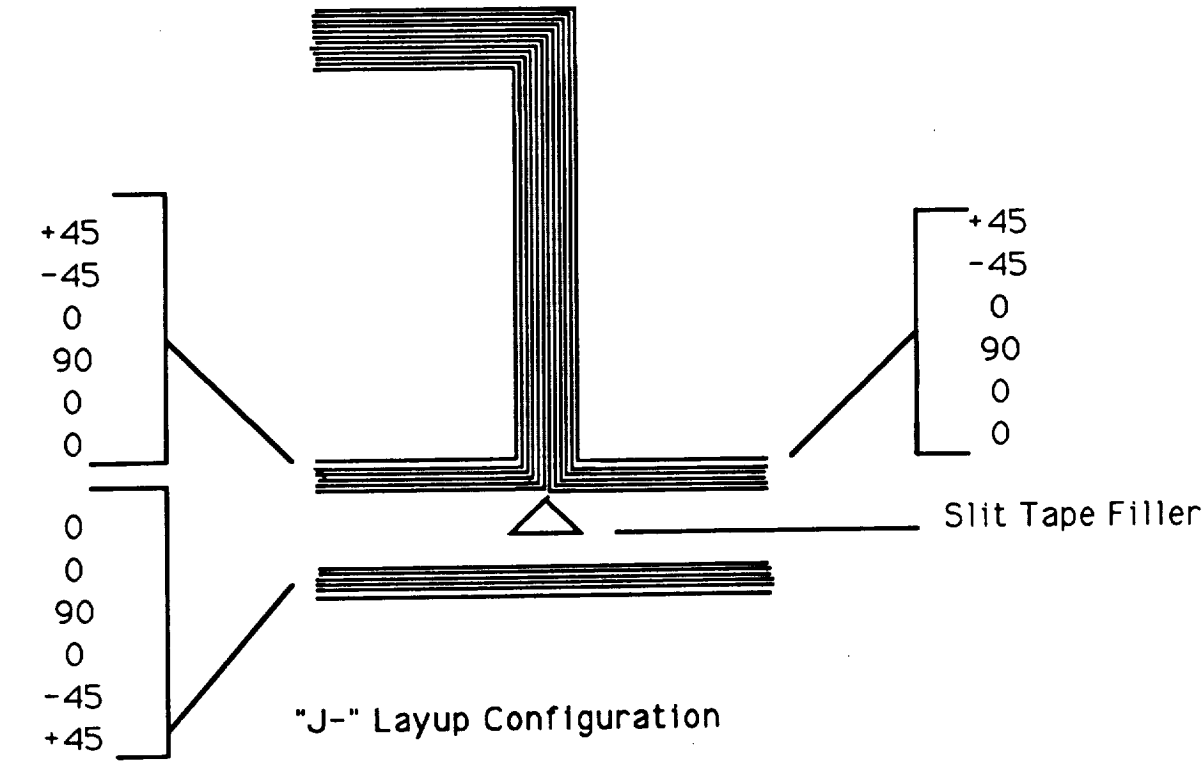

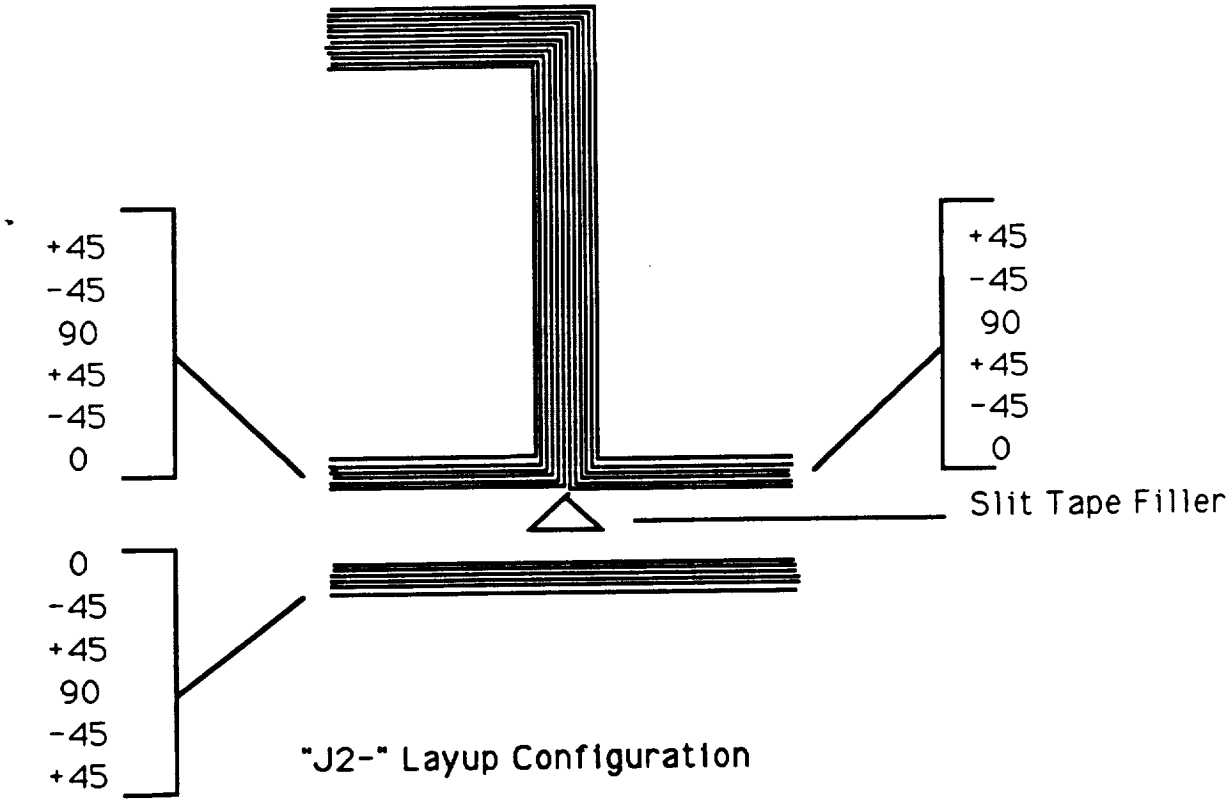

Figure 4

"J" Beam Ply Layup Orientation

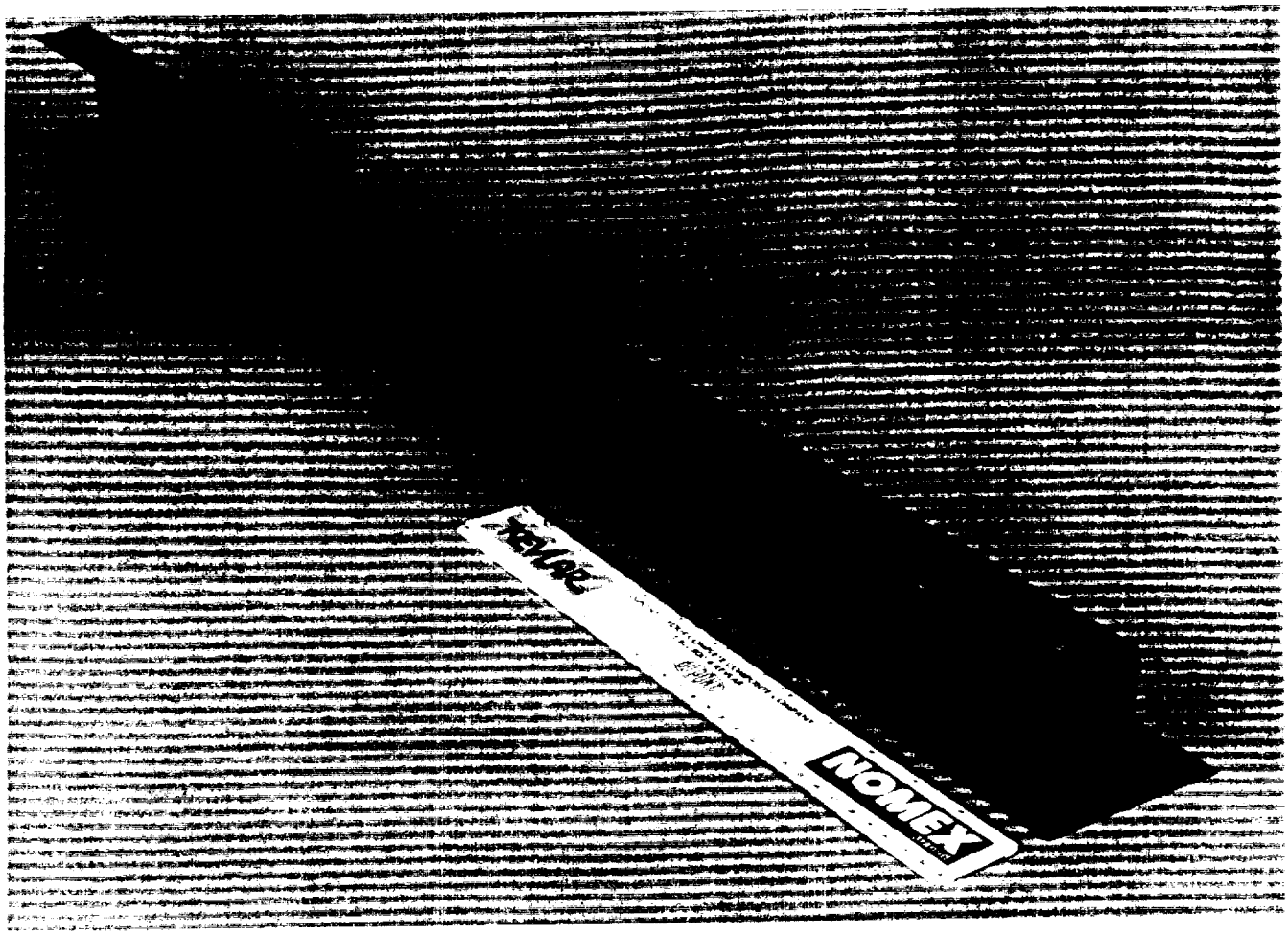

Figure 5

Autoclaved Straight "J" Beam - 40" Long

Table 1

"J" Beam Stock Shape Dimensions

MEASUREMENT	ANGLE			WIDTH	THICKNESS
	A	B	C		
1	90.559	89.877	90.121	2.585	0.066
2	90.694	89.869	90.238	2.588	0.066
3	90.572	90.132	89.951	2.587	0.064
4	90.454	89.679	90.303	2.59	0.064
5	89.758	90.262	90.65	2.588	0.064
6	90.224			2.585	0.063
7	90.273			2.596	0.065
8	90.024			2.598	0.064
9					0.065
10					0.063
11					0.064
12					0.063
13					0.064
AVE	90.319	89.9638	90.253	2.59	0.064
MAX	90.694	90.262	90.65	2.598	0.066
MIN	89.758	89.679	89.951	2.585	0.063
RANGE	0.936	0.583	0.699	0.0132	0.003
STD DEV	0.315	0.232	0.259	0.00489	0.001

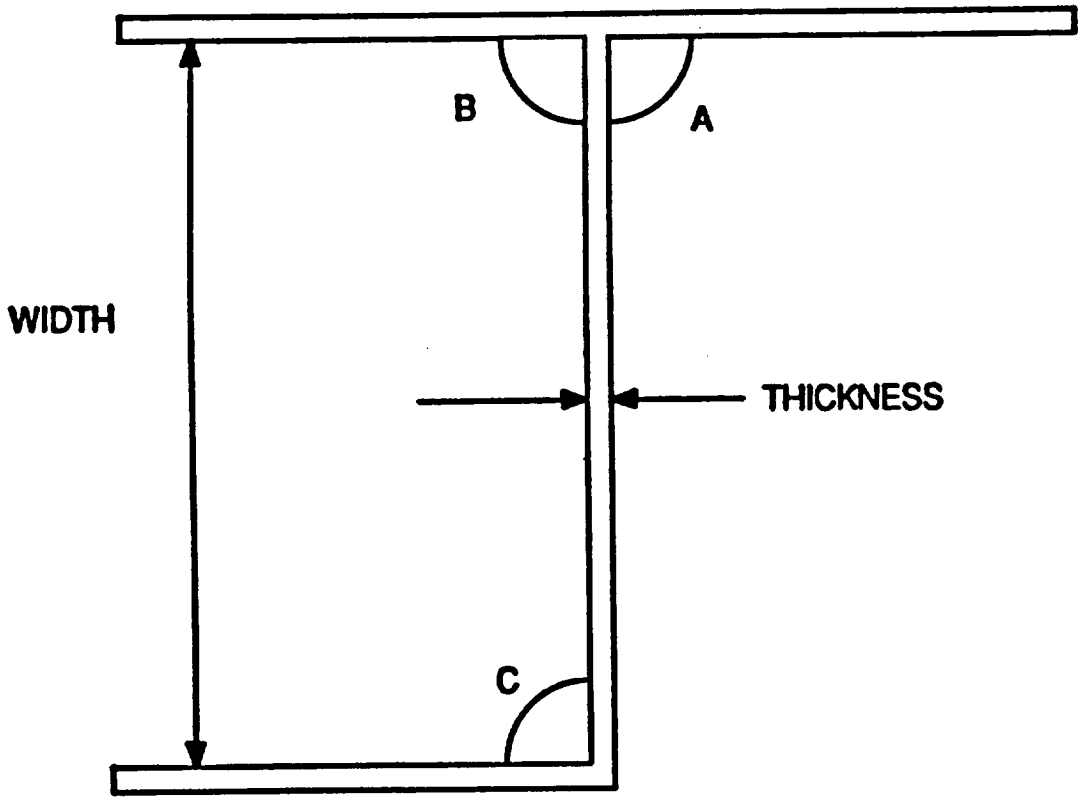

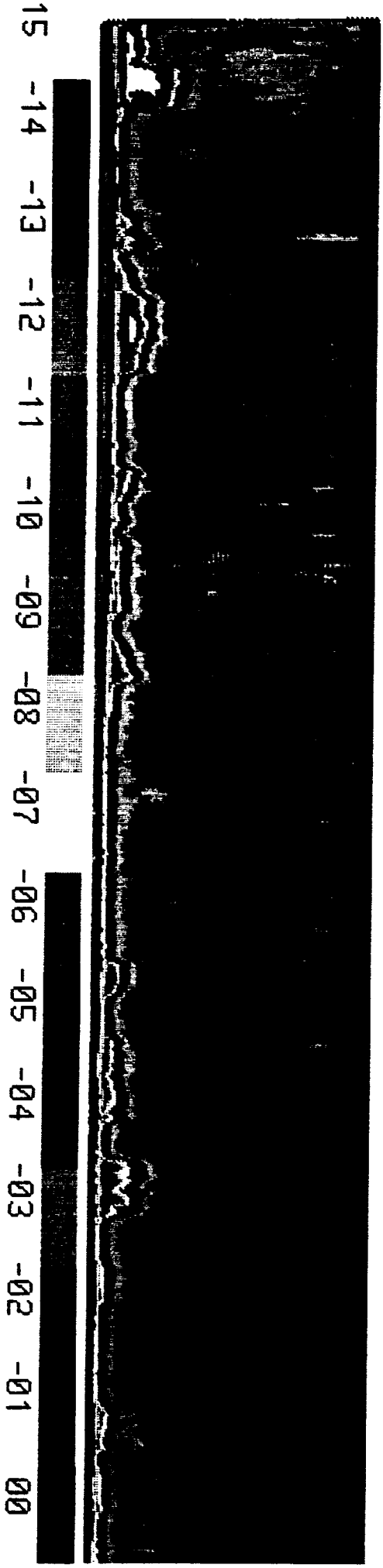

Figure 6
Ultrasonic Scan of
J-5 Straight Stock Shape -
Top Flange Area
(See Above)

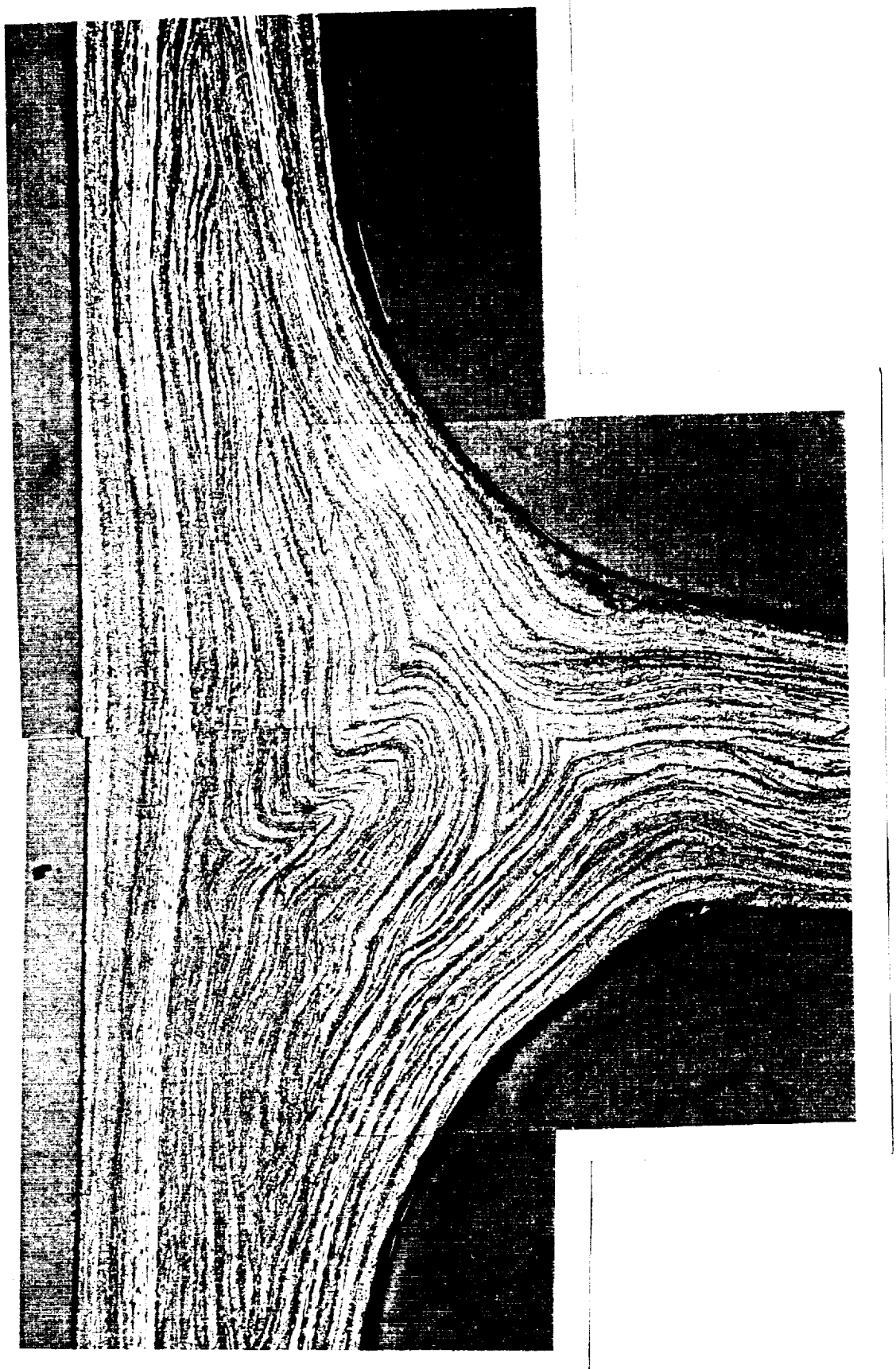

Figure 7

Photomicrograph of J-9 Straight Stock Shape Cross-Section

- Cap Radii -

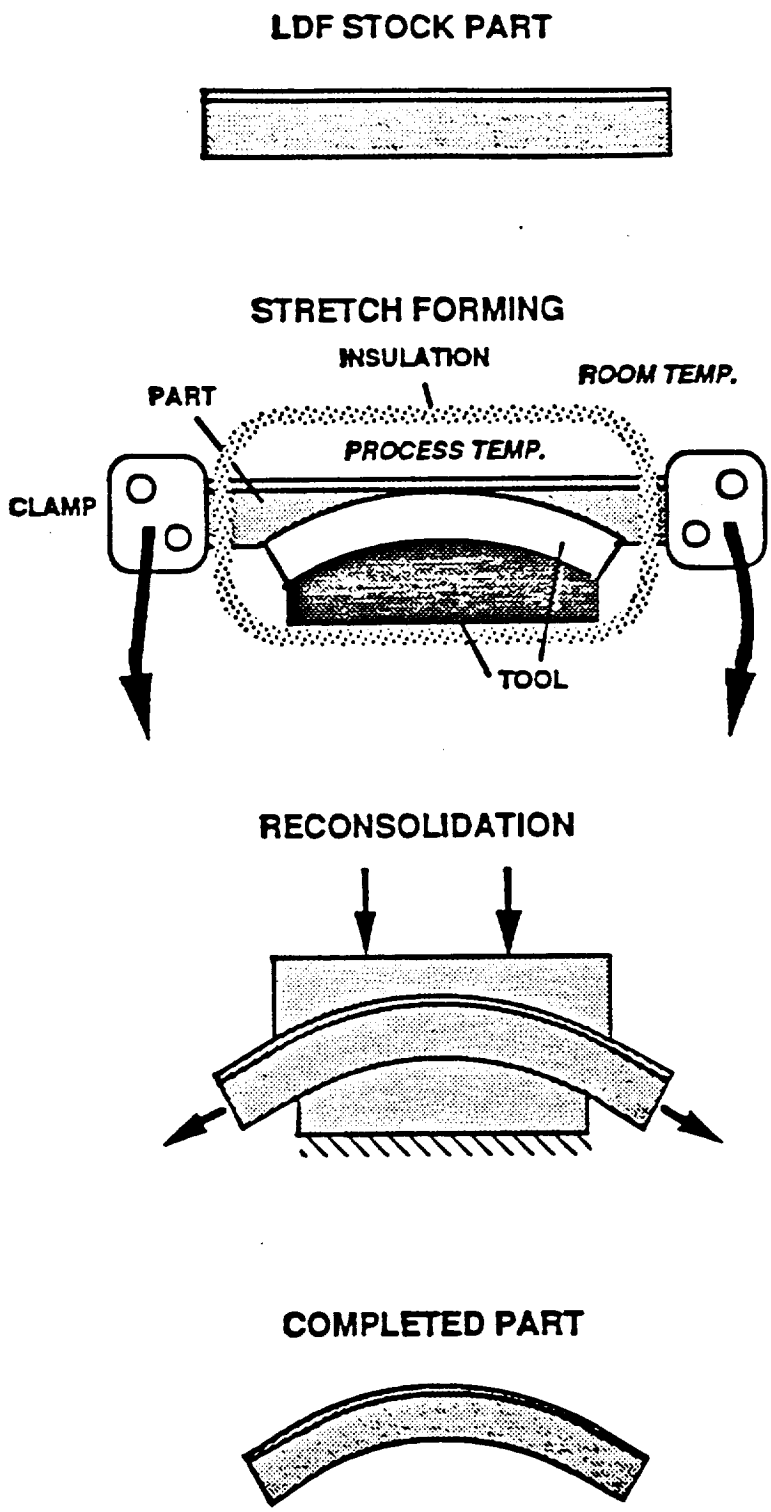

LDF™ Stretch-Forming Concept Definition

Figure 8

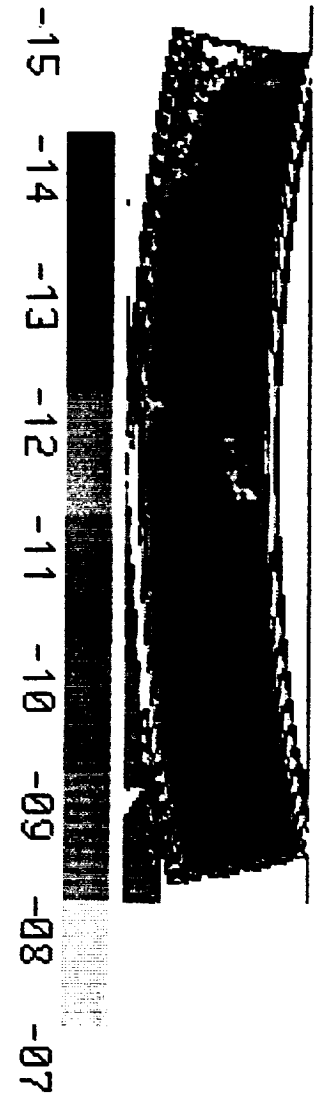

Figure 9
Ultrasonic Scan of Curved "J" Beam J-9
- Web Area -

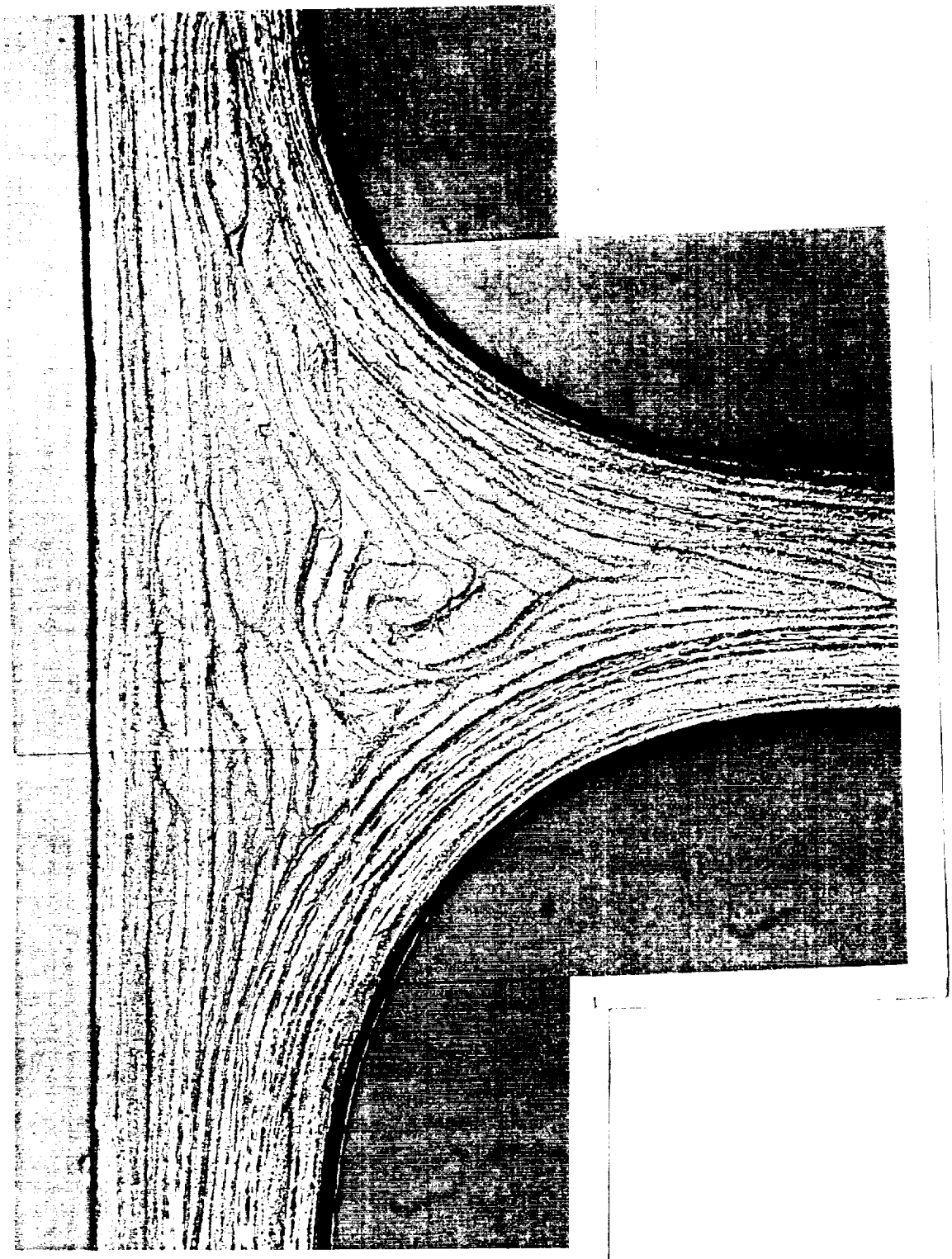

Figure 10

Photomicrograph of J-9 Curved Beam Cross Section

- Cap Radii -

Figure 11

Curved "J" Beam and Stock Shape Section

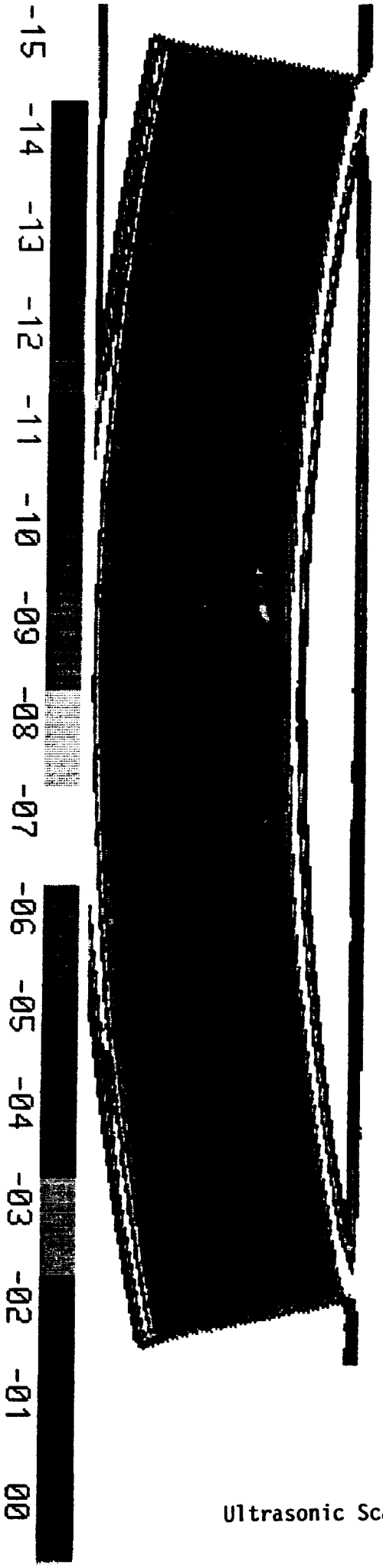

Figure 12

Ultrasonic Scan of J-20 Curved "J" Beam Web Region

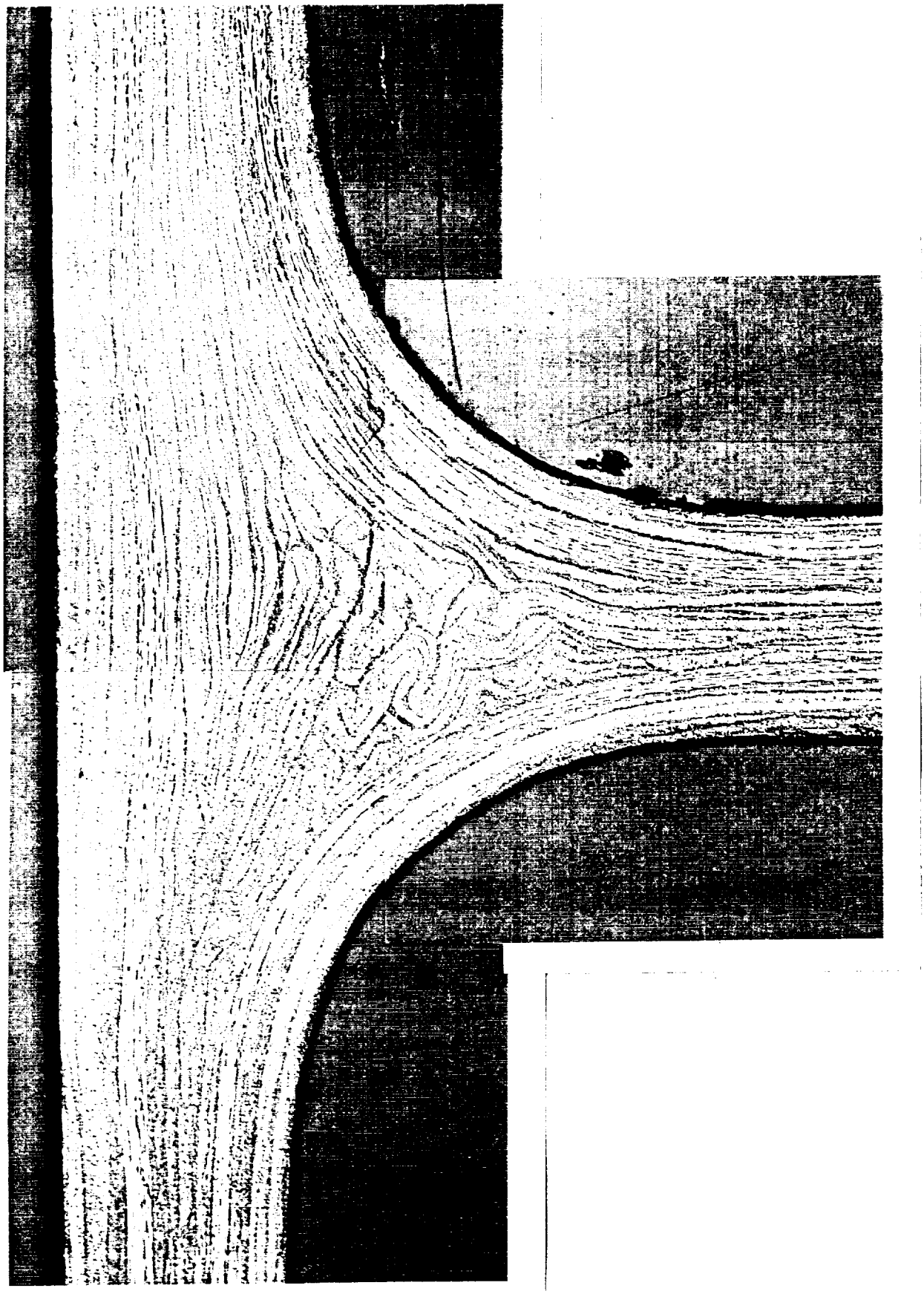

Figure 13

(a) Photomicrograph of J-20 Curved "J" Beam (25x)

- Cap Radii -

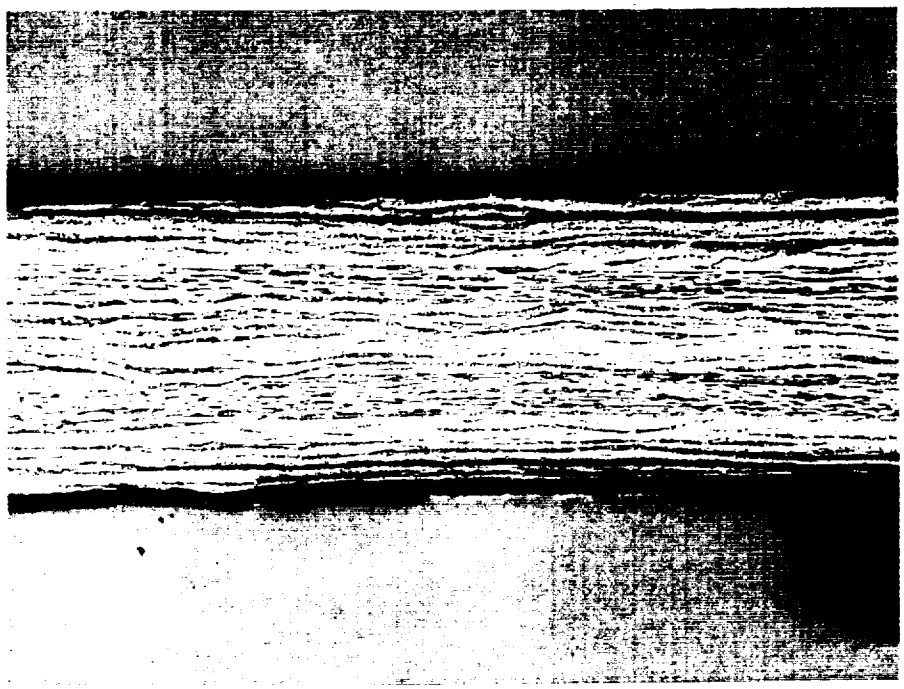

(b)

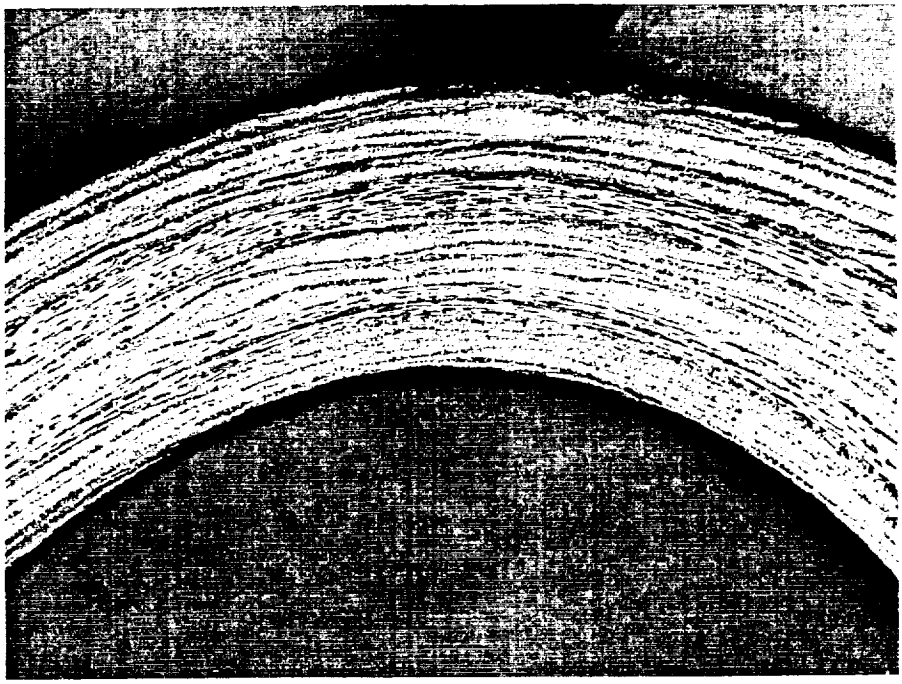

(c)

Figure 13

Photomicrograph of J-20 Curved "J" Beam:
(B) Web Region
(C) Inner Flange Radius

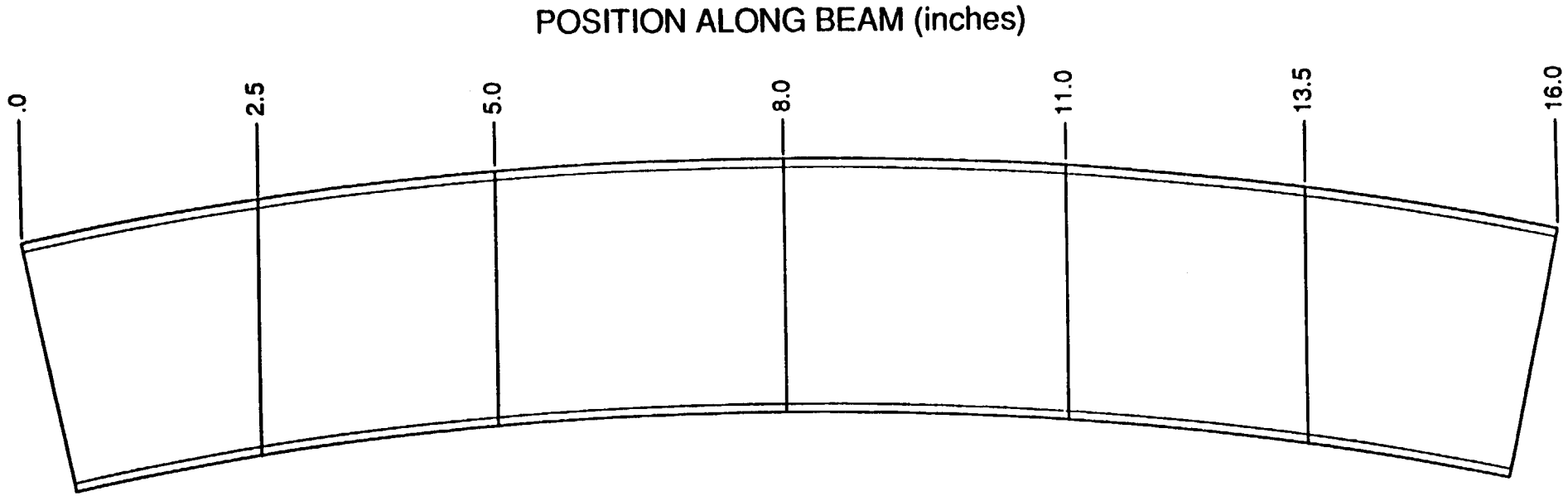

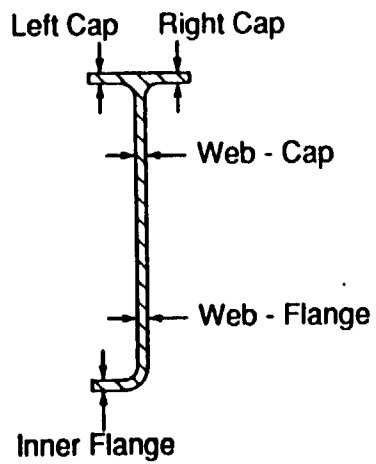

Figure 14

Thickness Measurement Locations

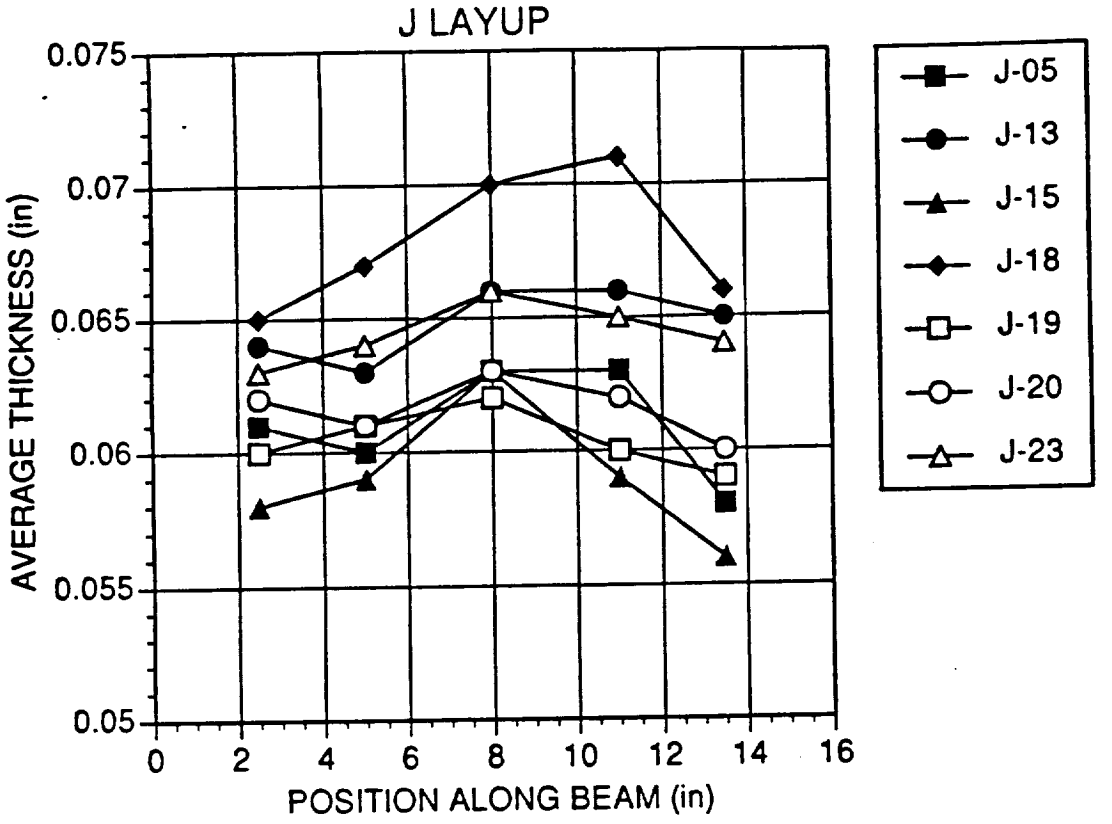

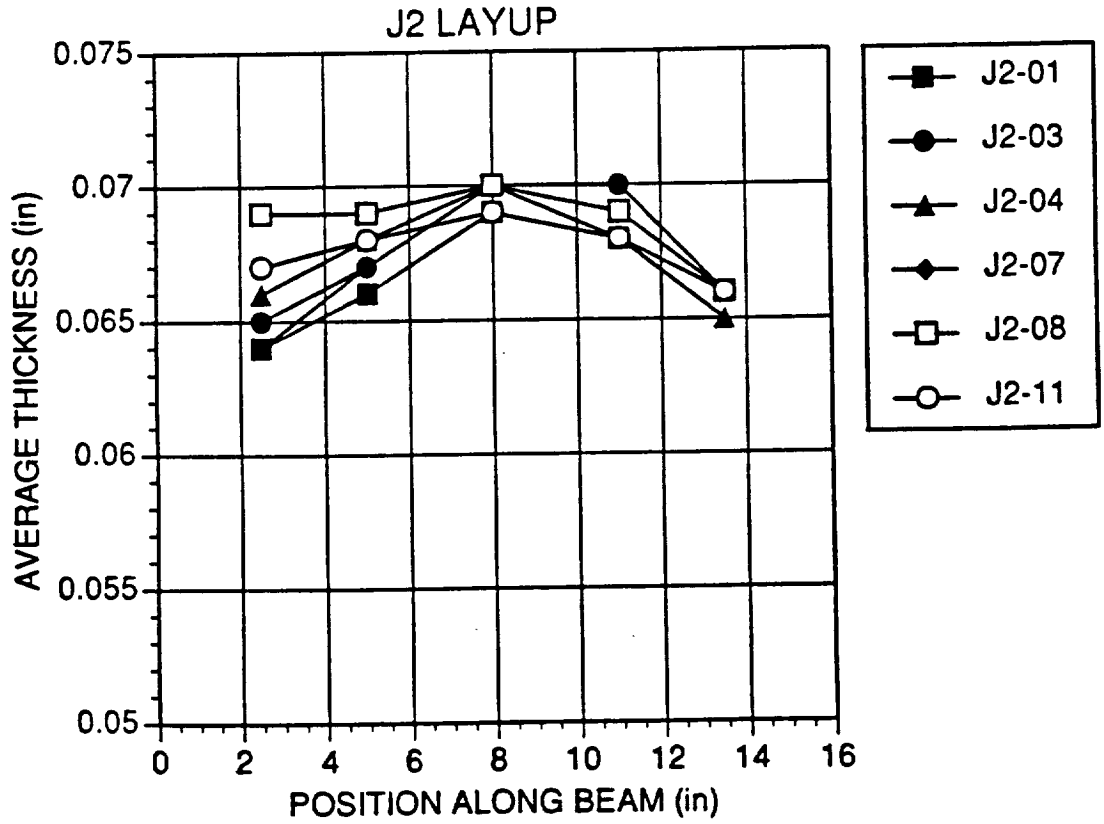

Figure 15

Average Part Thickness by Position

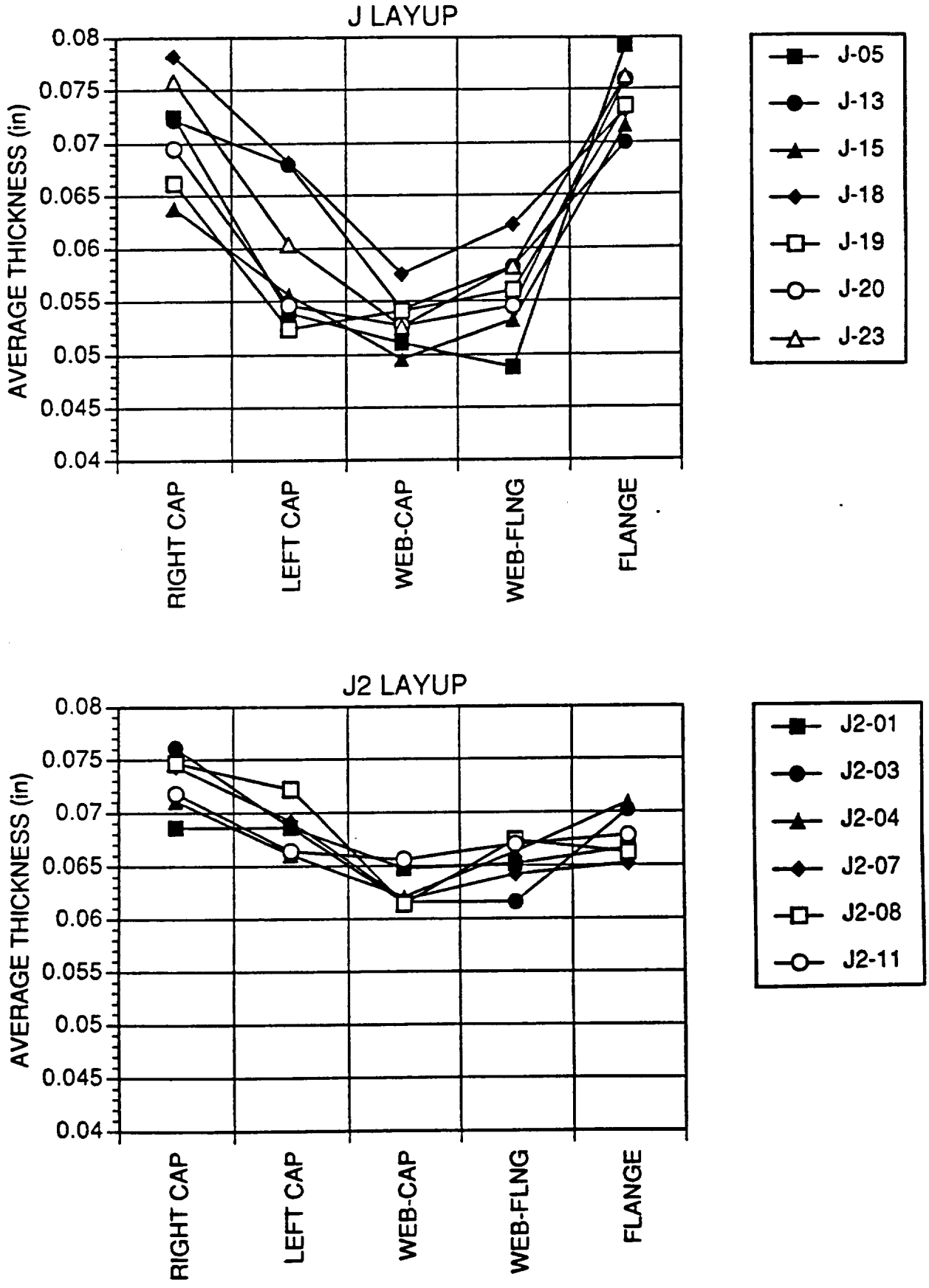

Figure 16

Average Part Thickness by Section

REPORT DOCUMENTATION PAGE

Form Approved
OMB No. 0704-0188

1. AGENCY USE ONLY (Leave blank)	2. REPORT DATE	3. REPORT TYPE AND DATES COVERED
	September 1992	Contractor Report

4. TITLE AND SUBTITLE
Continuation of Tailored Composite Structures of Ordered Staple Thermoplastic Material

5. FUNDING NUMBERS
C NAS1 - 18758
WU 510-02-12-01

6. AUTHOR(S)
Michael H. Santare and R. Byron Pipes

7. PERFORMING ORGANIZATION NAME(S) AND ADDRESS(ES)
Department of Mechanical Engineering and
Center for Composite Materials
University of Delaware
Newark, DE 19716-3140

8. PERFORMING ORGANIZATION REPORT NUMBER

9. SPONSORING / MONITORING AGENCY NAME(S) AND ADDRESS(ES)
National Aeronautics and Space Administration
Langley Research Center
Hampton, VA 23665-5225

10. SPONSORING / MONITORING AGENCY REPORT NUMBER
NASA CR-189671

11. SUPPLEMENTARY NOTES
Langley Technical Monitor: Dawn C. Jegley
Final Report

12a. DISTRIBUTION AVAILABILITY STATEMENT
Unclassified - Unlimited
Subject Category 24

12b. DISTRIBUTION CODE

13. ABSTRACT (Maximum 200 words)

The search for cost effective composite structure has motivated the investigation of several new approaches to develop composite structure from innovative material forms. Among the promising new approaches is the conversion of planar sheet to components of complex curvature through sheet forming or stretch forming. In both cases the potential for material stretch in the fiber direction appears to offer a clear advantage in formability over continuous fiber systems. Material heterogeneity can be induced during these manufacturing processes of thermoplastic composites. Predictions for the effective viscosities of a hyper-anisotropic medium consisting of collimated, discontinuous fibers suspended in a viscous matrix developed earlier by the authors have been extended to capture the characteristics of typical polymers including non-Newtonian behavior and temperature dependence. The influence of fiber misorientation has also been modeled by compliance averaging to determine ensemble properties for a given orientation distribution. In addition, a design tool is presented for predicting the effect of material heterogeneity on the performance of curved composite beams such as those used in aircraft fuselage structures.

14. SUBJECT TERMS	15. NUMBER OF PAGES
Advanced composites; Tailored structures	87
	16. PRICE CODE

17. SECURITY CLASSIFICATION OF REPORT	18. SECURITY CLASSIFICATION OF THIS PAGE	19. SECURITY CLASSIFICATION OF ABSTRACT	20. LIMITATION OF ABSTRACT
Unclassified	Unclassified		